COMPUTATIONAL DESIGN AND PERFORMANCE PREDICTION OF CREEP-RESISTANT FERRITIC SUPERALLOYS

1. **Report Term**: Final report
2. **Reporting Period Start/Stop Date**: 10/01/2014-09/30/2017
3. **Principal Authors Name**: Peter K. Liaw
4. **Date Report Was Issued**: 12/31/2017
5. **DOE Award Number**: DE-FE0024054
6. **Name and Address of Submitting Organization**: Department of Materials Science and Engineering, The University of Tennessee 1508 Middle Drive, Knoxville, TN 37996, USA

DISCLAIMER

Abstract

Ferritic superalloys containing the B2 phase with the parent $L2_1$ phase precipitates in a disordered solid-solution matrix, also known as a hierarchical-precipitate-strengthened ferritic alloy (HPSFA), had been developed for high-temperature structural applications in fossil-energy power plants. These alloys were designed by adding Ti into a previously-studied NiAl-strengthened ferritic alloy (denoted as FBB8 in this study). Following the concept of HPSFAs, in the present research, a systematic investigation on adding other elements, such as Hf and Zr, and optimizing the Ti content within the alloy system, has been conducted, in order to further improve the creep resistance of the model alloys. Studies, including advanced experimental techniques, first-principles calculations on thermodynamic and mechanical properties, and numerical simulations on precipitation hardening, have been integrated and conducted to characterize the complex microstructures and excellent creep resistance of alloys. The experimental techniques concern transmission-electron microscopy (TEM), scanning-electron microscopy (SEM), neutron diffraction (ND), and atom-probe tomography (APT), which provide the detailed microstructural information of the model alloys. Systematic tension/compression creep tests have also been conducted in order to verify the creep resistance of the potential alloy compositions. The results show that when replacing Ti with Hf and Zr, it does not form the $L2_1$ phase. Instead, the hexagonal Laves phase forms and distributes majorly along the grain boundary, or large segregation within grains. Since the Laves phase does not form parent to the B2-phase precipitates, it cannot bring the strengthening effect of HPSFAs. As a result, the FBB8 + 2 wt. % Hf and FBB8 + 2 wt. % Zr alloys have similar mechanical properties to the original FBB8. The FBB8 + Ti series alloys had also been studied, with the creep tests and microstructural characterizations, the FBB8 + 3.5 wt.% Ti possesses the greatest creep resistance, with the $L2_1$/B2 phase ratio of 4 (80 vol.% of the precipitates is the $L2_1$ phase, and 20 vol.% is the B2 phase).

First-principles calculations include thermodynamics, elastic properties, and interfacial properties, which have been conducted for the understanding of the thermodynamic and mechanical properties of HPSFAs. In addition to the systematic experimental approach and first-principles calculations, a series of numerical tools and algorithms, which assist in the optimization of creep properties of ferritic superalloys, are utilized and developed. These numerical simulation

results are compared with the available experimental data and previous first-principles calculations, providing the deep insight of creep mechanisms of the creep-resistant ferritic superalloys.

To conclude the present research, we've found that (1) only FBB8 + Ti alloys have the potential of forming HPSFA, and FBB8 + Hf and FBB8 + Zr do not work. Therefore, only FBB8 + Ti alloys have desirable creep resistance, (2) the optimal composition for the FBB8 + Ti alloys is FBB8 + 3.5% Ti, which has the greatest creep resistance (218.8 MPa as the threshold stress at 700 ^{o}C), (3) first-principle calculations obtained results that could not be obtained in experiments, which are relevant to develop ferritic superalloys with the improved creep resistance, and (4) two-dimensional dislocation-dynamics simulations investigate effects of factors like precipitate volume fractions and precipitate radii in the alloy systems, which helps in developing the most desirable microstructure with greatest strengthening.

Table of Content

1. First-principles Study of Thermodynamics

Congruent ordering energies [body-centered cubic (BCC) → B2, B2 → $L2_1$ and BCC → $L2_1$] in the Al-Ni-Ti system had been calculated in this chapter. Relevant ordering energies are obtained from first-principles using Vienna ab-initio simulation package (VASP) and Alloy Theoretic Automated Tookit (ATAT) codes [79]. Computed results are important in modeling the phase stability [using CALculation of PHAse Diagrams (CALPHAD) technique [80]], understanding the microstructure dynamics, phase transformation kinetics and microstructure evolution in multi-component alloys. However, relevant ordering energies could not be obtained from conventional experiments, such as the reaction calorimetry, justifying the usage of computational approach.

1.1 Introduction

In order to understand and model properties of multi-phase alloys, we believe that it is necessary to understand properties of individual phase(s), hence the properties of aggregate phases could be modeled and analyzed suitably. Following the same logic with determining elastic properties (C_{ij}) of Fe, B2-NiAl, and $L2_1$-Ni_2TiAl from computations, ordering energies can also be computed from the first-principles method.

Thermodynamics is key to understand microstructure evolution in multi-component alloys, microstructure dynamics, phase transformation kinetics, etc. In an earlier study [1, 2, 40, 60], supported by the Electric Power Research Institute (EPRI)-sponsored research at Northwestern University (NU), we had established the formation of hierarchical microstructures in an Fe-8.08Al-12.2Cr-1.9Mo-18.2Ni-2Ti alloy.

In this prototype alloy, the microstructure consists of the BCC-Fe, B2-NiAl, and $L2_1$-Ni_2TiAl phases [1, 2]. While the former represents a disordered BCC structure, the latter two represent the nearest-neighbor (NN) ordered structure (B2, NiAl-type) and the next-nearest neighbor (NNN, $L2_1$-Ni_2TiAl) ordered structures of the BCC phase, respectively. Therefore, it is incumbent to quantify these ordering energies.

Phase equilibria in the Al-Ni-Ti system have been summarized and assessed by Zeng et al [3], but experimental thermodynamic data is insufficient to assess the ordering energies mentioned above. Therefore, we have employed first-principles methods to quantify relevant ordering energies.

The first-principles calculations presented here are based on the electronic density-functional theory (DFT), and have been carried out, using the ab-initio total-energy program VASP program [4-6] projector-augmented wave (PAW) method [7], which retains the all-electron character, but the all-electron wave function is decomposed into a smooth pseudo-wave function, and a rapidly-varying contribution localized with the core region. In its current implementation of VASP, the PAW method freezes the core orbital to those in a reference configuration. However, very recently a relaxed core PAW method has been proposed [8] that is shown to yield results with the accuracy comparable to the FLAPW (full potential-linearized augmented plane wave) method [9]. The PAW method includes the non-linear core correction, accounts for the core-core overlap, and is free of any shape approximation for both the charge density and electronic potential.

The PAWs employed in the present work explicitly treat three valence electrons for Al ($3d^2 3p^1$), four for Ti ($3d^3 4s^1$), and ten for Ni ($3d^{10}$), A kinetic-energy cutoff of 410 eV was used for the expansion of the electronic wave functions in plane waves. All calculated results were derived, employing the generalized gradient approximation (GGA) for the exchange-correlation energy due to Perdew [10]. Brillouin-Zone integrations were performed, using Monkhorst-Pack [11] k-point meshes, and the Methfessel-Paxton [12] technique with the smearing parameter of 0.1 eV. For B2 and $L2_1$ phases, we have taken k-meshes of $16 \times 16 \times 16$, and $8 \times 8 \times 8$, respectively. The total energy was converged numerically to less than 5×10^{-6} eV/atom with respect to electronic and ionic degrees of freedom. The latter was relaxed, using Hellman-Feynman forces with a preconditioned conjugate gradient algorithm. All calculations are performed, using spin-polarized Hamiltonian and the "accurate" setting within VASP to avoid wrap-around errors.

While VASP is a commercial package, ATAT (written by Axel van de Walle, previously at Northwestern and now a faculty at Brown University) code [13-15] to generate 32-atom special quasirandom structure (SQS) supercells (BCC and B2 structures) at 50 at.% Ti. It is implicit that a ternary (BCC) SQS supercell, say in the Al-Ni-Ti system, at 25 atomic percent (at.%) Al, 50 at.% Ni, and 25 at.% Ti corresponds to the same composition as the Heusler phase Ni_2TiAl. Similarly, the ternary (B2) SQS supercell, say in the Al-Ni-Ti system, at 50 at.% Ni corresponds to the same composition as the Heusler phase Ni_2TiAl. Thus, these two SQS supercells should define ordering energies at congruent compositions i.e., BCC to B2, B2 to $L2_1$, and BCC to $L2_1$.

1.2 Simulation Procedure

Modeling configurational disorder in solid solutions is an important topic in the alloy theory. One modern approach is to employ supercells, called the special-quasirandom structure (SQS) [16] that is computationally efficient if the goal is to reliably obtain the formation (or mixing) energies, where the effects of short-range ordering (SRO) can be reasonably neglected. Like BCC and B2 phases, the Heusler (Ni_2TiAl) phase also exhibits a finite homogeneity range. However, here, we have considered only the ideal stoichiometry, Ni_2TiAl, to define the driving energy for congruent ordering.

Two major tasks associated with quantifying ordering energies are: (1) the generation of suitable SQS supercells representing ternary BCC and B2 alloys at discrete compositions, and (2) total energy calculations using SQS atomic structures. First-principle calculations allow us to quantify the driving energy of congruent ordering for the BCC → B2 and B2 → $L2_1$ transitions in relevant ternary alloys.

The approach based on SQS, like the cluster-expansion method, parametrizes the energy, *E* (per atom), of the alloy as a truncated polynomial in the occupation variables (σ_i).

$$E(\sigma) = \sum_{\alpha} m_{\alpha} J_a \left\langle \Pi_{i \in \beta} \sigma_i \right\rangle \tag{1}$$

where α is a cluster (a set of sites, *i*, corresponding to two-, three-, four-body, etc.). The sum is taken over all clusters that are inequivalent by a symmetry operation of the space group of the parent lattice, while the average $\langle ..... \rangle_{\alpha}$ is taken over all clusters, "b", which are equivalent to "a" by symmetry. In the generation of SQS structures, attempts are made to match as many correlations as possible with a structure as few atoms in the unit cell as possible. SQSs are traditionally generated, for a given unit cell size, by enumerating every possible supercell of that size and every possible configuration within that unit cell in search of the structure as many pair correlations agreeing with the ones of the disordered state as possible. When multiple configurations match the same number of pair correlations, matching multibody correlations of the disordered state can be used to identify the best SQS [17].

Starting with the ideal SQS supercells generated by the ATAT code, the total energy was calculated by relaxing in a step-by-step manner: (1) Step I involves only the volume relaxation, i.e., without altering the atomic positions and keeping them fixed at the ideal lattice positions; (2)

Step II involves the ionic relaxation, keeping the shape of the supercell fixed; and (3) Step III involves the full relaxation, i.e., all degrees of freedom are relaxed (volume, cell-internal, and cell-external) are relaxed [16]. By repeating Steps I and II several times, we obtain the (volume + ion)-relaxed energy, and in Step III, we obtain the fully-relaxed energy. We define the formation energy as the difference between the total energy of the alloy and the composition-weighted average of pure elements in their ground-state structures. For example, the formation energy ($\Delta_f E$ per atom) of a ternary Al-Ni-Ti alloy is given

$$\Delta_f E = E_{AlNi_2Ti} - 0.25 \times E_{Al} - 0.5 \times E_{Ni} - 0.25 \times E_{Ti} \quad (2)$$

where E_{Ni2TiAl}, total energies (per atom), of the alloy with a BCC or B2 structure, E_{Al}, E_{Ni}, and E_{Ti} are total energies (per atom) of FCC-Al, FCC-Ni, and HCP-Ti, respectively.

We define the congruent ordering energy ($\Delta_{ord}E$) as the difference between the total energy of the Heusler phase ($L2_1$-Ni_2TiAl) and *B*2-SQS at the same composition. For example, in the Al-Ni-Ti system, the ordering energies for the BCC → B2 , B2 → $L2_1$, and BCC → $L2_1$ transitions are given by

$$\Delta_{ord}E(BCC \longrightarrow B2) = E_{B2[SQS(AlNi_2Ti)]} - E_{BCC[SQS(AlNi_2Ti)]} \quad (3)$$

$$\Delta_{ord}E(B2 \longrightarrow L2_1) = E_{L2_1} - E_{B2(SQS[AlNi_2Ti])} \quad (4)$$

$$\Delta_{ord}E(BCC \longrightarrow L2_1) = E_{L2_1} - E_{BCC(SQS[AlNi_2Ti])} \quad (5)$$

where $E_{BCC(SQS(AlNi_2Ti))}$ is the total energy (per atom) of the 32-atom BCC-SQS supercell, and $E_{B2[SQS(AlNi_2Ti)]}$ is the total energy (per atom) of the 32-atom B2-SQS supercell. The quantity, E_{L21}, represents the total energy (per atom) of the 16-atom unit cell of the Heusler phase. As mentioned earlier in this section, the deviation from an ideal composition of Ni_2TiAl was not considered, even though the Ni_2TiAl phase shows a homogeneity range in experimental phase diagrams at 800 and 900 ˚C [18].

1.3 Results

Formation and ordering energies, as defined in Eqs. (2) to (5), calculated at zero K using the VASP code, are listed in Table 1. Kubaschewski [19] and subsequently Hu et al. [20] measured the heat of formation ($\Delta_f E$) of $L2_1$-Ni_2TiAl using a reaction calorimeter. They reported $\Delta_f E$ to be - 56.1 ± 1 and - 55.8 ± 2 kJ/mol-atom, respectively, with the face-centered cubic (FCC)-Al, FCC-Ni, and hexagonal close-packed (HCP)-Ti as reference states. The value of $\Delta_f E$ reported by Kubaschewski was used by Kaufman and Nesor [21] in modeling the phase stability of the ternary

system. Our calculated value of $\Delta_f E$ yields - 51,600 kJ/mol-atom, and the agreement should be considered to be good.

Furthermore, Nash and Liang [22] reported that the lattice parameter of $L2_1$-Ni_2TiAl at room temperature lies in the range of 5.85 to 5.91 Å, while Hu et al. [20] reported the lattice parameter of $L2_1$-Ni_2TiAl to be 5.886 Å. This value also agrees well with our calculated value of 5.8813 Å at zero K.

Considering the limited experimental data and associated uncertainties of thermodynamic data, we believe that our calculated values are good and reliable. However, we have not checked the convergence of ordering energies with respect to supercell sizes (i.e., the SQS supercell size). Here, we have used only a 32-atom SQS supercell. In a future report, additional calculations will be performed to assess the ordering energies using 64-atom SQS supercells. These supercells will help us establish the convergence of calculated ordering energies with respect to the supercell size.

It is important to recognize difficulties to measure ordering energies from calorimetry experiments. Difficulties originate from the fast reaction between elements in a calorimeter, and inability to control the reaction product. It is well known that powders of Al, Ni, and Ti react fast, and it may not be possible to control the crystal structure of the reaction product. Specifically, to measure/define congruent ordering energies, it is necessary to synthesize the BCC solid solution and the B2 phase as the first step but in practice, this process may not be possible. Also, when Al, Ni, and Ti powders are mixed in a calorimeter, the reaction product will be governed by the temperature, diffusion path, etc. In the Al-Ni-Ti system, BCC and B2 phases are stable in a narrow composition range along fast reaction kinetics, restrict the number of experiments that could be performed.

1.4 Conclusion

The computed results then define ordering energies that could not be obtained in conventional calorimetry experiments. Results are relevant to the microstructural design and control in an effort to develop ferritic superalloys with the improved creep resistance.

Table 1. Formation ($L2_1$-Ni_2TiAl) and congruent ordering energies [BCC → B2 , B2 → $L2_1$, and BCC → $L2_1$ phases as defined in Eqs. (2) to (5)] in the Al-Ni-Ti system calculated at 0 K. All values are in kJ/mol-atom. Reference states of the formation energy are: FCC-Al, FCC-Ni, and HCP-Ti.

Formation and ordering energies (in kJ/mol-atom)	
Formation Energy ($L2_1$-Ni_2TiAl)	
$\Delta_f E$ ($L2_1$ - Ni_2TiAl)	-51,600
Ordering Energy	
$\Delta_{ord} E$ (BCC → B2):	-14,800
$\Delta_{ord} E$ (BCC → $L2_1$):	-23,750
$\Delta_{ord} E$ (B2 → $L2_1$):	-8,950

2. First-principles Study of Elastic Properties

Polycrystalline elastic properties of phases of Fe and intermetallics in the Al-Ni-Ti system are calculated and summarized in this chapter. Specifically, using single-crystal elastic constants (C_{ij}) of Fe, B2-NiAl, and $L2_1$-Ni_2TiAl, we have calculated isotropic (or, polycrystalline) elastic properties: Bulk, shear, Young's modulus and Poisson's ratio. There is no experimental single-crystal data of $L2_1$-Ni_2TiAl to verify our calculated results. It is extremely difficult, if not impossible, to prepare single-crystal of $L2_1$-Ni_2TiAl as it forms by a transition peritectic (U-type) reaction in the Ni-Ti-Al system. However, it may be possible to prepare polycrystalline specimens (by conventional casting) and measure polycrystalline (or isotropic) elastic properties.

2.1 Introduction

To understand and model properties of the multi-phase alloy, we believe that it is necessary to understand properties of individual phase(s) so that the property of aggregate phases could be modeled and analyzed suitably. Following the same logic with the computation on the elastic properties (C_{ij}) of Fe, B2-NiAl, and $L2_1$-Ni_2TiAl from ab initio methods, here, we report isotropic elastic properties of phases in a hierarchical microstructure [1, 2] in a prototype alloy consisting of BCC-Fe, B2-NiAl and $L2_1$-Ni_2TiAl. We believe that it is important to understand properties of individual phases so that properties of phase aggregate could be modeled.

Regarding mechanical properties of an alloy with hierarchical microstructures, one fundamental property is single-crystal elastic constants (C_{ij}) as they govern a number of physical and mechanical properties ranging from the stress-strain behavior, dislocation motion, crack nucleation, crack propagation, load partitioning during creep, coherent interfacial energy, strain-induced morphological evolution, etc.

2.2 Simulation Procedure

We note that crystalline materials are in general mechanically anisotropic and the extent of anisotropies could be assessed with a prior knowledge of single-crystal elastic constants. Hence, our goal is to calculate isotropic (polycrystalline) elastic moduli using the homogenization technique. The microstructure of a prototypical alloy exhibiting hierarchical microstructures consists of: BCC-Fe, B2-NiAl, and $L2_1$-Ni_2TiAl.

Phase equilibria in the Al-Ni-Ti system have been summarized, and critical assessments (i.e., based on experimental results) have been published by several authors: Lee and Nash [18], Budberg [23], and Schuster et al. [24]. One exception to these critical assessments is the CALPHAD assessment by Zeng et al [3].

For example, Lee and Nash [18] suggested that $L2_1$-Ni_2TiAl forms by

$$U_2(@1{,}287℃): L + NiAl \rightarrow Ni_3Al + Ni_2TiAl$$

Budberg [23] also proposed the same reaction as by Lee and Nash [18], while Schuster et al [24] proposed that $L2_1$-Ni_2TiAl forms at slightly lower temperatures

$$U_3(@1{,}276℃): L + NiAl \rightarrow Ni_3Al + Ni_2TiAl$$

However, the CALPHAD modeling by Zeng et al [3] predicts quite differently from the other three authors

$$U_7(@1{,}335℃): L + Ni_2TiAl \rightarrow NiTi_2Al_3 + NiAl$$

Due to these invariant reactions, we conclude that the single-phase $L2_1$-Ni_2TiAl cannot be prepared from the melt. We strongly believe that it is the primary reason why there is no experimental single crystal C_{ij} data of $L2_1$-Ni_2TiAl! It is also the reason why computational methods are needed to fill the knowledge gap, i.e., when suitable specimens cannot be prepared by conventional experiments.

With the knowledge of C_{ij}s, there are several approaches to estimate the isotropic elastic limits. These include, among others, methods due to Voigt [25], Reuss [26], and Hill [27]. Voigt's [25] method is based on the assumption of the uniform local strain, $\partial\varepsilon_{ij}/\partial x_k = 0$, where ε_{ij} is the strain tensor, and x is the spatial coordinate, while the Reuss' [26] method is based on the assumption of the uniform local stress, $\partial\sigma_{ij}/\partial x_k = 0$, where σ_{ij} is the stress tensor. Hill showed that Reuss and the Voigt methods yield lower and upper bound, respectively, on effective moduli. The arithmatic mean of Voigt and Reuss bounds has been termed as the Voigt-Reuss-Hill (VRH) bound by Chung [28]. For anisotropic materials, geometric [29] or harmonic means [30] have also been suggested to be useful approximations to effective moduli. Hashin and Shtrikman (HS) [31-33] proposed a method based on variational principles, leading to tighter bounds for isotropic moduli than the Voigt and Reuss averages. Here, the lower and upper HS bounds of elastic moduli are represented as HS(-) and HS(+), respectively.

2.3 Results

Tables 2, 3 and 4 list the Reuss, Voigt, VRH averages, and HS bounds for the effective bulk (B) and isotropic shear (μ) modulus calculated from single-crystal constants of BCC-Fe, B2-NiAl and $L2_1$-Ni_2TiAl, respectively. Usually, B and μ are chosen as the two independent isotropic (polycrystalline) elastic constants. Other elastic constants, such as Young's modulus (E) and Poisson's ratio (v), may be expressed in terms of B and μ using the following relations

$$Y = \frac{9B\mu}{3B+\mu} \tag{6}$$

$$\upsilon = \frac{1}{2}\frac{3B-2\mu}{3B+\mu} \tag{7}$$

The calculated bounds for E and ν are listed in Tables 2 to 4. In BCC-Fe, B2-NiAl and $L2_1$-Ni_2TiAl, we find that the HS bounds lie within the Reuss and Voigt bounds.

Phase equilibria in the Al-Ni-Ti system have been summarized and critical assessments (i.e., based on experimental results) have been published by several authors: Lee and Nash [18], Budberg [23], and Schuster et al. [24]. One exception to these critical assessments is the CALPHAD assessment by Zeng et al. [3].

For example, Lee and Nash [18] suggested that $L2_1$-Ni2TiAl forms by the reaction

$U_2(@1{,}287℃): L + NiAl \rightarrow Ni_3Al + Ni_2TiAl$

Budberg [23] also proposed the same reaction as by Lee and Nash [18], while Schuster et al [24] proposed that $L2_1$-Ni_2TiAl forms at slightly lower temperatures

$U_3(@1{,}276℃): L + NiAl \rightarrow Ni_3Al + Ni_2TiAl$

However, the CALPHAD modeling by Zeng et al [3] predicts quite differently from the other three authors

$U_7(@1{,}335℃): L + Ni_2TiAl \rightarrow NiTi_2Al_3 + NiAl$

Due to the above invariant reactions, the single-phase $L2_1$-Ni_2TiAl cannot be prepared from the melt. We strongly believe that it is the primary reason why there is no experimental single crystal, C_{ij}, data of $L2_1$-Ni_2TiAl! It also underscores why computational methods are needed to fill the knowledge gap, i.e., when suitable specimens cannot be prepared by conventional experiments.

The single-crystal C_{ij} data of Fe were reported by Rayne and Chandrasekhar [34] and polycrystalline properties of BCC-Fe are listed by Simmons and Wang [35]. As seen in Table 2, there is a good agreement between our values and those listed by Simmons and Wang [35].

The single-crystal C_{ij} data of B2-NiAl were reported much later, including our calculations. Consequently, they are not listed in Simmons and Wang's work [35]. In addition, there is another problem associated with B2-NiAl. At low temperatures, due to an ensuing martensitic transformation C_{ij}s could not be measured below 22 ^{o}C. Table 3 lists calculated isotropic elastic constants data of B2-NiAl based on our calculated C_{ij} data at zero K. Isotropic elastic properties of B2-NiAl have been reviewed by Miracle [36] and Noebe et al. [37], and we find that they agree well with our calculated value. For example, Miracle [36] lists isotropic limits of NiAl at 27 ^{o}C as:

E (Young's modulus) = 187.8 GPa

G (Shear modulus) = 71.7 GPa

v (Poisson's ratio) = 0.317

The values of Noebe et al [37] are in good accord with those given by Miracle [36]. Our calculated values [those based on C_{ij} calculated at zero K [VRH and HS(-) limits in Table 2].] are also in good accord with those reported by Miracle [36], and Noebe et al [37].

As mentioned earlier, there is no experimental C_{ij} data of $L2_1$-Ni_2TiAl. Nevertheless, Table 4 lists computed values of isotropic elastic properties of $L2_1$-Ni_2TiAl.

2.4 Conclusion

We have calculated the isotropic elastic properties of phases observed in a prototypical alloy exhibiting a hierarchical microstructure: BCC-Fe, B2-NiAl, and $L2_1$-Ni_2TiAl. Among these, the single-crystal C_{ij} data is available for BCC-Fe and B2-NiAl. However, C_{ij} data of $L2_1$-Ni_2TiAl is not currently available. We strongly believe that the primary reason being: $L2_1$-Ni_2TiAl forms by the U-type reaction in the Ni-Ti-Al system during solidification. However, it may be possible to prepare polycrystalline specimens of Ni_2TiAl by means of conventional solidification and casting. This arrangement would then allow us to measure isotropic elastic constants and verify calculated properties.

Table 2. Calculated isotropic elastic properties of BCC-Fe. Bulk, shear, and Young's modulus are in GPa, compared with data listed by Simmons and Wang [35] in brackets.

	Ruess ([35])	Voigt ([35])	VRH ([35])	HS(-) ([35])	HS(+) ([35])
Bulk modulus	178.19 (173.1)	178.19 (173.1)	178.19 (173.1)	178.19 (173.1)	178.19 (173.1)
Shear modulus	78.33 (79.7)	80.58 (94.1)	79.48 (N/A)	79.45 (86.0)	79.60 (88.5)
Young's modulus	182.18 (207.4)	186.73 (239.1)	184.52 (N/A)	178.19 (221.4)	178.19 (226.8)
Poisson's ratio	0.308 (0.300)	0.303 (0.270)	0.306 (N/A)	0.306 (0.287)	0.305 (0.282)

Table 3. Calculated isotropic elastic properties of B2-NiAl. Bulk, shear, and Young's modulus are in GPa.

	Ruess	Voigt	VRH	HS(-)	HS(+)
Bulk modulus	159.42	159.42	159.43	159.42	159.42
Shear modulus	65.45	101.32	83.39	78.33	88.29
Young's modulus	153.52	222.95	189.35	179.94	198.76
Poisson's ratio	0.319	0.238	0.277	0.289	0.266

Table 4. Calculated isotropic elastic properties of $L2_1$-Ni_2TiAl. Bulk, shear, and Young's modulus are in GPa.

	Ruess	Voigt	VRH	HS(-)	HS(+)
Bulk modulus	166.22	166.22	166.22	166.22	166.22
Shear modulus	53.88	66.03	69.95	59.19	61.51
Young's modulus	129.66	155.49	163.59	141.09	146.02
Poisson's ratio	0.354	0.324	0.315	0.341	0.335

3. First-principles Study of Interfacial Properties

Since there are three hetero-phase interfaces in a hierarchical microstructure involving the disordered matrix (α-Fe or A2) and ordered precipitates of NiAl (B2) and Ni_2TiAl ($L2_1$), we have computed the interfacial energies of Fe/Ni_2TiAl (A2/$L2_1$) and NiAl /Ni_2TiAl (B2/$L2_1$) within the sharp interface approximation. Also, we have considered {100}, {110}, and {111} interface habits. We find that Fe/B2 interfacial energies are much higher than B2/$L2_1$. The investigation of the electronic basis of these results would require additional studies.

3.1 Introduction

One of our goals is to employ science-based systems engineering along with modern computational tools to design the Fe-based superalloy. In the present research, alloys are sought, which gives a relatively-high volume fraction of thermodynamically stable and coherent nano-scale precipitates with the cubic B2 (NiAl-type or B2-type) and/or $L2_1$ (Ni_2TiAl-type or $L2_1$-type) structures in an Fe matrix (A2). Here, we report the results of the coherent interfacial energy calculated from first-principles methods but within the sharp-interface approximation.

It is well known that the interfacial energy between the matrix and precipitate has a strong influence on the nucleation rate and coarsening resistance of precipitates. Usually, the interfacial energy in a two-phase solid-solid system is derived from the coarsening data for precipitates, in conjunction with the Oswald ripening theory [38]. Currently, there is no experimental data of the coherent interfacial energy in a hierarchical microstructure. So, to bridge the knowledge gap, we have employed the first-principles method to estimate various coherent interfacial energies in our model hierarchical microstructure [1, 2]. Specifically, in our hierarchical microstructure, there are coherent interfaces due to NiAl (B2) and Fe (A2), Ni_2TiAl ($L2_1$) and Fe (A2), and NiAl (B2) and Ni_2TiAl ($L2_1$). Another variable in the matrix/precipitate combination is the interface habit. In our model calculations, we have considered only low-index habits, namely, {100}, {110}, and {111}.

To improve the coarsening resistance of coherent precipitates, it is necessary to minimize the interfacial energy. In multi-component systems, it is difficult to assess the effect of various alloying elements on the interfacial energy, using the coarsening data of precipitates. Therefore, we have undertaken a systematic study to compute Fe/B2 and Fe/$L2_1$ interfacial energies from first principles. This arrangement may give us valuable guidelines in the computational design of coarsening resistant alloys.

3.2 Computational Procedure

The VASP software [4-6] was applied in the first-principles calculations, within the framework of the electronic-density-functional theory, employing the projector-augmented wave PAW method [7]. The PAWs employed in the present work explicitly treat three valence electrons for Al ($3d^2 3p^1$), four for Ti ($3d^3 4s^1$), and eight for Fe ($3d^7 4s^1$). A kinetic-energy cutoff of 410 eV was used for the expansion of the electronic wave functions in plane waves. All calculated results were derived, employing the generalized gradient approximation (GGA) for the exchange-correlation functional for exchange-correlation energy due to Perdew [10], a spin polarized Hamiltonian. Brillouin-zone integrations were performed, using Monkhorst-Pack k-point meshes [11], and the Methfessel-Paxton technique with the smearing parameter of 0.1 eV [12].

For the Fe/B2 model systems with the {100} habit, we have constructed supercells containing 8 to 32 atoms to test the convergence of the total energy with respect to the supercell size. Specifically, they correspond to $1 \times 1 \times 4$, $1 \times 1 \times 6$, $1 \times 1 \times 8$, and $1 \times 1 \times 16$ supercells of the conventional BCC/B2 unit cell, where one half of the supercell represents Fe and the other half represents the B2 phase. However, only one such test was done for the Fe/NiAl system with the {110} habit.

For the Fe/$L2_1$ model systems with {100} habit, we have constructed supercells containing 128 atoms, which correspond to $2 \times 2 \times 16$ supercells of the conventional BCC unit cell, or $1 \times 1 \times 8$ supercells of the conventional $L2_1$ unit cell.

At T = 0 K, the interfacial energy is the difference between the total energy of the combined system (the matrix + precipitate) and the total energies of the separated bulk parts. For example, in the case of Fe/B2 systems containing n unit cells of Fe (nFe) and B2 (nB2) phases, the interfacial energy is given by

$$\gamma = \Big(E_{Fe/B2}[n_{Fe}, n_{B2}] - 0.5(E_{Fe}[2n_{Fe}] + E_{B2}[2n_{B2}])\Big)/2A \qquad (8)$$

where E is the total energy, and A is the interfacial area. Analogous relations may also be defined for Fe/$L2_1$ and B2/$L2_1$ systems.

3.3 Results

Atomic-scale models of Fe/Ni_2TiAl and NiAl/Ni_2TiAl are shown in Figures 1 and 2.

Resulting calculated interfacial energies are shown in Figures 3 and 4. Figure 3 shows the calculated interfacial energy of the Fe/Ni_2TiAl system as a function of the supercell size (in terms of numbers of BCC unit cells to represent interfaces having for both {100} and {110} habits). Due to the spin-polarized nature, relevant calculations become expensive as the size of the supercell increases.

As implied in Figures 3 and 4, calculated interfacial energies at 0 K are much smaller for NiAl/Ni_2TiAl (Figure 4) than Fe/Ni_2TiAl (Figure 3). We note that the latter require the evaluation of the interfacial energy using a much larger supercell. Also, to investigate the electronic basis of the interfacial energy would require additional studies.

As a closing note, as mentioned in introduction, we have presented the values of coherent interfacial energies in a hierarchical microstructure within the sharp interface approximation where atoms are not allowed to migrate across the interface. Doing so would require cluster expansion as has been demonstrated for the case of Ni/Ni_3Al [39], i.e., in a γ-γ' model system. In addition, the experimental data is needed to verify some of the predicted results.

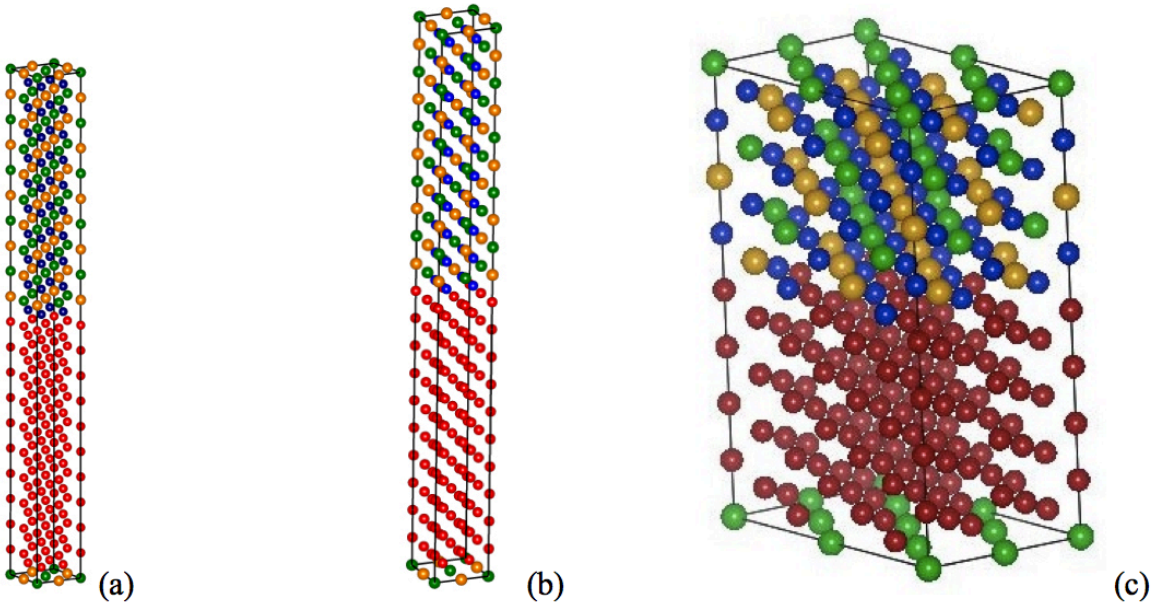

Figure 1. Atomic-scale model of Ni_2TiAl Fe/($L2_1$) coherent interfaces: (a) {100} habit with 160 atoms, (b) {110} habit with 160 atoms, and (c) {111} habit with 192 atoms. In each case, the bottom half represents BCC-Fe (A2), and the top half represents Ni_2TiAl ($L2_1$). Red represents Fe atoms, Blue represents Al atoms, Yellow represents Ti atoms, and Green represents Ni atoms.

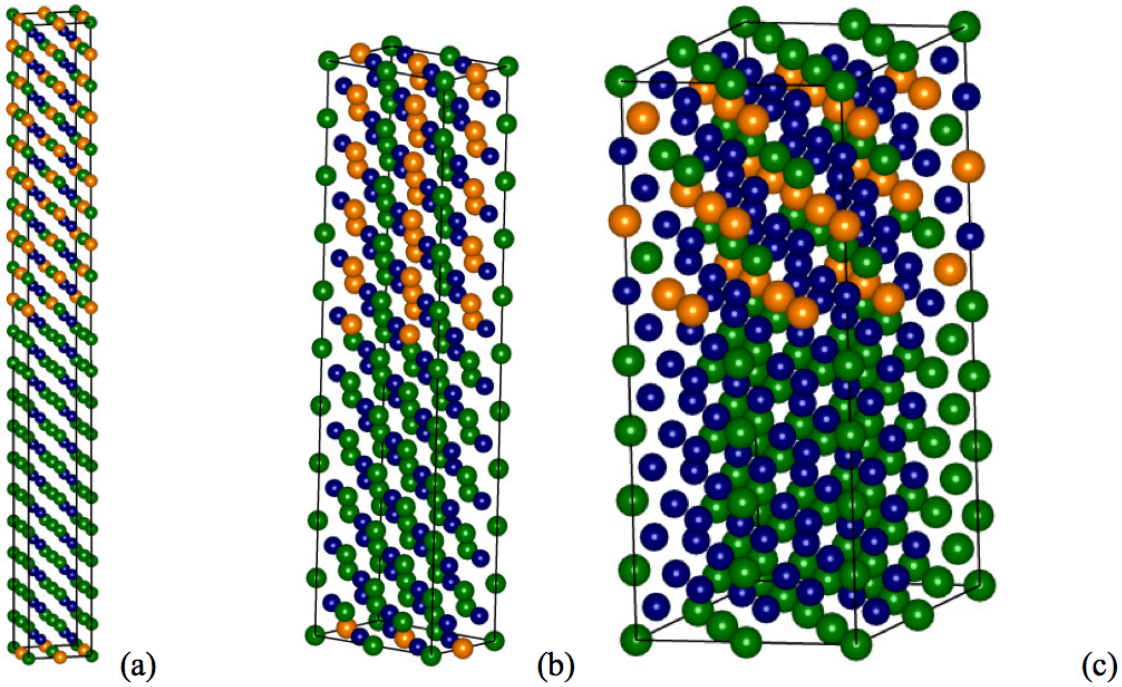

Figure 2. Atomic-scale model of NiAl (B2)/Ni_2TiAl ($L2_1$) coherent interfaces: (a) {100} habit with 160 atoms, (b) {110} habit with 160 atoms, and (c) {111} habit with 192 atoms. Here, the bottom half represents NiAl (B2), and the top half represents Ni_2TiAl ($L2_1$). Green represents Ni atoms. Blue represents Al atoms, and Yellow represents Ti atoms.

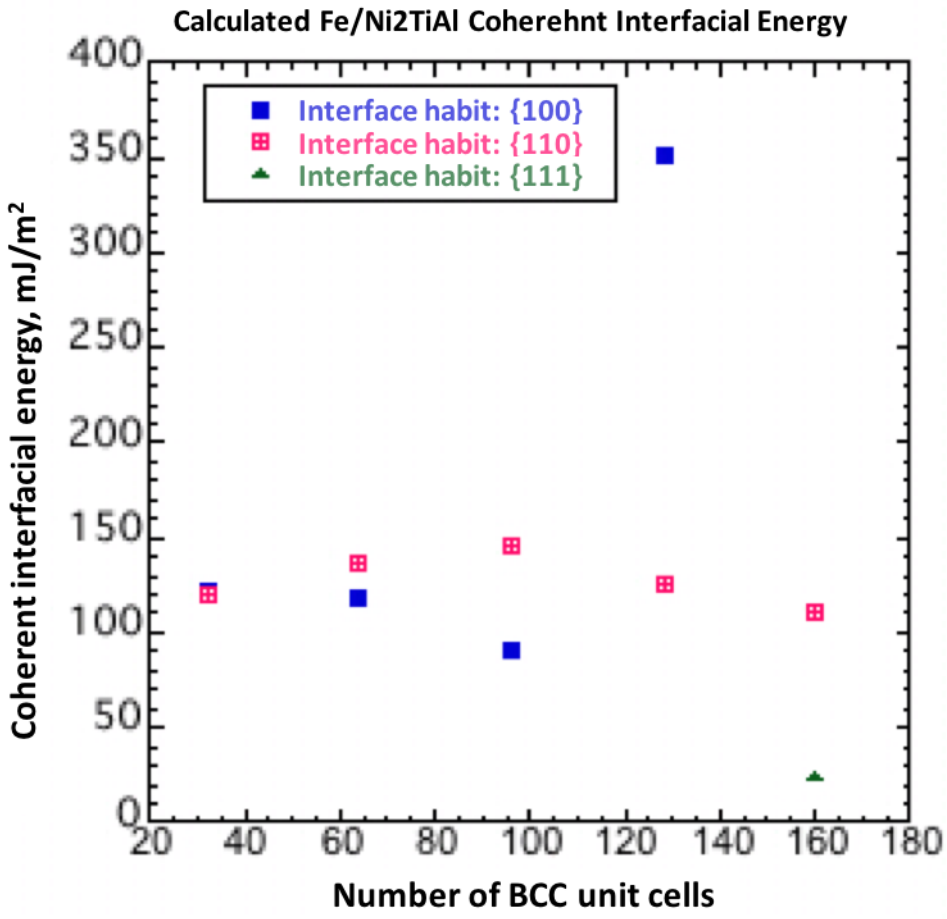

Figure 3. Coherent interfacial energy (calculated), at 0 K, of Fe (A2)/Ni_2TiAl ($L2_1$) with different habits.

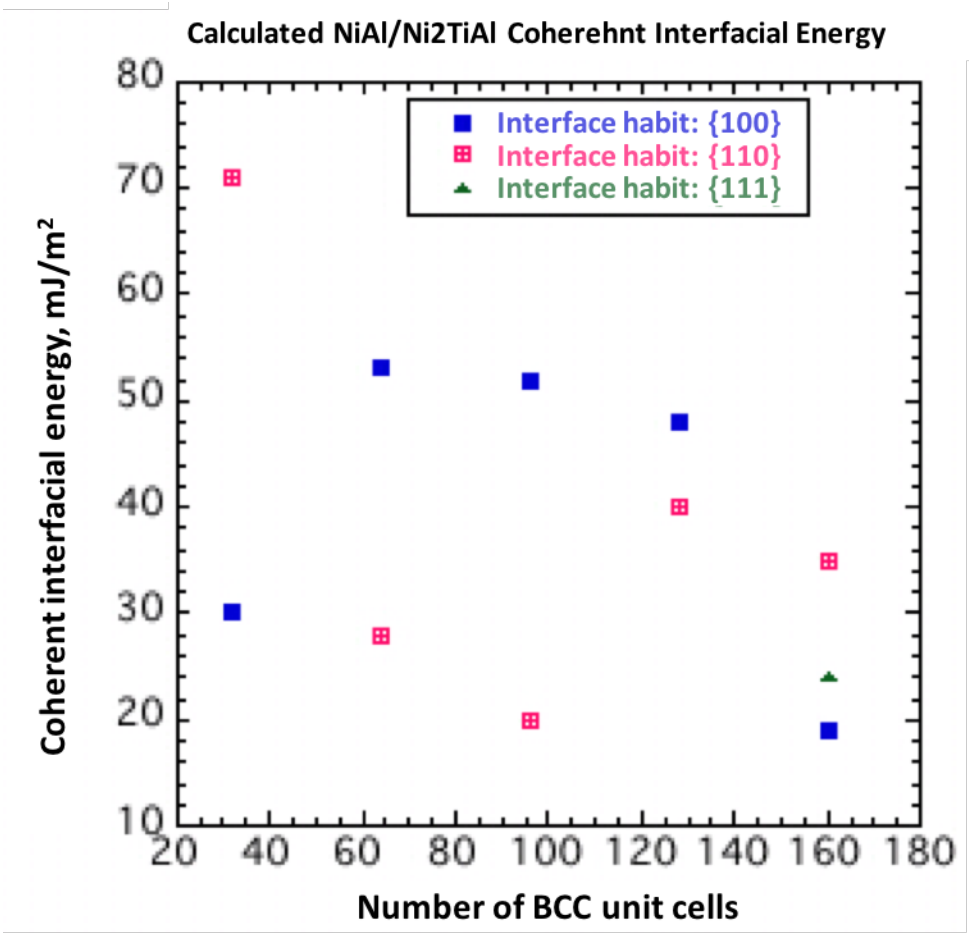

Figure 4. Coherent interfacial energy (calculated), at 0 K, of NiAl (B2)/Ni_2TiAl ($L2_1$) with different habits.

4. Design and Fabrication of Model Alloys

Several FBB8-based alloy systems had been investigated in this project, featuring FBB8 + 2% Hf, FBB8 + 2% Zr, FBB8 + 1.5% to 3.5% Ti alloys. The primary expectation for these alloy systems are composed of hierarchical structure precipitates, the same as the FBB8 + 2% Ti alloy. Therefore, by replacing Ti with Hf and Zr (larger atomic sizes), we expecting a stronger lattice mismatch between the precipitates and the matrix, and, hence, further improving the effect of dispersion strengthening. The alteration of the Ti content in the original FBB8 + 2% Ti alloy is for optimizing the creep resistance of the existing alloy system. Current studies show that FBB8 + 2% Ti has greater creep resistance than FBB8 and FBB8 + 4% Ti alloys, because of its $L2_1$/B2 phase hierarchical structure precipitates. However, the optimized ratio of $L2_1$ and B2 phases has not yet been investigated. Therefore, a study of the optimization of Ti content in FBB8 + Ti alloy system had been conducted. Notably, the term [FBB8 + X% A] refers to the FBB8 composition plus X weight percent of the A element, which will be the nomenclature for the whole report. A detailed nominal composition for all the alloys we've studied is listed in Table 5.

4.1 Introduction

The research on the FBB8 + Ti alloys shows that when Ti is added into the FBB8 alloy system, Ti combines with B2-NiAl and coverts into the Heusler phase of Ni_2TiAl ($L2_1$ phase), which further improves the creep resistance of the original alloy. When FBB8 is added with more than 4% Ti, all the B2 phase precipitates convert into the $L2_1$ phase. However, when FBB8 is added with only 2% Ti, it forms precipitates that composed of both the B2 phase of NiAl and $L2_1$ phase of Ni_2TiAl, which is also called a hierarchical-structure precipitate [40, 41]. Alloys strengthened by the hierarchical-structure precipitates have exceptionally-high creep resistance. At 700 ^oC, FBB8 + 2% Ti has a threshold stress of 186 MPa, which is much higher than 71 MPa of the original FBB8. We've compared the creep resistance between FBB8 + 2% Ti (strengthened by hierarchical structure precipitates) and FBB8 + 4% Ti (strengthened by only $L2_1$ phase precipitates), and the alloy that strengthened by hierarchical-structure precipitates apparently has better creep resistance.

Based on this alloy-design concept, Jung et. al [42] published the research related to the solubility of Hf and Zr into B2-TiNi and $L2_1$-Ni_2TiAl, and considered that Hf and Zr, because of the larger atomic radii, have the potential of lowering the lattice misfit between the B2 and $L2_1$

phases, and, therefore, enhance mechanical properties. The results showed that Hf and Zr have the high chance to substitute Ti in both B2 and $L2_1$ unit cells. Therefore, if FBB8 + Hf or FBB8 + Zr form the $L2_1$ phase, the Ni_2HfAl and Ni_2ZrAl could have a lower lattice misfit and enhance the interface coherency. Additionally, Hf and Zr enhance the solubility of Al in the TiNi, creating a more proper environment of forming the $L2_1$ phase.

Also, a systematic study on the FBB8 + Ti alloy system is required, in order to optimize the creep resistance. We've known that the hierarchical-structure precipitate brings superior creep resistance, and the hierarchical-structure precipitate is a combination of two different phases, $L2_1$ and B2 phases, respectively. Therefore, the volume fraction of each phase could be a critical factor for the creep resistance.

4.2 Procedure

The nominal composition of each alloy is listed in Table 5. As described in the above paragraphs, the nomenclature of the FBB8 + X% A always refers to FBB8 plus X weight percents of the A element. For the rest of the report, all the samples will be named after this nomenclature, unless specifically marked. For example, FBB8 + 2% Hf means FBB8 plus 2 weight percent of Hf. The samples for microstructure characterization are fabricated majorly by an arc-melting method, followed up with an aging procedure that will be described in the following paragraph. After the aging process, samples will be cut into small pieces and polished for the microstructural characterization like SEM, TEM, and/or APT.

Samples for compression tests (including compressive-creep tests) are fabricated by the arc-melting method into a rod shape, with a diameter/length ratio of 1/2. The actual sample dimension that has been fabricated in this project is 4 mm in diameter with 8 mm in length, and 6 mm in diameter with 12 mm in length. The compression samples also aged with the same aging procedure, and then polished for the following tests.

Samples for tension tests (including tensile-creep tests) are fabricated by Sophisticated Alloy Company, and then machined into a specific shape, shown in Figure 5. Tension samples are also aged with the same aging procedure, and then polished for the following tests.

For the aging process, samples are sealed in quartz tubes with vacuum, and then put into furnace under 1,200 ^{o}C for a 30-minute homogenization process, and then aged at 700 ^{o}C for 100 hours.

Table 5. Nominal compositions of the model alloys in weight percent (wt. %)

	Fe	Al	Cr	Ni	Mo	Zr	B	Hf	Ti
FBB8 + 2% Hf	Bal.	6.5	10	10	3.4	0.25	0.025	2	0
FBB8 + 2% Zr	Bal.	6.5	10	10	3.4	2	0.025	0	0
FBB8 + 1% Hf-1%Ti	Bal.	6.5	10	10	3.4	0.25	0.025	1	1
FBB8 + 0.5% Hf-1.5%Ti	Bal.	6.5	10	10	3.4	0.25	0.025	0.5	1.5
FBB8 + 1.5% Ti	Bal.	6.5	10	10	3.4	0.25	0.025	0	1.5
FBB8 + 2.5% Ti	Bal.	6.5	10	10	3.4	0.25	0.025	0	2.5
FBB8 + 3% Ti	Bal.	6.5	10	10	3.4	0.25	0.025	0	3
FBB8 + 3.5% Ti	Bal.	6.5	10	10	3.4	0.25	0.025	0	3.5

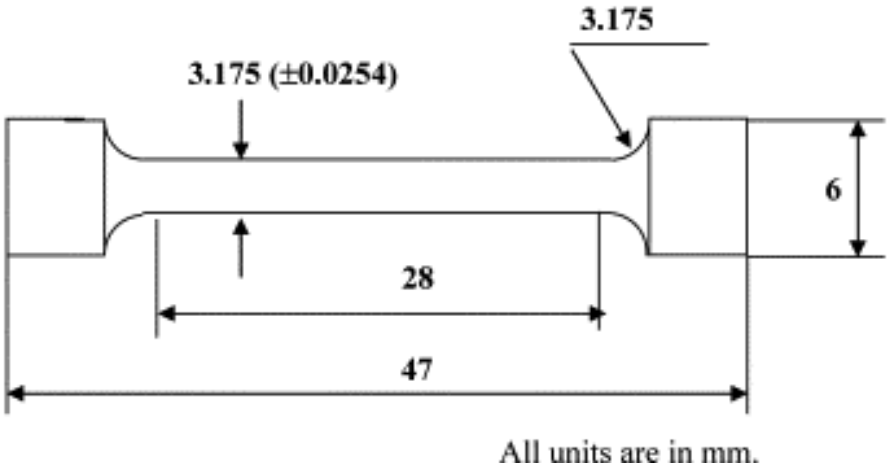

Figure 5. Schematic of tensile test sample geometry.

5. Microstructural Characterization

Several microstructural-characterization techniques had been deployed in this project, including the scanning electron microscopy (SEM), transmission electron microscopy (TEM), atom-probe tomography (APT), and ex-situ neutron diffraction (ND). In this chapter, results obtained from SEM, TEM, and APT will be shown and discussed. Results from ND will be left to the following chapters.

5.1 Introduction

The model alloys are enhanced primarily by the precipitation. Therefore, microstructural information is critical to evaluate the model alloys. The microstructural characterization needs to be able to provide: (1) volume fraction of the precipitation, (2) phase identification, (3) chemical composition in each phase…etc. Hence, several advanced techniques, such as scanning electron microscopy (SEM), transmission electron microscopy (TEM), atom probe tomography (APT), and neutron diffraction (ND) have been employed in this task. Other than experimental techniques, CALPHAD has also taken a role in the prediction and analysis on the microstructure of the model alloys. In general, SEM is able to provide a broader view on the microstructure, and helps in quickly realizing how many different areas exist in the alloys, which might be different phases. TEM provides a much closer view on the microstructure. Especially with the diffraction techniques, TEM is able to give the crystal-structural information of the microstructure. APT is able to provide the chemical composition in different areas (phases) within the alloys, with a very high resolution, which is not able to achieve by normal techniques. The above chemical-composition information help in further confirming the crystal structure of the phases, and the partitioning of the elements within the alloy systems. ND is able to provide diffraction pattern that also offers structural information. Other than TEM, ND provides diffraction data within a relatively larger area, hence, statistically more reliable. The CALPHAD calculation is not a measuring technique, and, however, is able to provide possible phases formed from the thermodynamics' point of view. In the following paragraphs, results obtained from above techniques are presented and discussed, in order to understand the microstructures of the model alloys.

5.2 CALPHAD Calculations

The CALPHAD method is based on the experimental information when the system reaches phase equilibrium, and, therefore, collects all the thermodynamic information from thermochemical and thermophysical studies. The thermodynamic properties for each possible phases are, then, calculated by numerical models, and optimized by adjusting parameters within the numerical models, to best fit the modeling results to the thermodynamic information collected from the experimental data. This process helps in recalculating thermodynamic properties for all phases and, therefore, reliably predict the set of stable phases and their thermodynamic properties in regions that experiments cannot achieve.

There are two factors for the CALPHAD method: Gibbs energies for each phase, the software and the database for calculating results in equilibria. The Gibbs-free energy is essential to determine the phases formed in a certain condition, and from the most experimental data, parameters, such as temperature and pressure, can be obtained or calculated, from the above parameters. The Gibbs-free energy can be, thus, determined. Notably, to obtain an exact description of the behavior of the Gibbs free energy for a multi-component system is not possible. Therefore, the CALPHAD method provides an advantage, for it has the strength to combined several sub-systems to describe the behavior of a multi-component system. In our research of ferritic superalloys, the alloy system usually contains six or more components. Therefore, the CALPHAD method can be used for the formation of phases in our research.

The software for calculating equilibria and databases with the stored assessed information, for calculating equilibria, is the other crucial factor for the CALPHAD method. At present, as there are many different kinds of models used for various phases, there are several thermodynamic databases available, either free or commercially available, for different materials like steels, superalloys, semiconductor materials, aqueous solutions, slags, etc. There are also several different kinds of software available using different kinds of algorithms for computing the equilibrium. It is an advantage if the software allows the equilibrium to be calculated, using many different types of conditions for the system, including not only the temperature, pressure, and overall composition because in many cases the equilibrium may be determined at a constant volume or at a given chemical potential of an element or a given composition of a particular phase.

The CALPHAD calculation results are shown in Figures 6 and 7. From Figure 6, it shows that in the system of FBB8 + 2% Ti, both $L2_1$ and B2 phases form, which fits our previous

observations on FBB8 + 2% Ti samples, which shows that the hierarchical ($L2_1$/B2) structure precipitates exist. Figure 7 presents that in the FBB8 + 2% Zr system, there won't be the $L2_1$ phase formed, instead there will be Laves phases formed. Unfortunately, currently there is no Hf data within the database. Therefore we cannot calculate the phases formed within the FBB8 + 2% Hf system. The CALPHAD method seems to be able to provide reasonable predictions for our research. The FBB8 + 2% Ti prediction indicates the existence of the hierarchical structure, with predictions of volume fractions (about 7% of $L2_1$ phase and 12% of B2 phase, and, thus, a total of 19% of hierarchical structure precipitates, which fits well with the experimentally-reported number $16.3 \pm 2.3\%$ [40]).

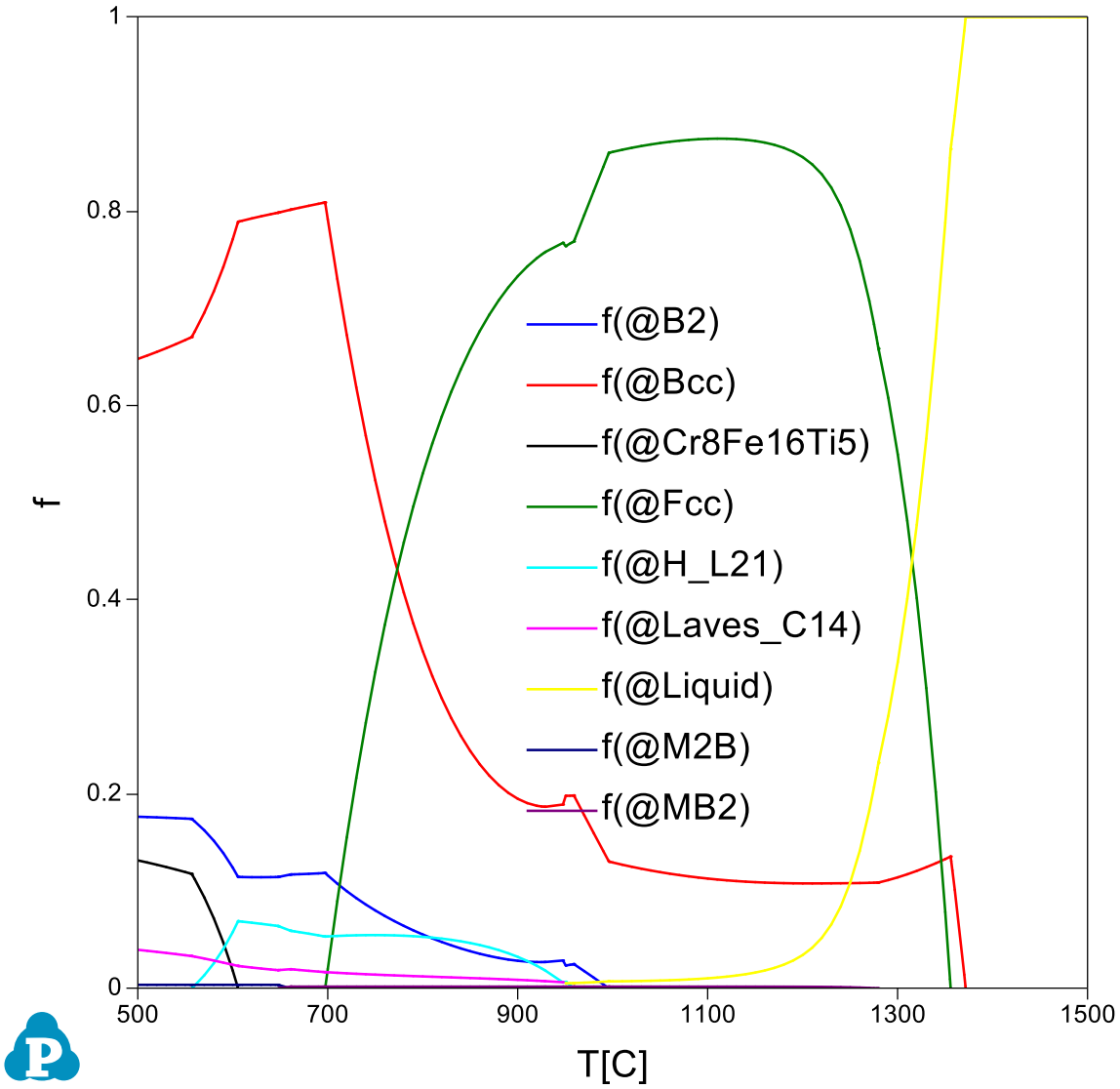

Figure 6. The volume fraction of each possible phase versus temperature plot for the FBB8 + 2% Ti alloy. It can be seen that at 700 ^{o}C, the $L2_1$ phase (a light blue line) and B2 phase (a blue line) coexisted. This prediction fits our observations on the FBB8 + 2% Ti alloy [40].

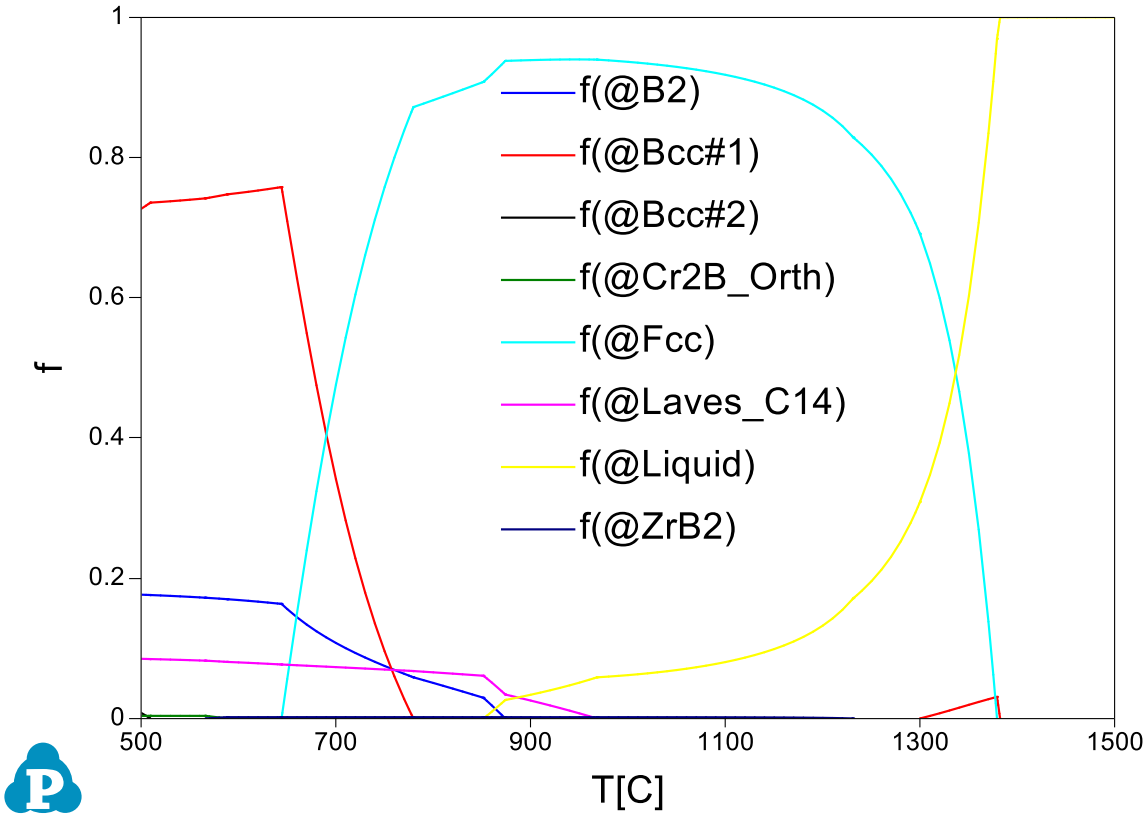

Figure 7. The volume fraction of each possible phase versus temperature plot for the FBB8 + 2% Zr alloy. Within this system, the prediction shows that no $L2_1$ phase formed in the temperature region between 500 ^{o}C to 1,500 ^{o}C. Instead, at 700 ^{o}C, there is Laves phase (pink line) formed.

5.3 Results from FBB8 + 2% Hf and FBB8 + 2% Zr Alloys

Due to the Hf's position below titanium in the same elemental group on the periodic table and a known miscibility gap among Hf, Ni, and Al described in the literature [42], it was hypothesized that the addition of Hf could yield a similar precipitate structure ($L2_1$) to the structure that was previously observed when an equal amount of Ti was added to the same FBB8 system. These samples were homogenized and then aged, following the same aging process described in chapter 4. The investigation of the microstructure of this alloy by means of SEM was performed, using a Hitachi 3400 located at Northwestern University. Figure 8 displays a micrograph of the FBB8 + 2% Hf. In Figure 8, a continuous film of various thicknesses is observed along the grain boundary. The brighter z-contrast of the film, as compared to the surrounding matrix, suggests that the film is mainly composed of heavier elements than the matrix. However, relatively-small visible areas of the film make obtaining a reliable composition from Energy-dispersive spectroscopy (EDS) difficult. In addition, Figure 8 shows the presence of several large (~ 10 - 15 μm radius) and small (> 1 μm) high z-contrast phases that have precipitated throughout the grain. The large precipitates appear with several different internal microstructures that vary from one continuous phase to multiple different contrast phases present in the same large precipitate, although all the precipitates seem to mostly have the same z-contrast, which has a similar brightness to the film found at grain boundaries. Figures 9 and 10 show microstructures that are congruent with that observed in Figure 8. This trend suggests that there is super-saturation of a heavy element (mostly likely Hf in this case) in the matrix, which is precipitating out in the grain and along the grain boundary. Preliminary creep testing performed at The University of Tennessee demonstrates that the FBB8 + 2% Hf alloys has creep strength lower than any of the titanium-containing alloys and on par with the base FBB8 alloy. This relatively-low creep resistance can be expected as the detrimental effects of continuous grain-boundary films on an alloy's overall mechanical properties is well established for many systems [43].

For the FBB8 + 2% Zr alloy, the alloy sample had been aged under the same aging process described in Chapter 4. The aged alloy samples were then examined by SEM to investigate its microstructure.

The SEM images of FBB8 + 2% Zr are shown in Figures 11 to 13. In Figure 11, a general view of the microstructure of the FBB8 + 2% Zr alloy is demonstrated. Similar with the FBB8 + 2% Hf alloy, there is also a dispersion of precipitates formed within grains and also along the grain

boundary, which might suggest that the phases formed within the FBB8 + 2% Hf alloy system is similar with the FBB8 + 2% Zr alloy system. Since CALPHAD calculations for the FBB8 + 2% Hf alloy system is not available due to the lack of datasets in the database, the similarity of the microstructure within both alloy systems could be an analogy. In Figure 12, a closer view of the microstructure of the FBB8 + 2% Zr alloy is shown, which shows that those precipitates with the high Z-contrast have both clear, straight edges and blurred, curvy edges. In the CALPHAD calculation of the FBB8 + 2% Zr alloy, it indicates that while cooling down from 1,200 °C to the room temperature, liquid phase transformed into other phases. Precipitates with blurred and curvy edges might be formed from the liquid phase during the cooling process. According to the CALPHAD calculation, these precipitates with the high Z-contrast could be the Laves phase (C14) $ZrCr_2$ and/or $ZrFe_2$ [44]. In Figure 13, a SEM image with the highest magnification is shown. Within the matrix, it shows a clear view that there are many black, spherical dots. These dots could be the B2 phase precipitates which the FBB8 alloy originally has. The spherical shape of these precipitates suggests that the interface between the precipitate and the matrix is semi-coherent, and, therefore, it could be the B2 phase within the FBB8-based alloy system [40].

From the SEM images, the microstructures of these two alloys share the similar pattern, which contains dark, nano-sized particles as precipitates, dispersed everywhere within the matrix, and brighter secondary phases distributed along the grain boundaries and as larger particles (micro-sized) within grains. According to the CALPHAD calculation, we suspect that the dark, nano-sized particle is the B2 phase, and the brighter secondary phase could be the hexagonal Laves phase. Table 6 shows the elemental distribution of each phase within the FBB8 + 2 wt.% Hf alloy. The Laves phase, no matter it is distributed along grain boundaries, or dispersed within grains as micro-sized particles, they have similar chemical compositions. The Laves phase is composed majorly by Fe (52 - 56 at.%) and Hf (13 - 15 at.%), which might indicate that the chemical composition could be $FeHf_2$. The chemical composition within the B2 phase majorly consists of Al (44 at.%) and Ni (47 at.%), with almost equi-molar fractions, which suggests NiAl as a formula. The matrix is majorly composed of Fe (78 at.%) and Cr (12 at.%). Note that Cr is especially enriched within the matrix, rather than other phases.

Table 7 shows the elemental distribution of each phase within the FBB8 + 2 wt.% Zr alloy. Similar to the FBB8 + 2 wt.% Hf alloy, the chemical composition within the Laves phase is majorly

Fe (52 at.%) and Zr (19 at.%). Within the B2 phase, it has the equi-molar of Ni (46 at.%) and Al (45 at.%), Within the matrix, it is majorly composed of Fe (77 at.%) and Cr (12 at.%).

Within all three phases, it is notable that there is always a certain amount of the Fe precent, even within the B2 phase (roughly 8 at.%). The reason for this phenomenum is because the APT data close to the boundary between two phases can be easily mixed. Since the matrix should be composed of majorly Fe, it is easy to include additional Fe counts into the B2 and Laves phases. Another notable problem is, according to the chemical formula of the Laves phase ($FeHf_2$/$FeZr_2$), the atomic percentage of Hf or Zr should be twice more than Fe. However, from both Tables 1 and 2, the atomic percentage of Fe is roughly 2.5 times of Hf/Zr. Figure 14 shows a high-resolution SEM image of the FBB8 + 2 wt.% Hf alloy, which presents that the Laves phase is actually a segregation of many nano-sized particles, not a homogenized bulk particle as we observed using the low-resolution microscope. This segregation of nano-sized particles indicates that the chemical composition of the Laves phase is actually a mixture of the Laves phase and the matrix, and the latter contains a high amount of Fe.

In conclusion, the APT study of both FBB8 + 2 wt.% Hf and FBB8 + 2 wt.% Zr alloys provides the evidence that the additions of Hf and Zr into the FBB8 system do not form the $L2_1$ phase as expected. Instead Hf/Zr forms the nano-sized Laves-phase particles. They segregated and distributed along grain boundaries and within grains.

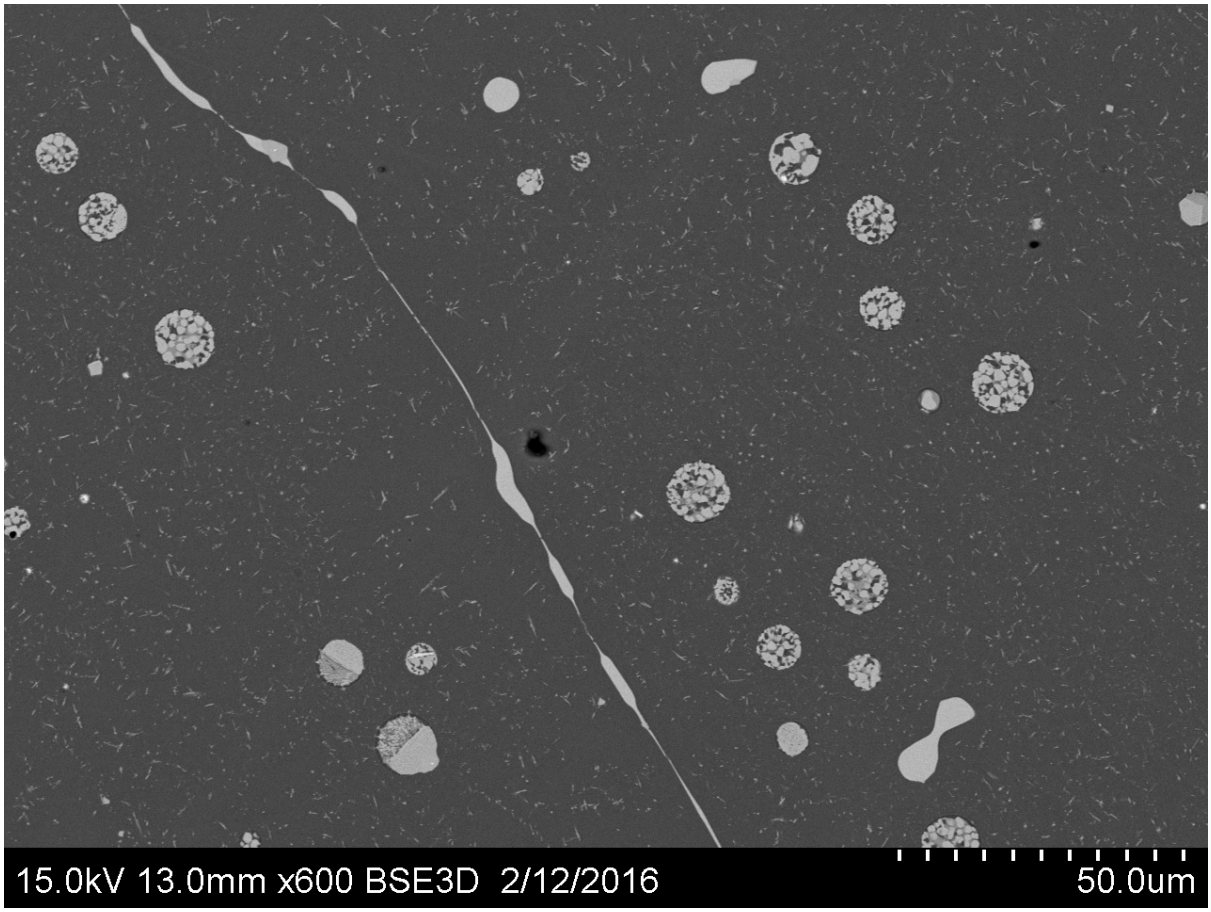

Figure 8. A scanning-electron-microscopy (SEM) image of the FBB8 + 2% Hf alloy displaying a dispersion of large (<r> = ~ 10 - 15 μm) and small (> 1 μm) precipitates in the grain as well as a continuous film at the grain boundary.

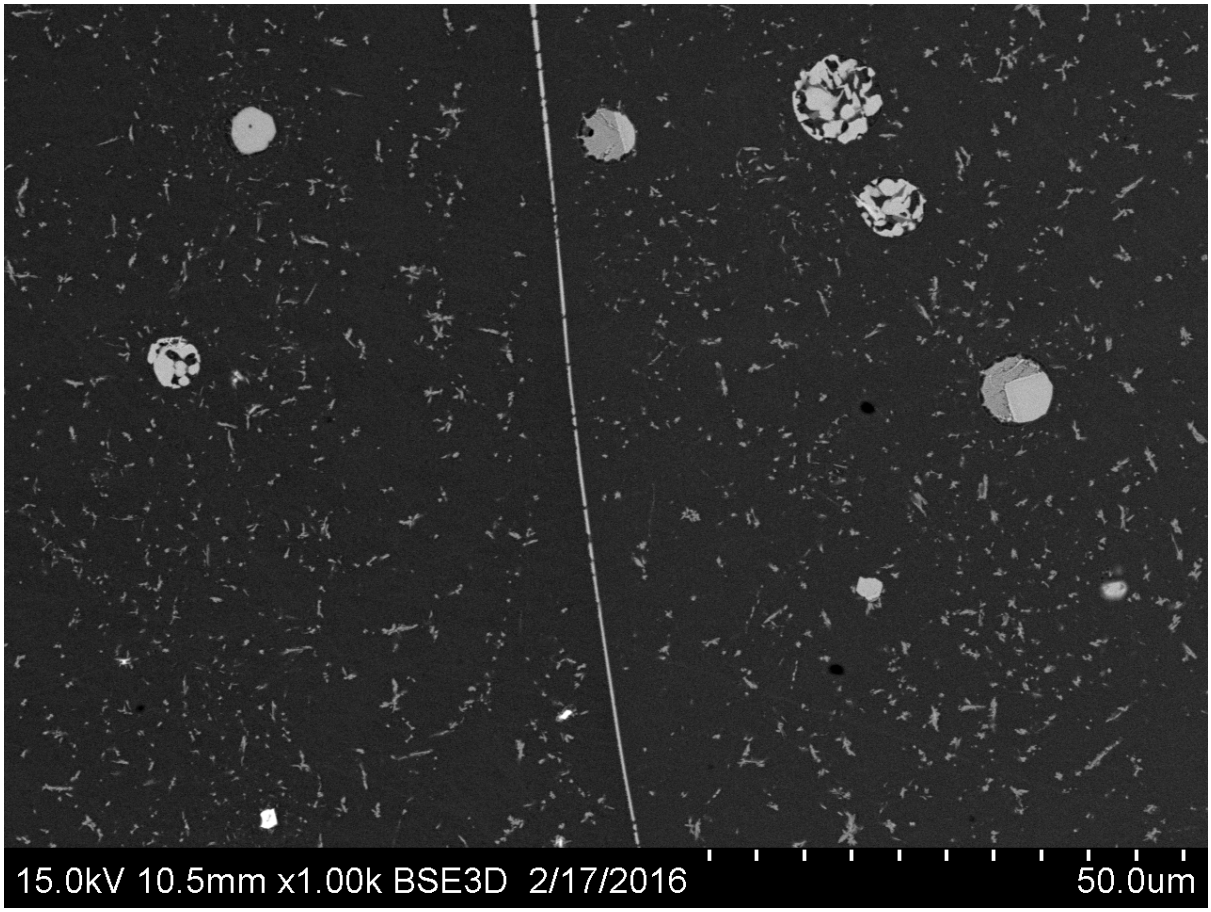

Figure 9. A scanning-electron-microscopy (SEM) image of the FBB8 + 2% Hf alloy displaying a dispersion of large (<r> = ~ 10 - 15 μm) and small (> 1 μm) precipitates in the grain as well as a continuous film at the grain boundary.

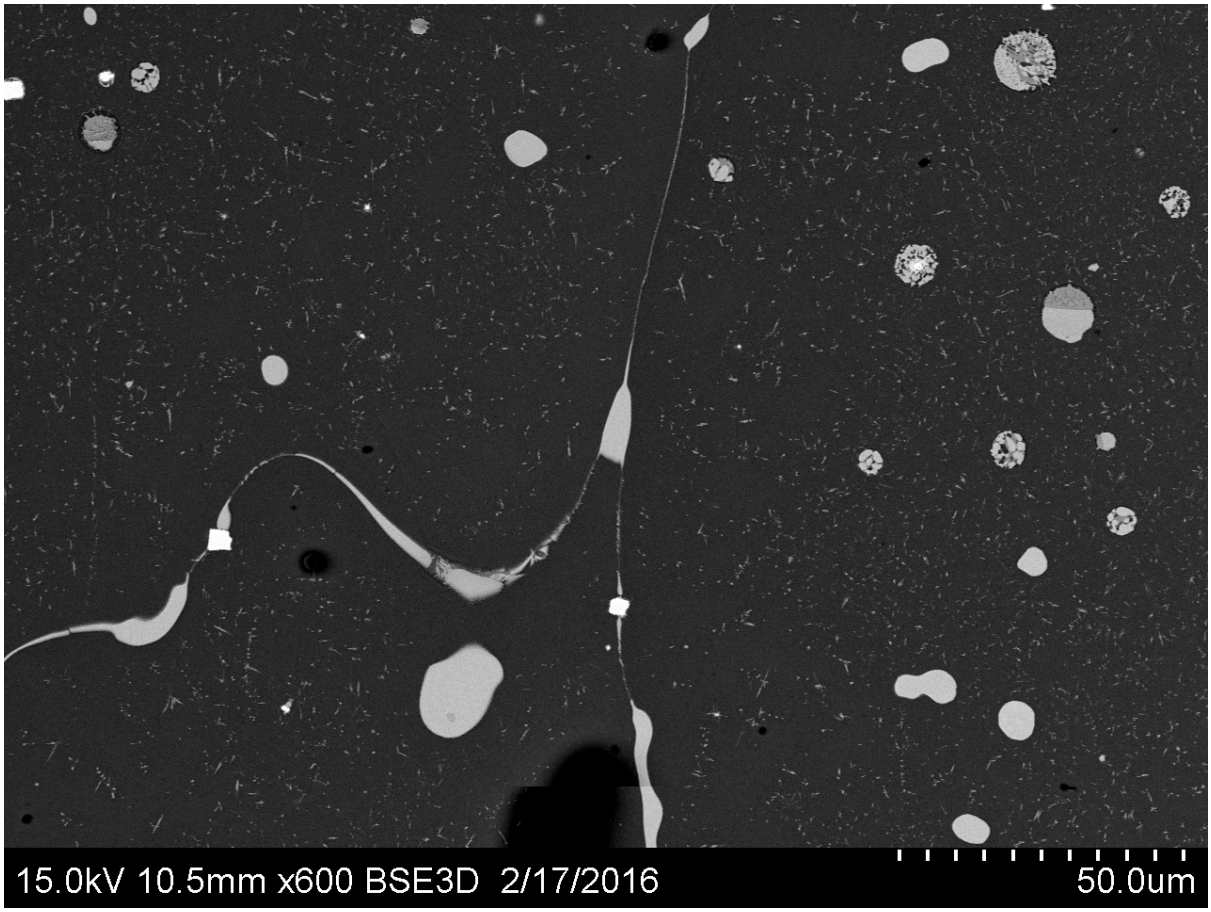

Figure 10. A scanning-electron-microscopy (SEM) image of the FBB8 + 2% Hf alloy displaying a dispersion of large (<r> = ~ 10 - 15 μm) and small (> 1 μm) precipitates in the grain as well as a continuous film at the grain boundary.

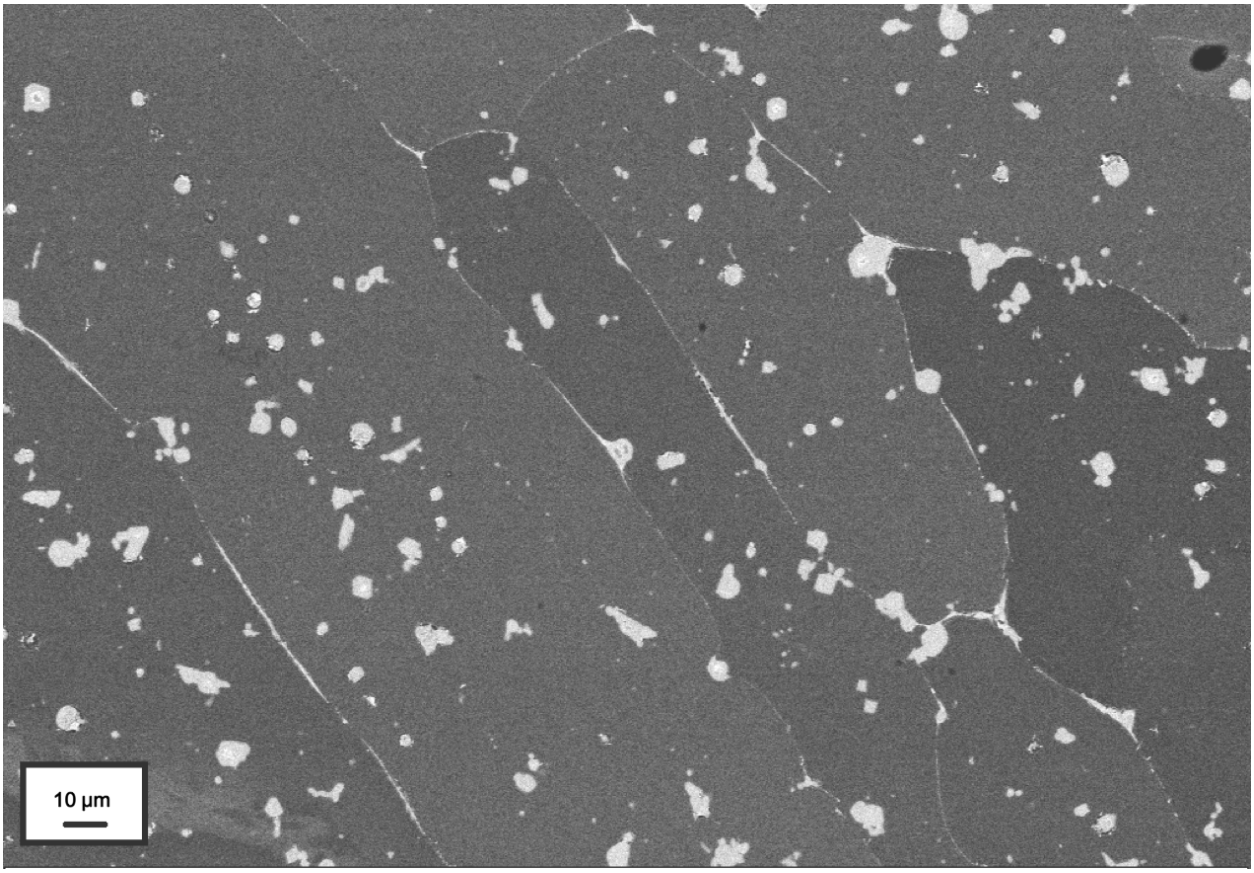

Figure 11. SEM image with a general view of the microstructure of the FBB8 + 2% Zr alloy. Similar to the FBB8 + 2% Hf alloy, a dispersion of precipitates with the high Z contrast (looks white) formed in the grain as well as a continuous film at the grain boundary.

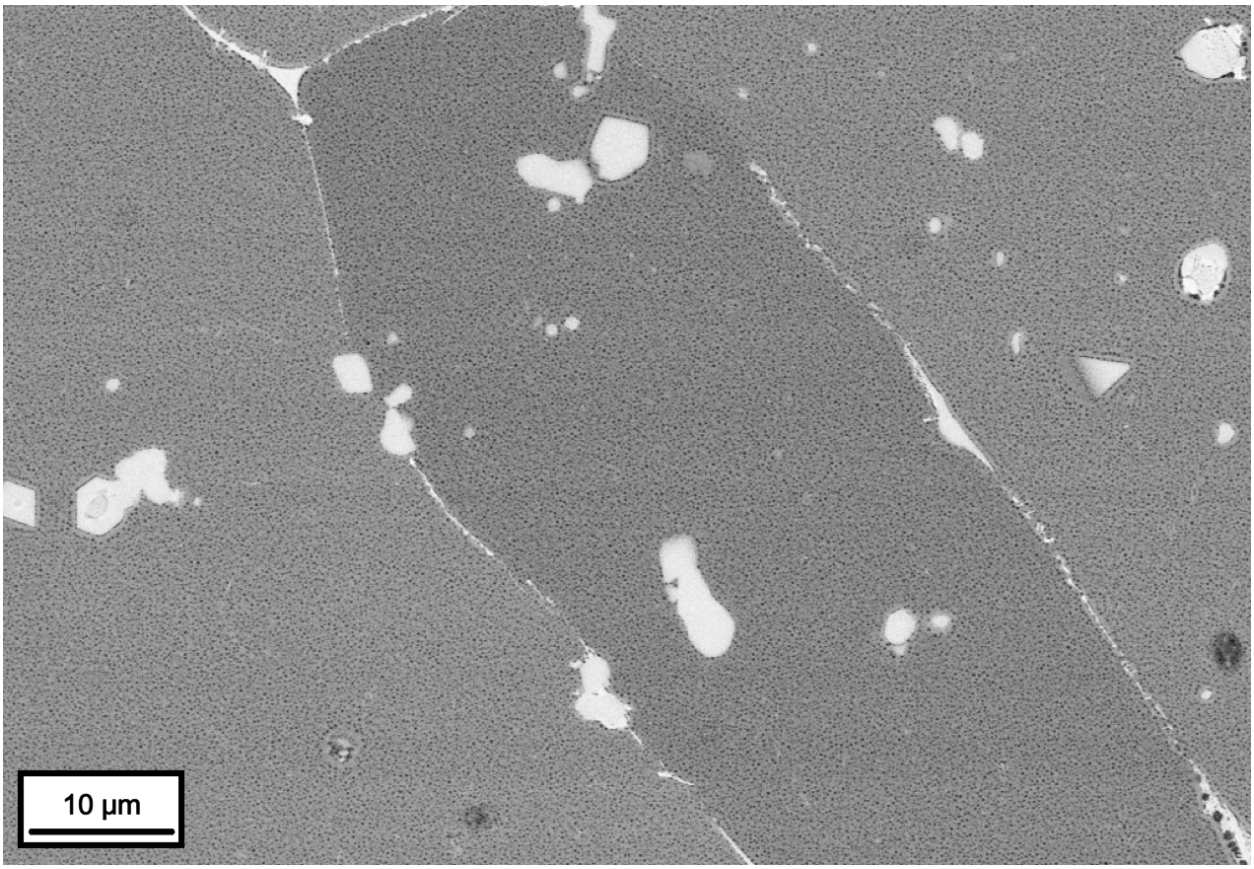

Figure 12. SEM image with a higher magnification of the microstructure of the FBB8 + 2% Zr alloy. Precipitates with the high Z contrast have both clear, straight edges and blurred, curvy edges, which might suggest that those precipitates were the liquid phase during the homogenization at 1,200 °C, and then phase transformed when cooling down to room temperature.

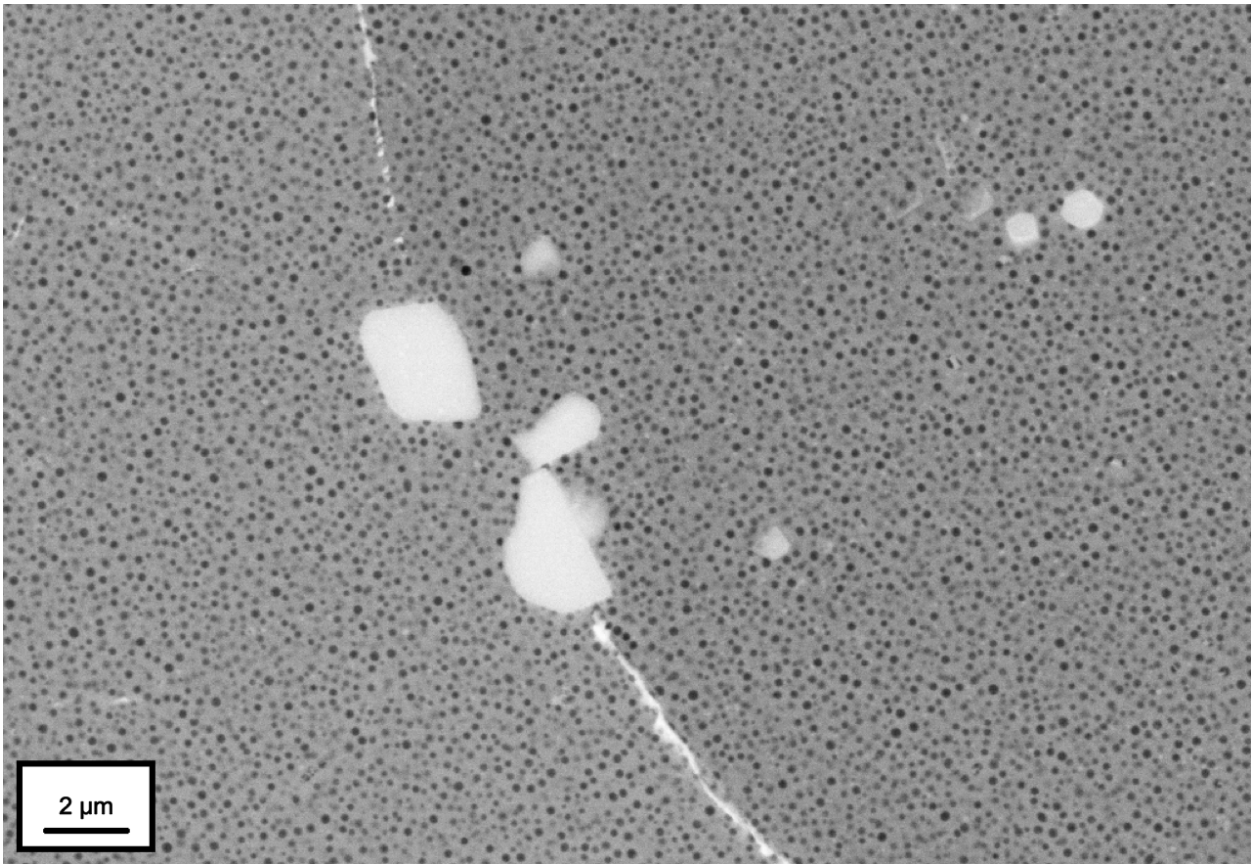

Figure 13. SEM image with an even higher magnification of the microstructure of the FBB8 + 2% Zr alloy. Within the matrix there are black spherical dots, with an average size of 137.5 nm. These dots could be the B2-phase precipitates (NiAl).

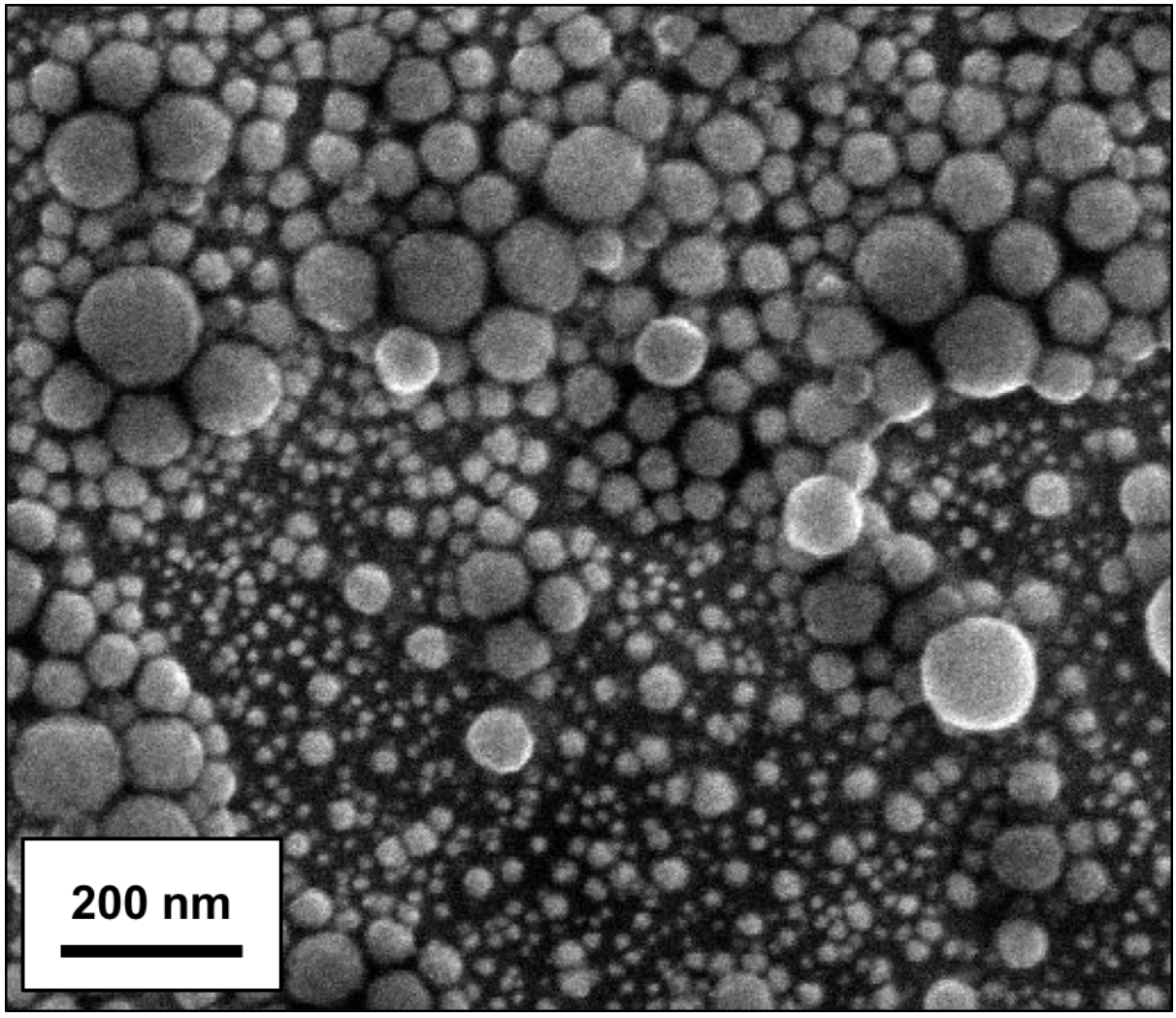

Figure 14. A high-resolution SEM image of the Laves phase within the FBB8 + 2% Hf alloy. The white, nano-sized particles are Laves-phase particles. Unlike the Laves phase shown under low resolution, the Laves-phase region is actually a segregation of nano-sized particles, instead of a homogenized large paricle.

Table 6. Elemental distribution of each phase within the FBB8 + 2% Hf alloy

	Laves Phase @ grain boundary (at.%)	Laves Phase Bulk (at.%)	B2 (at.%)	Matrix (at.%)
Fe	0.52454	0.56331	0.08367	0.77293
Hf	0.13624	0.1495	0.00011	-
Al	0.08331	0.07002	0.44039	0.06558
Ni	0.12625	0.10018	0.47334	0.0193
Cr	0.03833	0.03563	0.00233	0.12344
Mo	0.02484	0.0315	0.00011	0.01727
B	0.00001	-	-	-
Zr	0.05946	0.0473	0.00002	-

Table 7. Elemental distribution of each phase within the FBB8 + 2% Zr alloy

	Laves Phase (at.%)	B2 (at.%)	Matrix (at.%)
Fe	0.5232	0.08815	0.771
Zr	0.19447	0.00007	0.00002
Al	0.10376	0.45322	0.06867
Ni	0.1002	0.45592	0.02019
Cr	0.03303	0.0025	0.12467
Mo	0.0094	0.00013	0.01539
B	0.00055	-	-

5.4 Results for FBB8 + 1% Hf-1% Ti and FBB8 + 0.5% Hf-1.5% Ti alloys

The FBB8 + 1%Hf-1%Ti alloy has been fabricated and aged by the same process mentioned in the Chapter 4. The aged alloy samples then were examined by SEM and TEM to investigate its microstructure. The SEM images are shown in Figures 15 to 17. In Figure 15, a general view of the microstructure of the FBB8 + 1%Hf-1%Ti alloy is demonstrated. Similar with the FBB8 + 2%Hf alloy, there is also a dispersion of precipitates formed within grains and also along the grain boundary. Compared to the FBB8 + 2%Hf alloy, these grain-boundary films are relatively thin, the size of the dispersed precipitates is relatively small, which might be due to the less Hf content. In Figure 16, a closer view of the microstructure of FBB8 + 1%Hf-1%Ti alloy is shown, which is different from that of the FBB8 + 2%Hf alloy. In the FBB8 + 2%Hf alloy, there are many different kinds of precipitates dispersed inside grains and along grain boundaries. However, in the FBB8 + 1%Hf-1%Ti alloy, the microstructure is more uniform, compared to that of the FBB8 + 2%Hf alloy. This trend indicates that adding more Hf into the FBB8 causes the forming of those larger, brighter colored precipitates within grains and grain boundaries. In Figure 17, a SEM image with a closer view of secondary phases is shown. These secondary-phase precipitates have a very different appearance, which is not found in the FBB8 + 2%Hf alloy. There are pore-like structures found within these secondary-phase precipitates in Figure 17, which might be due to the lack of the hot isostatic pressing (HIP) process to eliminate pores inside the material after fabricating samples.

Figures 18 and 19 show the TEM image as well as energy-dispersive x-ray (EDX) spectrometry of the FBB8 + 1%Hf-1%Ti alloy. In Figure 18, precipitates with the size of 100 to 200 nm have been observed and determined by the TEM diffraction. The diffraction result indicates that these nano-sized precipitates are the B2 phase, NiAl. Another proof is from the EDX results shown in Figure 19. In Figure 19, for certain elements, the area with color dots is that of the rich elements, and the black area is that of scarce elements. The quantitative results are listed in Table 8, which shows that the matrix is basically Fe and Cr, which is not surprising for a ferritic alloy, and the precipitate is abundant of Ni and Al. Notably the Hf and Ti concentrations are extremely low in these nano-sized precipitates, which shows that these precipitates cannot be the $L2_1$ phase precipitates or $L2_1$/B2 hierarchical structure precipitates.

The FBB8 + 0.5% Hf-1.5% Ti alloy has been fabricated and aged by the same process mentioned in Chapter 4. In Figure 20, an example of the grain structure present in the FBB8 +

0.5% Hf-1.5% Ti alloy is shown with an average grain size of several hundred microns. It is important to note the we see a vast reduction in both the size and number density of the intergranular, brighter z-contrast (as compared to the surrounding matrix) phases than those observed in the FBB8 + 2% Hf alloy, which was reported last quarter. This trend suggests that the FBB8 + 2% Hf alloy was supersaturated with Hf that resulted in the precipitation of unwanted intergranular phases and, consequently, the the current composition of the FBB8 + 0.5% Hf-1.5% Ti alloy is much closer to the ideal Hf content for our purposes. To confirm this hypothesis, chemical analysis is being performed to confirm the compositions of both alloys to ensure that Hf and Ti are indeed the only elemental quantities that have drastically changed. In Figure 21, which is a higher magnification of the same FBB8 + 0.5% Hf-1.5% Ti alloy, we can see a distinct precipitate structure that is ubiquitous throughout the matrix. These precipitates have an average precipitate radius, <r>, of ~ 95 nm, which is slightly smaller than that of the FBB8 + 2%Ti alloy (<r> = 109nm). In addition, we can see that the high z-contrast phase that decorates the grain boundaries is discontinuous (unlike the continuous film we observed in the FBB8 + 2%Hf alloy), which is preferable for robust high-temperature mechanical properties. This trend is reflected in preliminary creep results that show that the current FBB8 + 0.5% Hf-1.5% Ti alloy is roughly one order of magnitude more creep resistant than the FBB8 + 2% Hf alloy, However, more tests need to be performed to verify these results.

The hierarchical precipitate structures were investigated, utilizing dark-field (DF) images with selected-area-diffraction patterns (SADPs) in TEM. Figure 22 displays SADPs and DF images taken in the near [10-1] zone axis orientation with the (010) reflection for the B2- ordered NiAl and (-11-1) reflection and for the $L2_1$-ordered Ni_2TiAl phase of the FBB8 + 2% Ti and FBB8 + 4% Ti alloys.

The precipitates in Figures 22(a), (b), and (c), displayed in the DF images of the (010)B2 (-11-1) $L2_1$ super-lattice of the FBB8 + 1.5% Ti alloy, show a cuboidal shape with the width ranging from 50 to 100 nm and a spatial arrangement along the <001> direction. From the regions of bright contrast within the precipitates in the DF image, $L2_1$ sub-precipitates hierarchically are embedded within B2 precipitates. The matrix-precipitate and the B2-$L2_1$ interfaces are observed to be coherent with an interfacial alignment toward a cube-on-cube orientation. The DF image of the FBB8 + 1.5% Ti - 0.5% Hf alloy, Figures 22(d), (e), and (f) show a similar feature of the hierarchical structure of the $L2_1$ imbeded in the the B2 structure. The volume fraction of the $L2_1$

phase in the B2 phase are confirmed by the comparison of DF image of the $L2_1$ phase with the B2 phase in both Hf-added and Hf-free specimens. The volume fraction of the $L2_1$ phase is ~ 9.2 % in the Hf-free FBB8 + 1.5% Ti sample. However, it decreases drastically to 4.9 % in the Hf-added FBB8 + 1.5% Ti sample. These fractions are quite small when compared with the FBB8 + 2 wt.% Ti sample, which reported as ~ 50.5% of the $L2_1$ phase in the B2 phase [60].

Figure 23a displays a three-dimensional (3D) reconstruction of an APT analysis of FBB8 + 1.5% Ti - 0.5% Hf, showing B2 and $L2_1$ precipitates enveloped by the green-colored Ni (20 atomic percent, at.%) and red-colored Ti (10 at.%) iso-(concentration) surface, respectively. The iso-surface represents the average of the far-field plateau concentrations of the two phases, by employing the inflection-point methodology [76]. Figure 23b displays an extracted iso-surface image for a clear view of the hierarchical B2/$L2_1$ structure in precipitates with the transparent green Ni and red Ti iso-surfaces. The larger B2 (green iso-surface) precipitate is imbedded a plate-shaped $L2_1$ sub-precipitates (red iso-surface) and shows a hierarchical structures. In the concentration distribution, Fe, Cr, and Mo are strongly partitioned into the matrix, whereas Ni, Al, Ti, and Zr are concentrated in the B2 and $L2_1$ sub-precipitates. Between B2/$L2_1$ phases in the precipitate, Ni and Al are decreased in the $L2_1$ phase, as compared to the B2 sub-precipitates: Ni and Al concentrations decrease to 36.8 and 29.2 at.% in the $L2_1$ phase, from 39.9 and 38.9 at.% in the B2 phase, respectively. Hf is also strongly partitioning to both phases in the precipitate. The concentration ratio of Hf between the BCC-matrix and $L2_1$ is 9.5 ± 2.3, which is larger than that between the B2 and BCC matrix, 7.1 ± 2.4. This preferential partitioning of Hf into the $L2_1$ phase may destabilize the $L2_1$ phase due to the large size of the Hf atom and decrease the volume fraction of the $L2_1$ phase in the precipitate, as measured in the TEM observation.

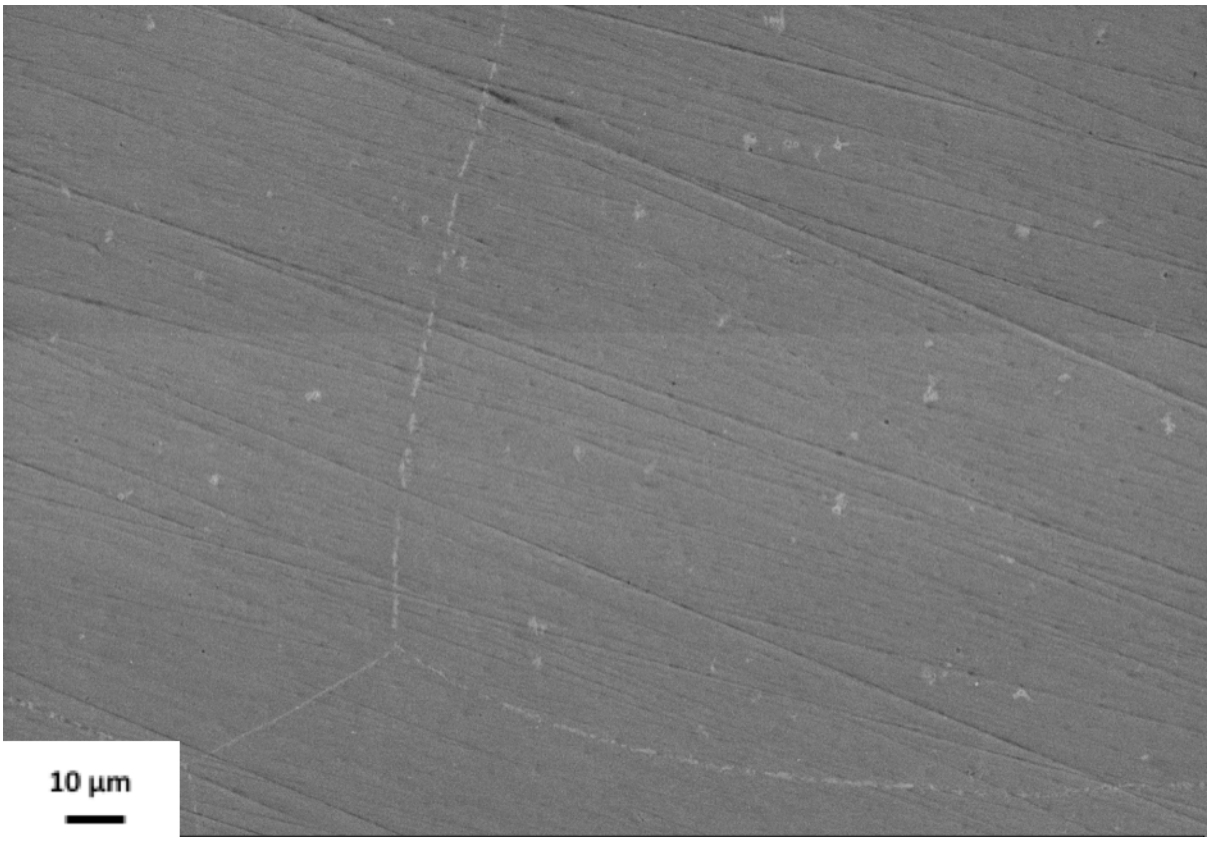

Figure 15. SEM image with a general view of the microstructure of the FBB8 + 1% Hf-1% Ti alloy. Similar to the FBB8 + 2%Hf alloy, a dispersion of precipitates formed in the grain as well as a continuous film at the grain boundary.

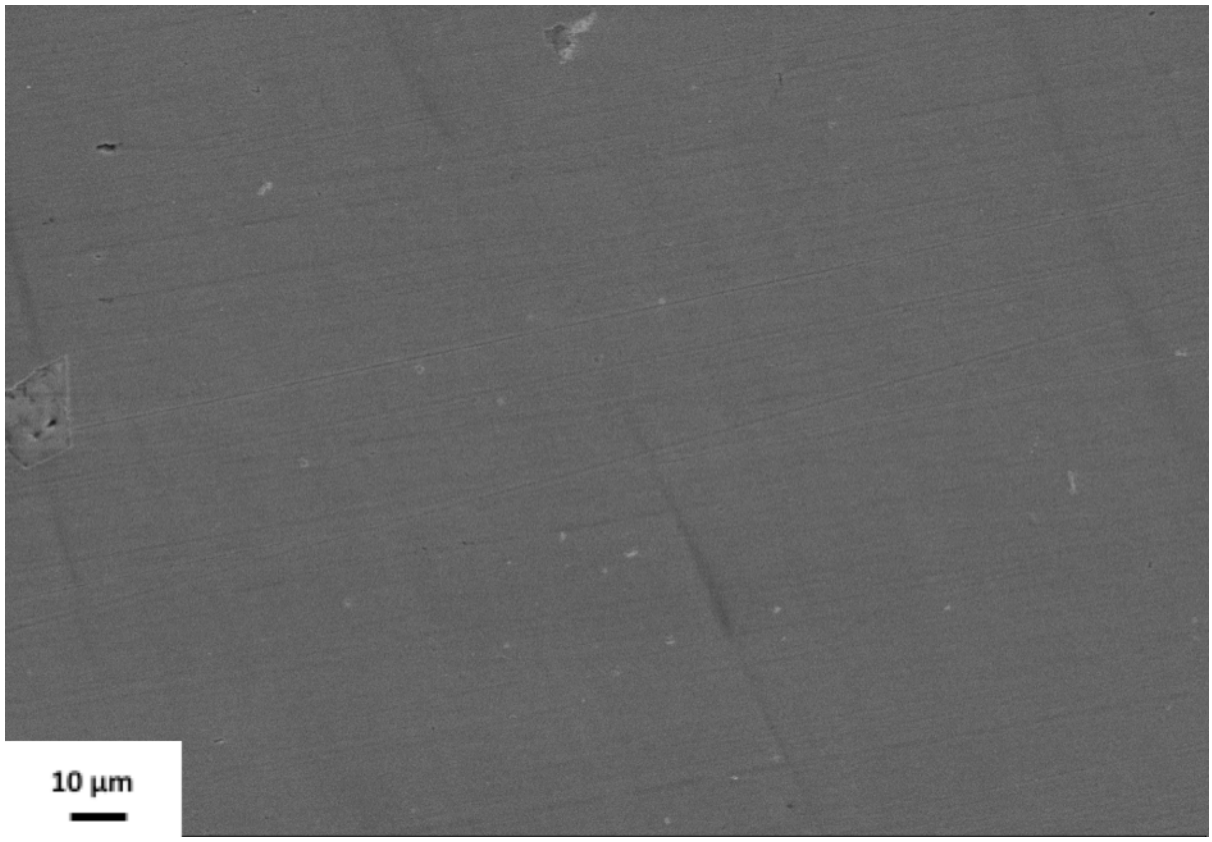

Figure 16. SEM image with a closer view of the microstructure of the FBB8 + 1% Hf-1% Ti alloy. Unlike the FBB8 + 2% Hf alloy, the microstructure of the FBB8 + 1% Hf-1% Ti alloy is more uniform, without many kinds of precipitates (different sizes, different shapes...etc.)

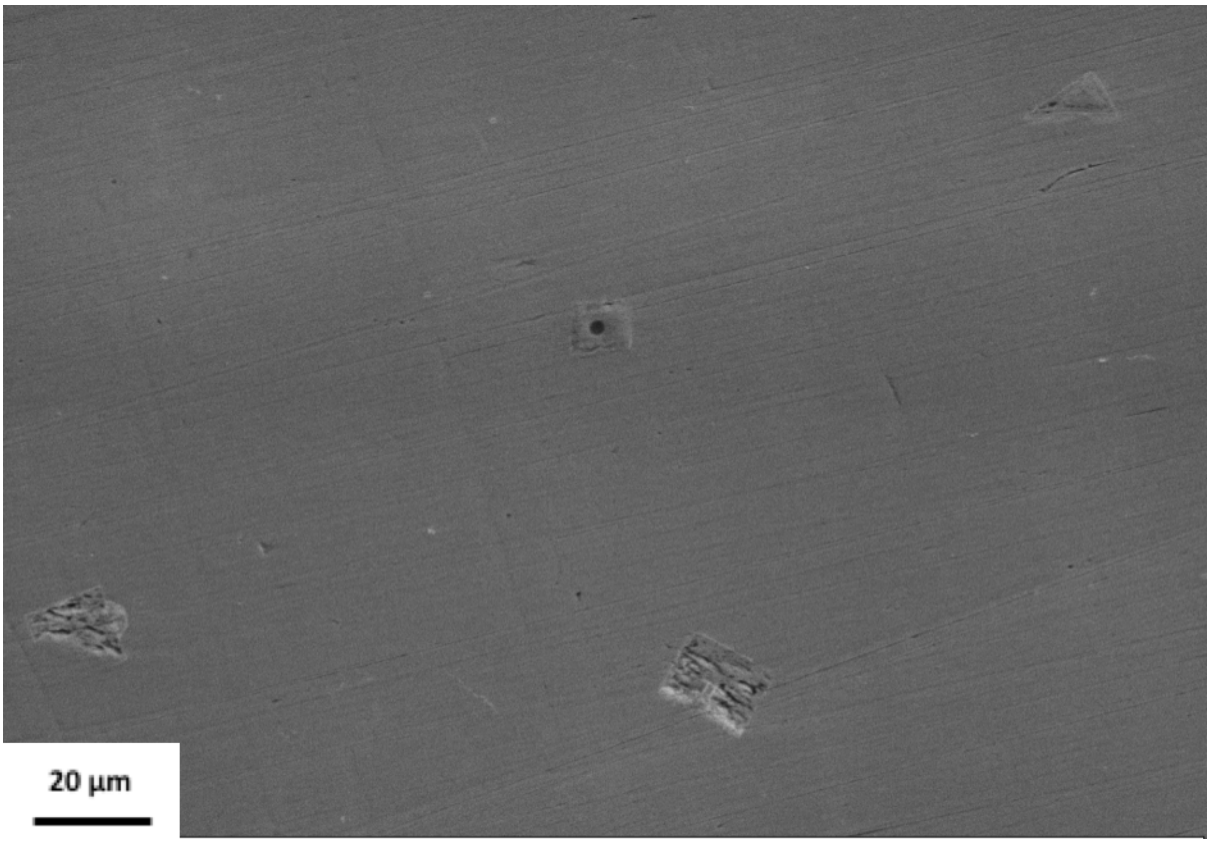

Figure 17. Another SEM image with a closer view of the microstructure of the FBB8 + 1%Hf-1%Ti alloy. There are secondary phases formed with sizes around 12 to 20 µm. These secondary phases seem to have pores inside under SEM.

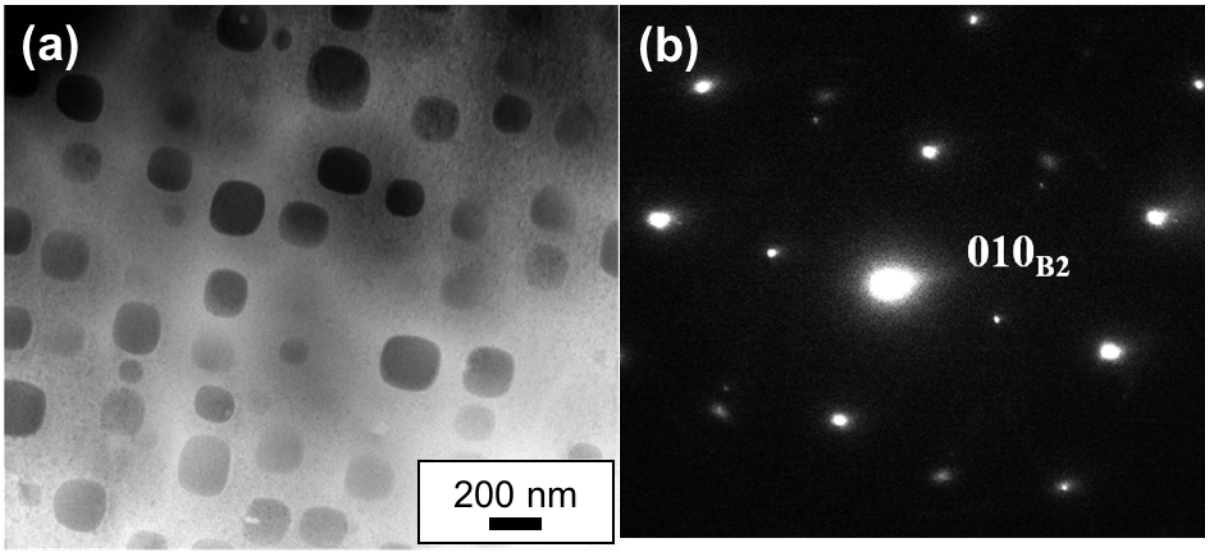

Figure 18. The (a) TEM image and (b) TEM diffraction pattern of FBB8 + 1%Hf-1%Ti alloy. (a) The TEM image shows cuboidal shaped precipitates dispersed within the matrix, with the precipitate size of 100 to 200 nm in diameter. (b) The diffraction pattern shows that these precipitates have a B2-phase structure.

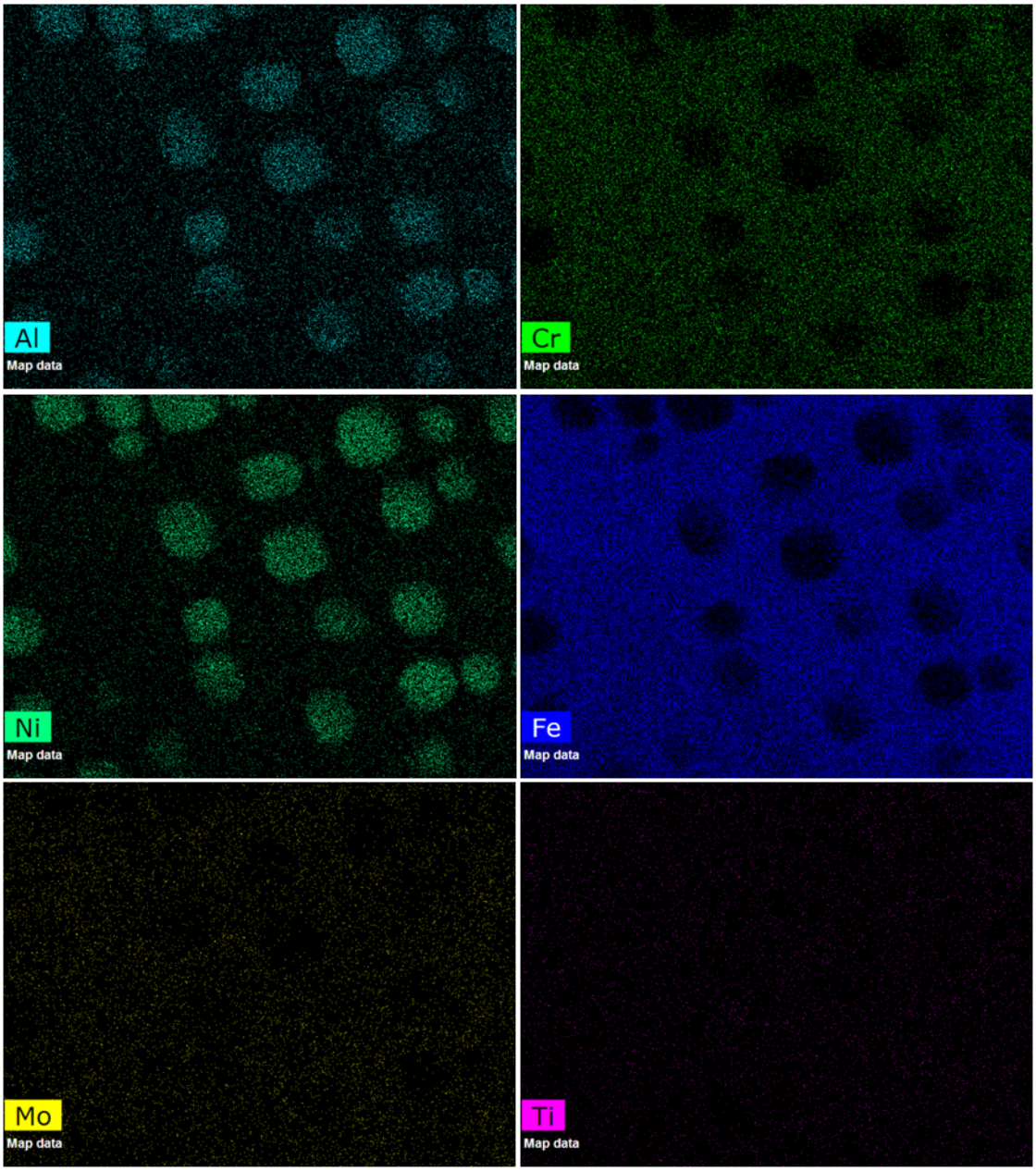

Figure 19. The EDX image for the FBB8 + 1%Hf-1%Ti alloy. The brighter area shows the abundance of certain elements, and the darker area presents the lack of certain elements.

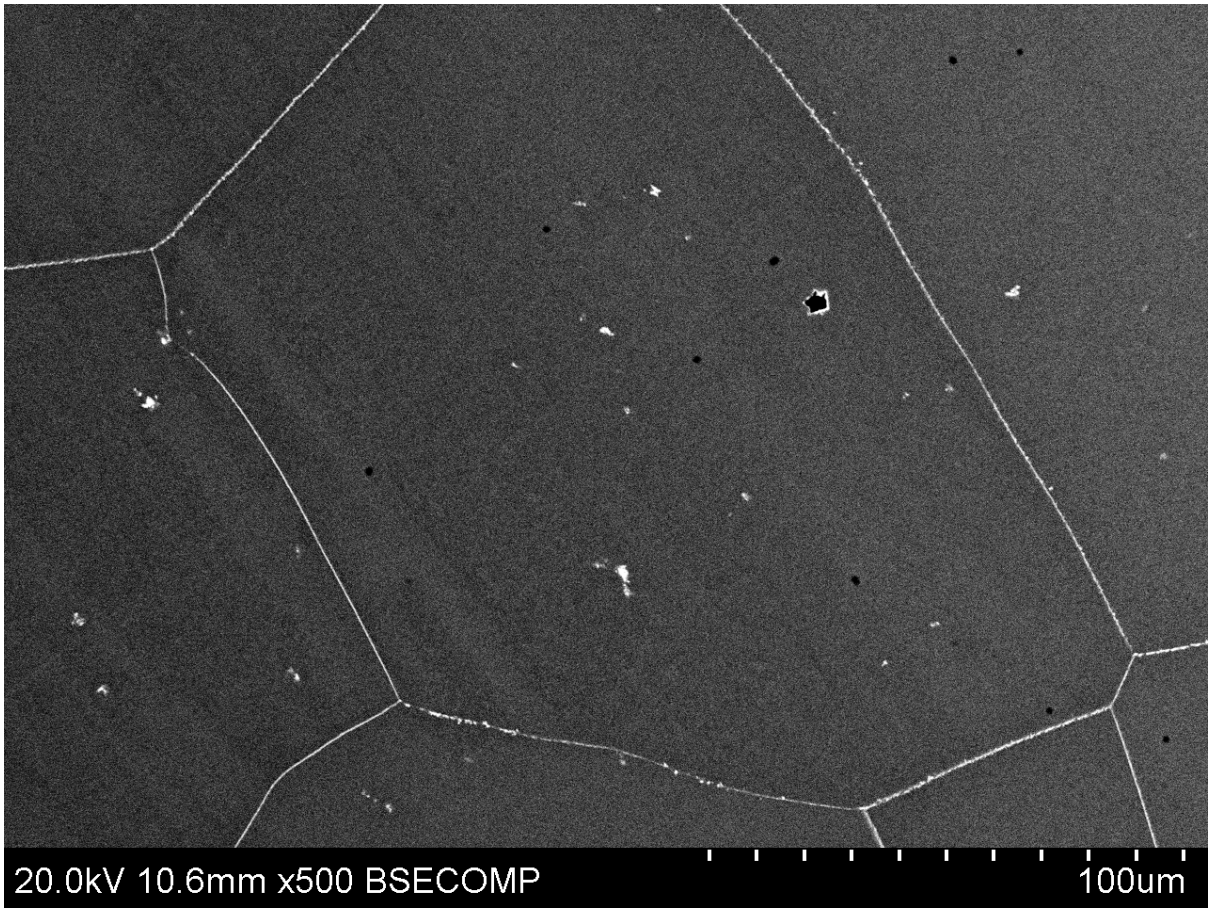

Figure 20. A scanning-electron-microscopy (SEM) image of the FBB8 + 0.5% Hf - 1.5% Ti alloy (taken at 500 times magnification) displaying the grain structure of the alloy (several hundred microns) and high z-contrast phase that are present inside the grains and decorate the grain boundaries.

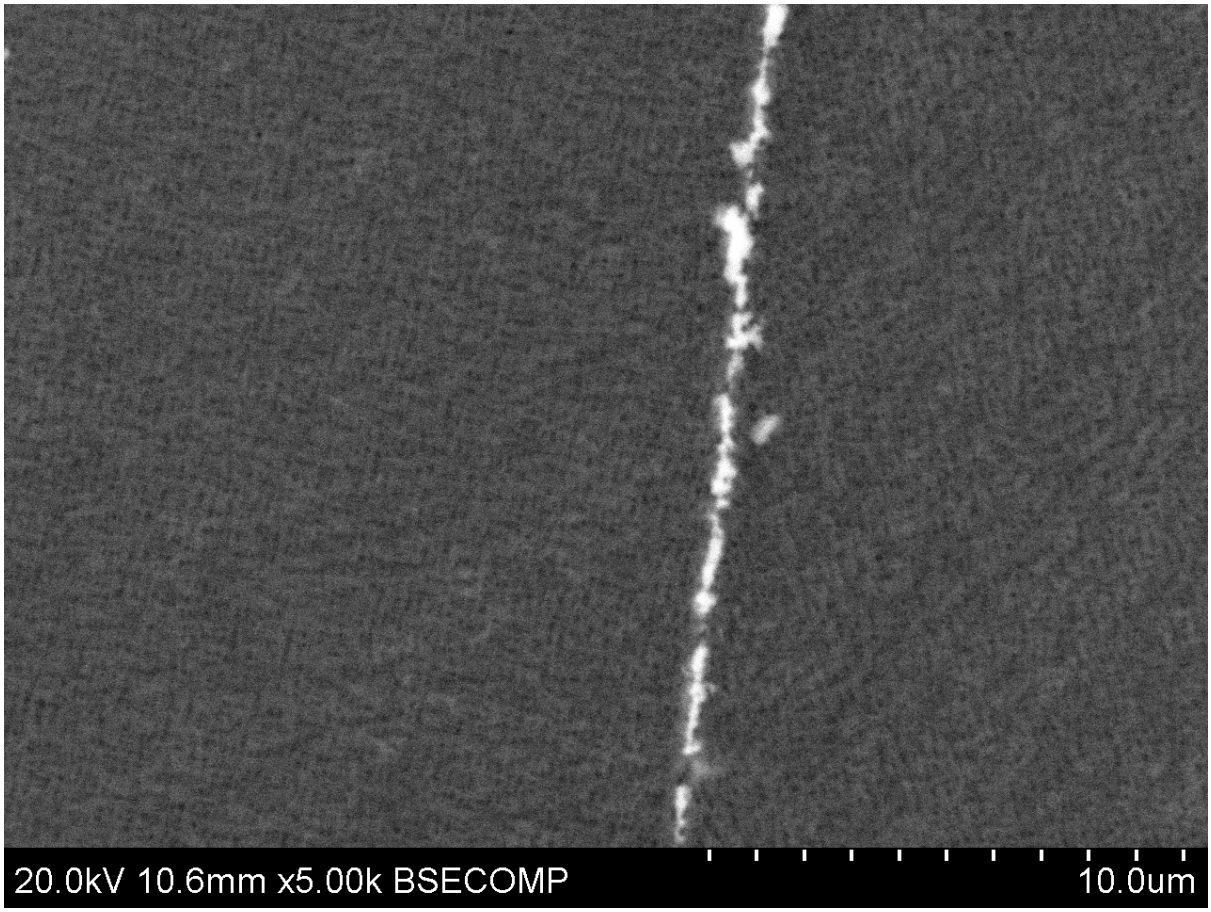

Figure 21. A scanning-electron microscopy (SEM) image of the FBB8 + 0.5% Hf - 1.5% Ti alloy (taken at 5,000 times magnification) displaying a distinct precipitate population with a <r> = ~ 94 nm and a discontinuous dispersion of a high z-contrast phase at the grain boundary.

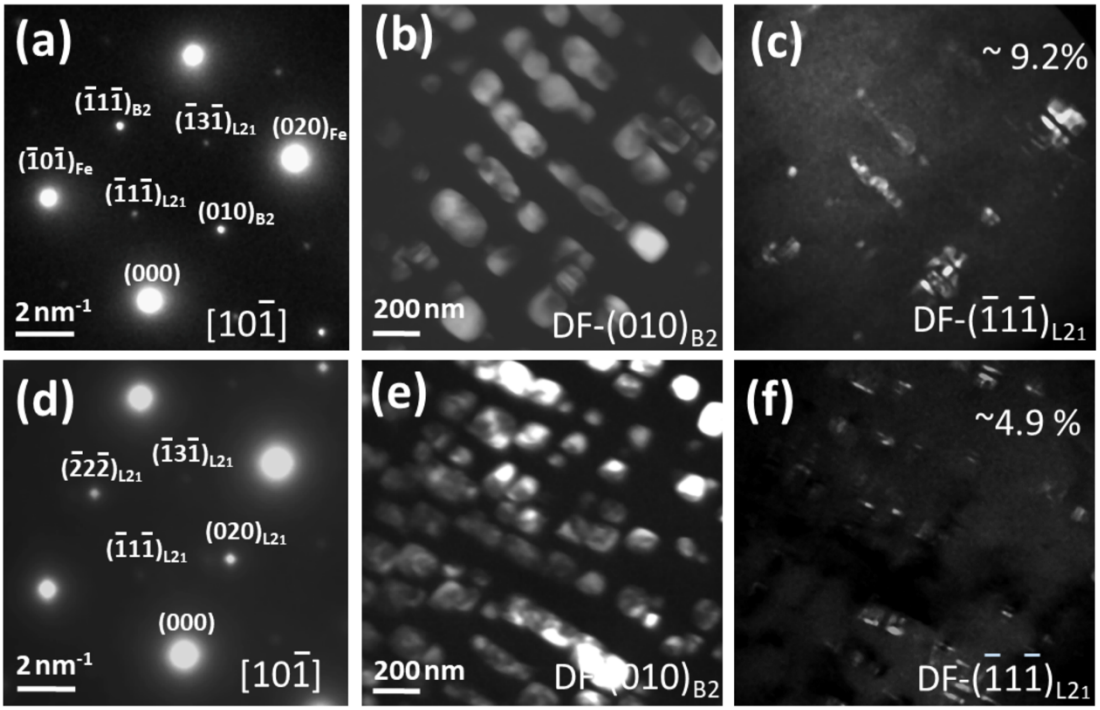

Figure 22. The selected-area-diffraction pattern (SADP) and dark-field (DF) transmission electron microscopy (TEM) images of FBB8 + 1.5% Ti - 0.5% Hf alloys in the aged at 700 ^{o}C for 100 hrs. (a, b, c) SADP and DF images of (010)B2, (-10-1)$L2_1$ superlattice reflection of FBB8 + 1.5% Ti, (d,e,f) SADP and DF images of the (010)B2, (-10-1)$L2_1$ superlattice reflection of FBB8 + 1.5% Ti - 0.5 wt.% Hf.

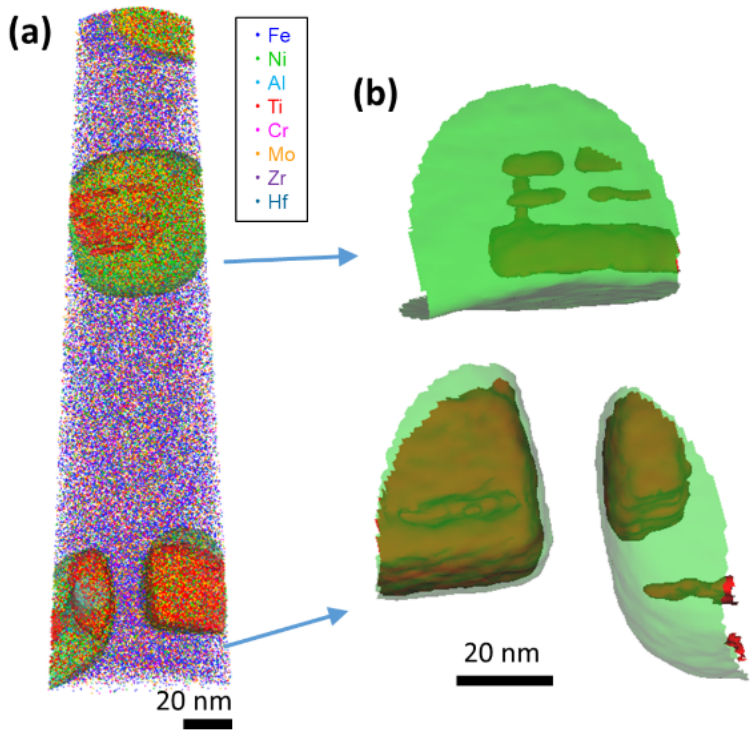

Figure 23. Atom-probe tomography (APT) analysis of the hierarchical structure of precipitates in the FBB8 + 1.5% Ti - 0.5% Hf alloy with the mixed B2 + $L2_1$ phases. (a) 3D reconstruction of the volume showing Al, Ni, Fe, Cr, Mo, Zr, Ti, and Hf, and two iso-(concentration) surfaces of 20 at.% Ni (green color) and 10 at.% Ti (red color), and (b) 3D reconstruction of hierarchical precipitates with transparent Ni and Ti iso-surfaces.

Table 8. The elemental concentration (at. %) within the precipitates (ppt) and the matrix

	Al	Ti	Cr	Fe	Ni	Zr	Mo	Hf
Ppt	21.0 ± 0.07	1.8 ± 0.01	1.3 ± 0.03	17.9 ± 0.14	57.2 ± 0.23	0.2 ± 0.04	0.3 ± 0.08	0.3 ± 0.11
Matrix	5.2 ± 0.45	1.3 ± 0.05	12.4 ± 0.13	75.3 ± 0.76	3.3 ± 0.14	0.1 ± 0.05	2.2 ± 0.03	-

5.5 Results for FBB8 + Ti series alloys

The creep resistance varies with small changes in the amount of Ti added by increase of coherency strains with forming sub $L2_1$-ordered Ni_2TiAl in the B2 ordered-NiAl precipitate that impedes dislocation motion effectively. Here, the effect of the $L2_1$ volume fraction in the precipitate by the Ti addition on the creep property in the ferritic alloy is studied. The volume fraction of $L2_1$ phase is 12.1 ± 3.1 at. % in the hierarchical-Ni_2TiAl/NiAl precipitate in the FBB8 + 1.5% Ti alloy, and it increases drastically to 90.9 ± 1.9 at. % in the FBB8 + 3.5%Ti alloy and 100 at. % in the FBB8 + 4%Ti sample. This is measured precisely by examining dark-field (DF) TEM images. The creep resistance is increased by the addition of titanium in a range of 1.5 to 3.5% Ti, and decrease sharply when between 3.5 and 4% Ti is added. This trend demonstrates the strong effect that the volume fraction of the $L2_1$-Ni_2TiAl phase in the hierarchical microstructure of the precipitate has on the creep strength by increase of coherency strains. Although the presence of titanium has an overall positive effect on creep properties, the presence of misfit dislocation after 2.0% Ti reduces the increase of misfits in the range 2.0 to 3.5% Ti additions. The creep resistance is sensitively changed by the ratio of B2 or $L2_1$ precipitates, the lattice misfit, and coarsening processes [77]. Therefore, understanding the alloying elements effect on the volume fraction change of sub-precipitate within the main precipitates will help with a further design of these steels to achieve higher strength and creep resistance for high temperature applications.

The precipitate microstructure was investigated using dark-field (DF) transmission electron microscopy (TEM) images with selected area diffraction patterns (SADPs), Figure 24. DF images are taken in the near [10-1] zone axis orientation with $(111)_{B2}$ reflection for the B2-ordered NiAl and $(111)_{L21}$ reflection for $L2_1$-ordered Ni_2TiAl phase of the FBB8 + (1.5 - 4.0 Ti) alloys. The SADPs in Figures 24(a), and (e) clearly reveal the super-lattice reflections of both B2-

and $L2_1$-ordered phases (020 and 222) and unique $L2_1$-ordered Ni_2TiAl (111 and 131). Three structures, BCC, B2 and $L2_1$, have cube on cube orientation relationships (ORs) maintaining the coherent interface. Replacing half of the Al atoms with Ti in the B2-ordered NiAl phase results in the $L2_1$-ordered Ni_2TiAl, the unit-cell of $L2_1$-phase, therefore, doubles the unit-cell of B2-NiAl. The hierarchical structure of precipitates are display in the color mixed DF images of $(111)_{L21}$ and $(111)_{B2}$ super-lattices in the FBB8 + (1.5 - 4.0 wt.% Ti) alloys, Figures 24(b) to (g). Two super-lattices, $(111)_{L21}$ and $(111)_{B2}$, are indicated by the red and green circles in SADP image, respectively. The precipitate in the FBB8 + 1.5% Ti alloy shows a cuboidal shape with a width ranging from 50 to 100 nm and spatial arrangement along the <001> direction. These cuboidal shape and cubical array of precipitate suggests a strong effect of coherency stresses on the interface between two interfaces, BCC/B2 and $L2_1$-B2 phases [78]. The precipitate shape changed from cuboidal to spherical by losing coherency between BCC/precipitate interface with the further Ti addition. The $L2_1$-Ni_2TiAl precipitates are incorporated with misfit dislocations around the primary precipitates, suggesting a semi-coherent interface between the Fe matrix and the hierarchical B2/$L2_1$ precipitates. Regions with a red colored image indicates the location of $L2_1$ sub-precipitates that are mixed with the green colored B2-ordered precipitates. The DF images of the FBB8-(1.5 to 3.5% Ti) alloy, Figures 24 (b) to (f), show similar feature of hierarchical structure of $L2_1$/B2 structure with different volume fractions. The volume fraction of the $L2_1$ phase in the precipitate (B2 + $L2_1$) are confirmed by the comparison of DF image of $L2_1$ phase and B2 phase in TEM analysis. The volume fraction of the $L2_1$ phase is 12.1 ± 3.1 at. % in the FBB8 + 1.5% Ti sample, and it increases drastically to 90.9 ± 1.9 at. % in the FBB8 + 3.5% Ti sample and 100 at. % in the FBB8 + 4% Ti sample. The volume fraction of the $L2_1$ phase with Ti concentration is represented in Figure 25.

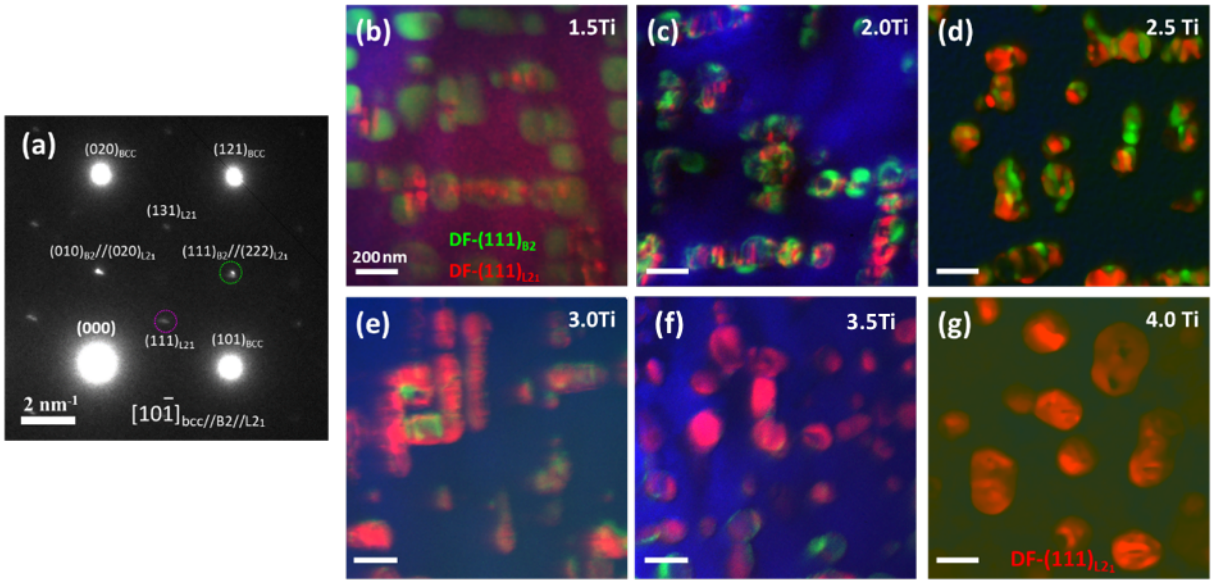

Figure 24. The selected area diffraction pattern (SADP) and dark-field (DF) transmission electron microscopy (TEM) images of FBB8 - (1.5 - 4.0 wt.%Ti) alloys in the aged at 700 ^{o}C for 100 hrs. SADPs are obtained in the [10-1] zone axis condition with containing three phases; BCC (Fe), B2 and $L2_1$. (b-f) color mix of dark-field (DF) images of B2 (green) and $L2_1$ (red) phases to show the volume fraction change in the precipitate.

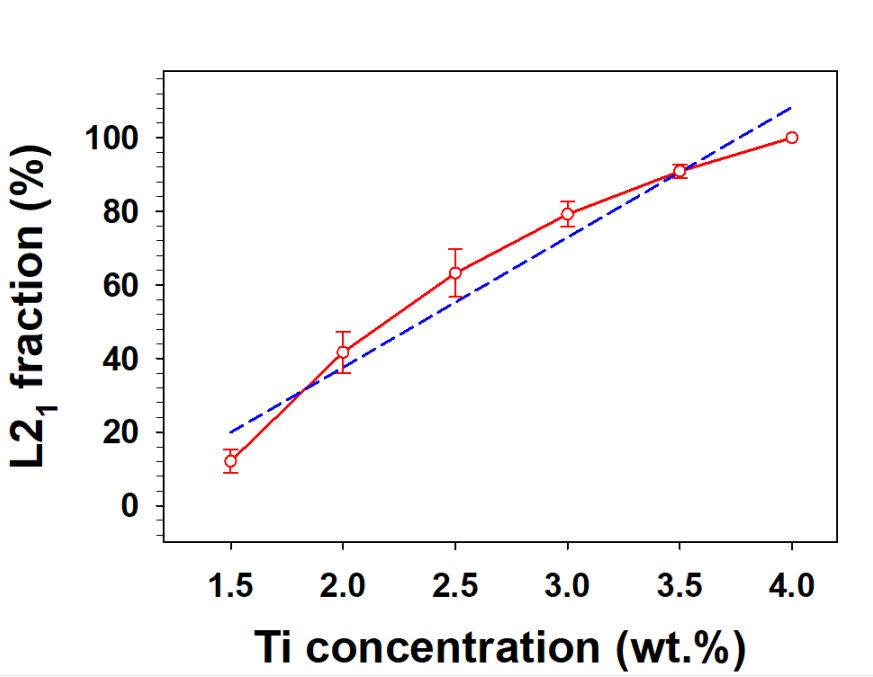

Figure 25. Volume fraction of $L2_1$ phase in precipitate as a function of Ti concentration (1.5 - 4.0 wt.% Ti). The red empty circle indicates the measured value of the $L2_1$ phase in the precipitate and blue dot line is a linear fit of experimental values.

5.6 Conclusion

From the microstructural characterization, we've found that (1) FBB8 + 2% Hf and FBB8 + 2% Zr alloys do not have $L2_1$ phase formed parent with the existing B2 phase. Instead, Hf and Zr added into the FBB8 system form the Laves phase with Fe and segregated along the grain boundaries and within grains. (2) The dark-field (DF) TEM images in alloys with Ti higher than 1.5 wt.% reveal the hierarchical, cuboidal (50 - 100 nm in size), coherent B2-sub $L2_1$ precipitate, with an interfacial alignment towards a cube-on-cube orientation, (3) the 3D APT analysis on the alloys shows the detailed compositional changes in the B2/$L2_1$ hierarchical microstructure of the precipitates. Fe, Cr, and Mo are strongly partitioned to the matrix phase, whereas Ni, Al, Ti, and Zr are mainly concentrated into the B2 and $L2_1$ (sub)-precipitates. Between the B2 and L21 precipitates, Ti, Fe, Mo, Cr, and Zr are enriched in the $L2_1$ subprecipitates (and consequently Ni and Al are depleted). Hf is also strongly partitioned to both phases in the precipitate, and may destabilize the $L2_1$ phase due to the large size of the Hf atom and decrease the volume fraction of the $L2_1$ phase in the precipitate.

6. Lattice Constants and Precipitate Volume Fraction Measurements

The lattice constant and volume fraction of the precipitation are critical factors for the evaluation of mechanical properties for precipitation strengthening alloys. The lattice constant difference (a.k.a. lattice mismatch) between the matrix and precipitates is the major source of strengthening, and the volume fraction of the precipitation is also important. The precipitates within the alloy should have high enough volume fraction, appropriate precipitation size, and homogeneously dispersed within the alloy. In this chapter the major tasks are the measurements of the lattice constants for each phases within the model alloy systems, and the volume fraction of the precipitates.

6.1 Introduction

Conventionally, the precipitate volume fraction can be measured by taking SEM images, and measure the diameter on each precipitate for a statistically sufficient amount of numbers. However, from the analysis of the diffraction patterns, both the lattice constants and volume fraction of each phase can be easily extracted by utilizing the General Structure Analysis System (GSAS) with the Rietveld refinement method [81]. The diffraction pattern for a specific phase possesses peaks in specific angles, which tells us the lattice constant of that phase. Also different phases, based on their respective crystal structure, have different numbers of peaks within the diffraction pattern. From the information, combined with preliminary results from the microstructural investigations, the lattice constant and the volume fraction for each phase can be easily identified from the fitting approach performed within the GSAS software [82]. The following paragraphs are going to discuss the measurements on the model alloys.

6.2 FBB8 + 2% Hf alloy and FBB8 + 2% Zr alloy

From the preliminary investigations and calculations on the microstructures of FBB8 + 2 wt.% Hf and FBB8 + 2 wt.% Zr alloys, we briefly concluded that the major phases presented within these alloys should be α-Fe as the matrix and B2-NiAl as the major precipitates (strengtheners). There should be also a hexagonal Laves phase (C14) according to the CALPHAD calculation in Figure 7, but probably with low volume fractions that as a result, cannot be easily identified in the diffraction pattern. Since the mechanical properties are majorly affected by B2 and/or $L2_1$ phases, our focus on the diffraction pattern will be majorly the peaks of those phases.

The in-situ neutron experiment is conducted as a compressive creep test at 700 ^{o}C and different stress levels (80, 90, and 100 MPa) at the Spallation Neutron Source (SNS) in the Oak Ridge National Laboratory (ORNL). The samples of FBB8 + 2% Hf and FBB8 + 2 wt.% Zr alloys are fabricated as a cylinder, with the length and diameter ratio of 2:1. After fabrication, the samples were homogenized at 1,200 ^{o}C for 30 minutes, and then aged at 700 ^{o}C for 100 hours. During the compressive creep tests, the incident neutron beam constantly hit the sample and diffracted, collected by two detectors, which are able to collect the axial and radial responses of the sample under stress. Figure 26 shows a schematic figure for the setup of the in-situ neutron experiment. During the experiment, the compression sample will be heated up and dwelled at 700 ^{o}C, and applied with constant loading depends on the stress level. In this chapter, we are using the ND pattern from the bank-2 detector. However, it has no differences between the data collected from the bank-1 and bank-2 detectors without applying any stress. The collected data is later analyzed by the General Structure Analysis System (GSAS) with the Rietveld refinement method.

Figure 27 shows the ND pattern of the FBB8 + 2% Hf alloy at room temperature. The major phases that can be identified from the whole peak fitting are the BCC phase (α-Fe) and B2 phase (B2-NiAl). Major peaks with high intensities are actually an overlap of BCC and B2 peaks, because of the almost identical lattice constants. In the diffraction pattern, we can see that the peaks that are unique for the B2 phase are having low intensities due to low volume fractions, and become hardly recognizable in the high d-spacing area. Figure 28 shows the ND pattern of the FBB8 + 2 wt.% Zr alloy at room temperature, and it looks similar to the ND pattern of the FBB8 + 2 wt.% Hf alloy, which suggests that although there are different chemical compositions for these two alloys, the phases that they formed are the same. This phenomenon can also be proved by the scanning-electron-microscopy (SEM) images reported in chapter 5.

Figure 29 presents the ND pattern of the FBB8 + 2% Hf alloy at 700 ^{o}C, and Figure 30 presents the ND pattern of the FBB8 + 2% Zr alloy at 700 ^{o}C. Due to the thermal expansion, every peak at 700 ^{o}C for the ND patterns shifts to higher d-spacings than at room temperature. By comparing the phases at 700 ^{o}C and room temperature, there are no significant differences, which suggests that the change in temperature from room temperature to 700 ^{o}C does not cause a formation or annihilation of original existing phases. The CALPHAD calculation for the FBB8 + 2% Zr alloy in Chapter 5 suggests that there will be about 40% of the FCC phase formed at 700 ^{o}C. However, in the diffraction pattern, it does not show evidence for the formation of the FCC

phase. One thing needs to be noted is that there are actually many small peaks that cannot be easily identified from whole peak fitting. The hexagonal Laves phase (C14) has been tried in the fitting but the peak position does not match, neither do the $L2_1$ phase. This result might suggest that either (1) there are no hexagonal Laves phase (C14) and $L2_1$ phase, or (2) the volume fractions of the hexagonal Laves phase (C14) and $L2_1$ phase are too low. According to the CALPHAD calculation, the volume fraction of the hexagonal Laves phase (C14) is lower than 10%, which might be the reason that there's no clear peaks to show the existence of the hexagonal Laves phase (C14).

Some structural information for the FBB8 + 2% Hf and FBB8 + 2% Zr alloys is summarized in Table 9. The lattice constants for the BCC and B2 phases are almost the same, leading to a very small amount of lattice mismatch (< 0.2% at either room temperature or 700 ^{o}C), which suggests that the matrix/precipitate interface is a coherent interface. For the volume fraction of the precipitates (B2 phase), at room temperature, there is ~ 21 vol.% of the precipitates within FBB8 + 2% Hf alloy, and ~ 15 vol.% within the FBB8 + 2% Zr alloy. At 700 ^{o}C, the volume fractions of the precipitates (B2 phase) for both FBB8 + 2 wt.% Hf and FBB8 + 2% Zr alloys dropped. For the FBB8 + 2 wt.% Hf alloy, it becomes ~ 17.5 vol.%, and for the FBB8 + 2% Zr alloy, it becomes ~ 14 vol.% at 700 ^{o}C. The decrease of the volume fraction of the materials can be predicted from the CALPHAD calculation, after about 650 ^{o}C, there will be a decrease of the B2 phase. For the FBB8 + 2% Hf alloy, it seems to have a relatively-higher volume fraction of precipitates, compared with the FBB8 + 2% Zr alloy, which leads to either (1) more precipitates assuming with the same precipitation size, or (2) larger precipitation size assuming the same number of precipitation particles, resulting in better mechanical properties.

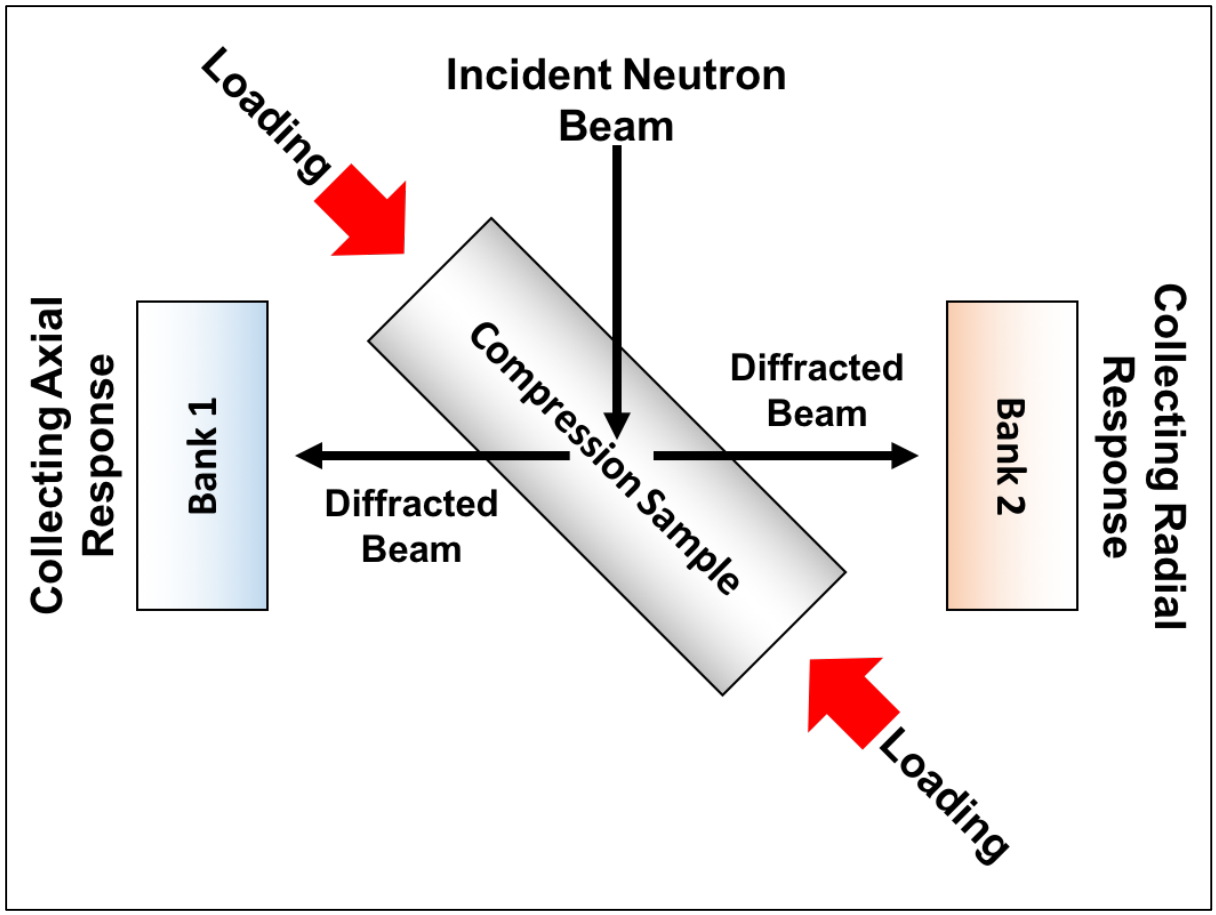

Figure 26. A schematic of the setup for the in-situ neutron experiment. Banks 1 and 2 detectors can constantly collect axial and radial responses of the sample during the applying stress.

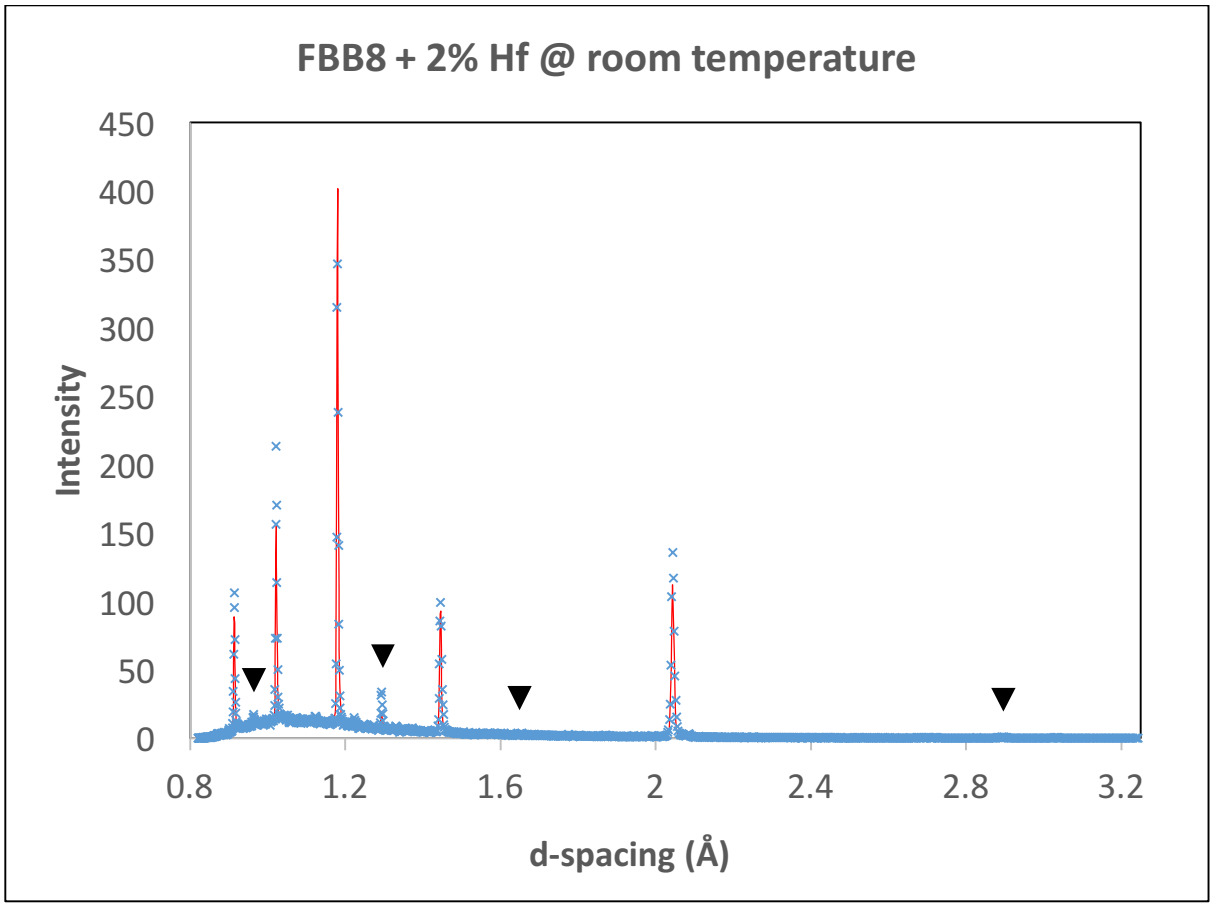

Figure 27. The ND pattern for the FBB8 + 2% Hf alloy at room temperature. Major peaks with high intensities are the combination of peaks of the α-Fe and B2 phases. Black arrows indicate the peaks of the B2 phase. Due to the low volume fraction, the intensities for peaks of the B2 phase at the high d-spacing become extremely low.

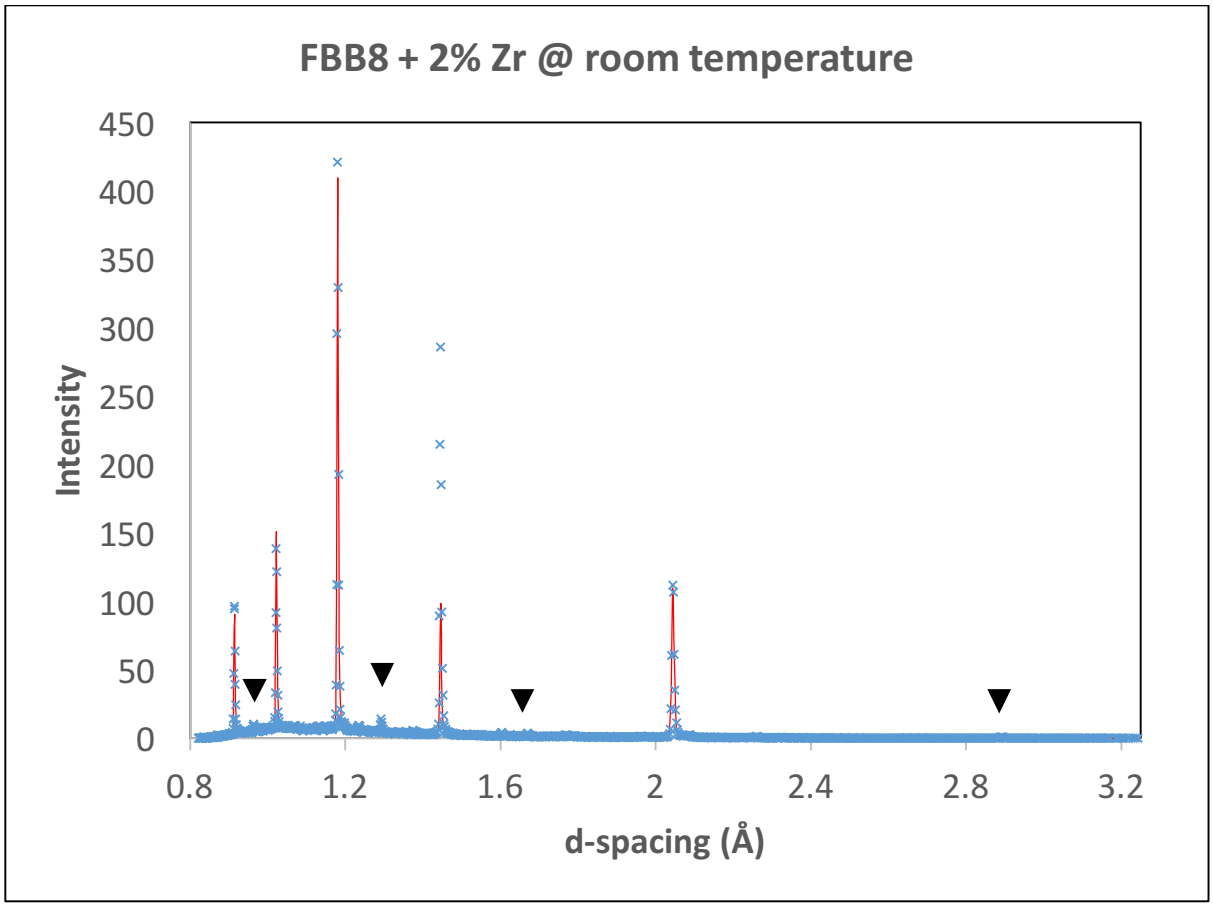

Figure 28. The ND pattern for the FBB8 + 2% Zr alloy at room temperature. The whole pattern looks much similar to the ND pattern for the FBB8 + 2% Hf alloy, which suggests the similarity of the phases within these two different compositions.

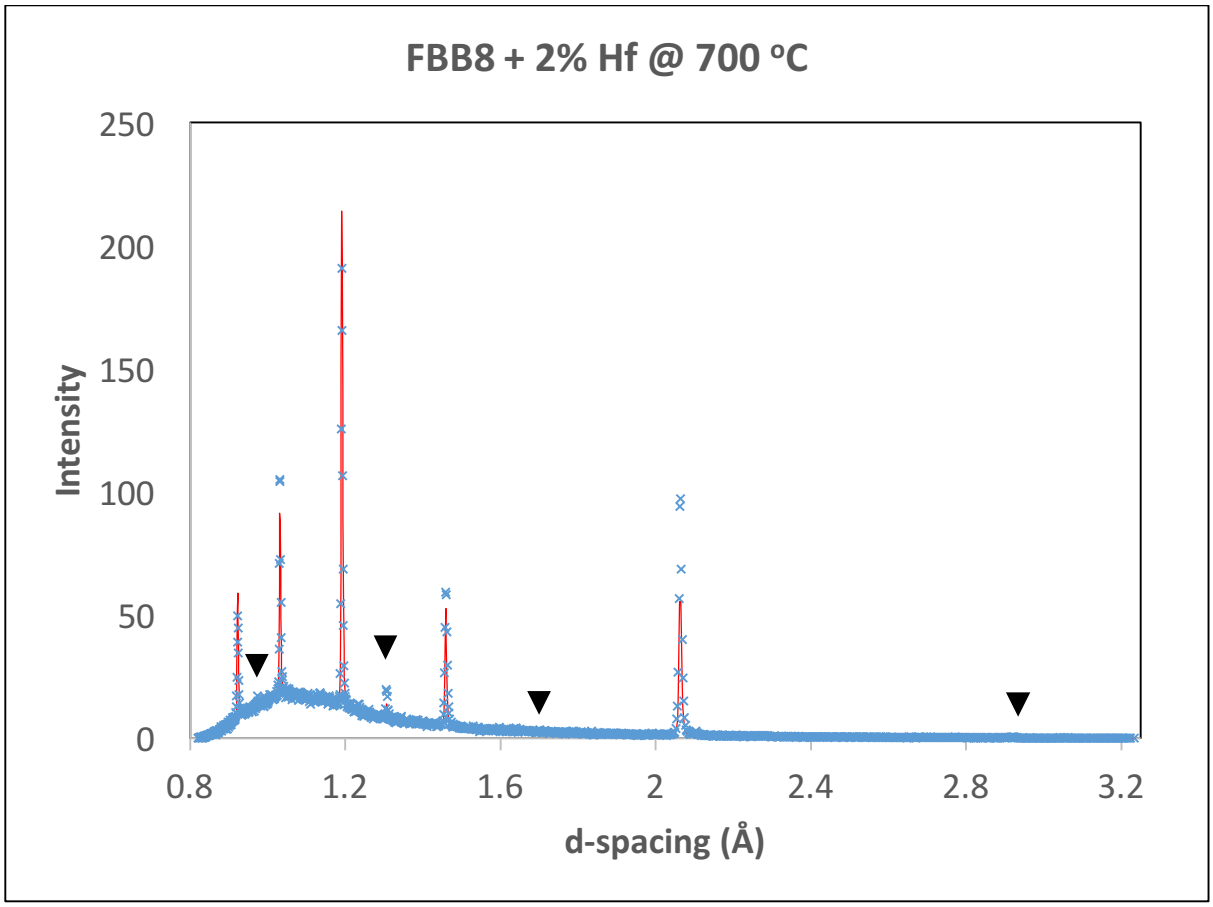

Figure 29. The ND pattern for the FBB8 + 2% Hf alloy at 700 °C. Peaks are shifted to the right because of the thermal expansion. As shown in the figure, there's no major changes in phases from room temperature to 700 °C. α-Fe and B2 phases are still the most obvious phases that can be identified from whole peak fitting, which suggest that they are still the majority of the microstructure of the FBB8 + 2% Hf alloy.

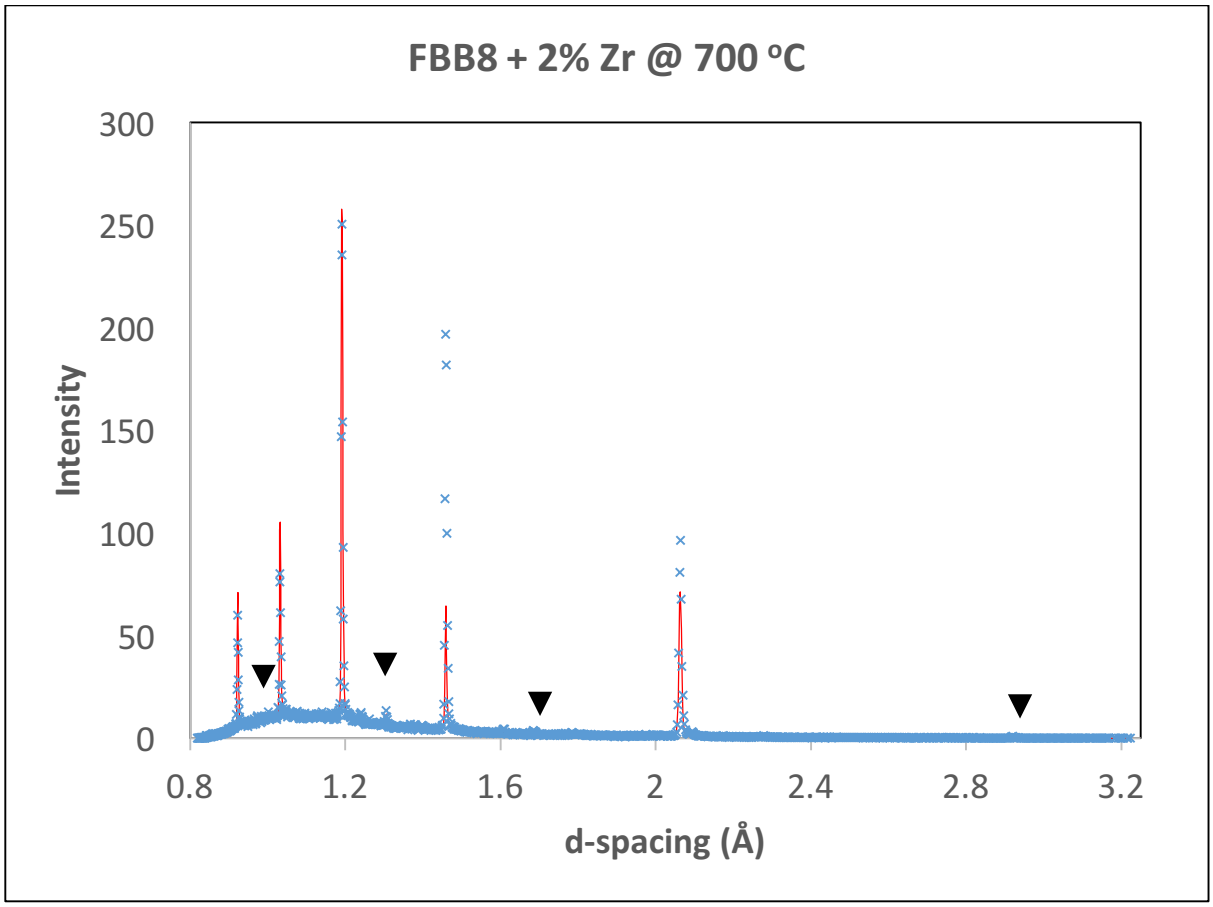

Figure 30. The ND pattern for the FBB8 + 2% Zr alloy at 700 °C. Same as the FBB8 + 2% Hf alloy, α-Fe and B2 phases are still the most obvious phases that can be identified from whole peak fitting. Therefore, there's no major change in phases from room temperature to 700 °C.

Table 9. The structural information for the phases presented within FBB8 + 2% Hf and FBB8 + 2% Zr alloys at room temperature and 700 °C.

Material		Room Temperature		700 °C	
	Phases	Lattice Constant (Å)	Volume Fraction	Lattice Constant (Å)	Volume Fraction
FBB8 + 2% Hf	BCC	2.887898	0.786903616	2.915356	0.824291925
	B2 Phase	2.890448	0.213096384	2.921048	0.175708075
FBB8 + 2% Zr	BCC	2.889297	0.850251825	2.915942	0.85938138
	B2 Phase	2.889125	0.149748175	2.918233	0.14061862

6.3 FBB8 + 4% Ti alloy

The results presented here summarize the analysis of the microstructural characterization of the single-Ni_2TiAl-strengthened ferritic alloy 4 wt. % Ti-containing alloy at room and elevated temperatures, using ND techniques. The in-situ ND experiments were carried out on the Spectrometer for MAterials Research at Temperature and Stress (SMARTS) diffractometer of the Los Alamos Neutron Science Center (LANSCE) facility located at the Los Alamos National Laboratory [45]. The ND instrument utilizes time-of-flight (TOF) measurements, in which the incident beam is polychromatic with a range of wave lengths, which allows for the ND measurements with a diffraction pattern covering a wide range of d-spacings without the rotation of samples or detectors. The ND measurements were conducted at room temperature, 572 ˚C, and 700 ˚C. The samples were measured by ND at elevated temperatures after the sample saturated within ± 1 ˚C of the target temperature. The ND data were collected for 15 minutes.

In order to obtain the thermal lattice strain during heating, a whole-pattern Rietveld refinement was performed to fit the entire ND spectrum, employing the General Structure Analysis System (GSAS) program developed at the Los Alamos National Laboratory [46]. The average phase strain is calculated, using the following formula

$$\varepsilon = (a - a_0)/a_0 \tag{9}$$

where a is the lattice parameter of a given phase measured during heating, and a_0 is the corresponding lattice parameter at room temperature. In addition, single-peak fitting of the $(110)_{Fe}$ and $(220)_{L21}$ peaks employing the RAWPLOT utility of the GSAS code was conducted to obtain the intensity ratio of the $L2_1$ to Fe phases [46].

The Rietveld-refinement technique was used to obtain the average lattice parameters of the Fe and $L2_1$-type phases using the GSAS code developed by Larson and Von Dreele [46, 47] at the Los Alamos Neutron Science Center (LANSCE). The average lattice parameters of the Fe matrix and $L2_1$-type precipitate at room temperature are 2.8864 and 5.8537 Å, respectively, and gradually increase with temperature, as shown in Figure 31(a). The lattice mismatch between the lattice parameters of the Fe and $L2_1$ phases is calculated, using following equation;

$$\delta = \frac{2(a_{L2_1} - 2a_{Fe})}{(a_{L2_1} + 2a_{Fe})} \tag{10}$$

where δ is the lattice misfit, and a_{Fe} and a_{L2_1} are the lattice parameters of the Fe and $L2_1$ phases, respectively. Since the $L2_1$ structure consists of the eight sub-lattices of a B2 structure [48], the lattice parameter of the Fe was multiplied by a factor of two for the corresponding structural comparison. The average lattice parameters of the Fe and $L2_1$ phases, and corresponding lattice misfits at room and elevated temperatures are summarized in Table 10. The lattice misfit at room temperature is 1.39 %, and no clear temperature dependence of the lattice misfit is observed. The thermal strains of both phases were estimated, using Equation (9), Figure 31(b) shows the thermal strains of the Fe and $L2_1$ phases as a function of temperature. Thermal strains determined using neutron diffraction (ND) have been employed to obtain coefficients of thermal expansion (CTEs) of constitutive phases in composite materials [49, 50]. Similarly, the average CTEs were determined from the slopes of linear fits to the data in Figure 31(b) and found to be 1.34×10^{-5} /°C and 1.42×10^{-5} /°C for the Fe and Ni_2TiAl phases, respectively. The reported CTE of the α Fe is 1.2×10^{-5} /°C [51], which is in agreement with the CTE of the Fe matrix in the current alloy. However, there is no available experimental value of the CTE of the Ni_2TiAl with a high amount of Fe elements. An experimental CTE of a Fe_2TiAl alloy with the $L2_1$ structure has been determined by ND [52], and was found to be 1.45×10^{-5} /°C, which is close to that of the Ni_2TiAl phase in the current alloy.

A direct separation of the fundamental peaks can be made, using the GSAS single-peak fitting (SPF), due to the reasonable intensity of the $L2_1$ phase and well-separated fundamental reflections. In this study, fundamental reflections $(110)_{Fe}/(220)_{L21}$ were selected to determine the intensity ratio, as shown in Figure 32. The intensity ratio of $L2_1$ to Fe can be determined from the structure factor and volume fraction, using the following equations [53]:

$$\frac{I_{hkl}^{L21}}{I_{hkl}^{Fe}} = \frac{\left(F_{hkl}^{L21}\right)^2}{\left(F_{hkl}^{Fe}\right)^2} \frac{v_f}{(1-v_f)} \tag{11}$$

$$F_{hkl}^{Fe} = b_{c0} e^{2\pi i(0h+0k+0l)} + b_{ce} e^{2\pi i(0.5h+0.5k+0.5l)} \tag{12}$$

$$F_{hkl}^{L21} = b_{c0} e^{2\pi i(0h+0k+0l)} + b_{ce} e^{2\pi i(0.5h+0.5k+0.5l)} + b_{h.ce} e^{2\pi i(0.25h+0.25k+0.25l)} \tag{13}$$

where I_{hkl}^{L21} and I_{hkl}^{Fe} are the intensities of the (hkl) peaks in the $L2_1$ and Fe phases, respectively, F_{hkl}^{L21} and F_{hkl}^{Fe} are the structure factors of the (hkl) peaks in the $L2_1$ and Fe phases, respectively, b_{co}, b_{ce}, and $b_{h.ce}$ are the scattering lengths of the corner, center, and half center atoms, respectively, and V_f is the volume fraction of the $L2_1$-type precipitate. The values of scattering lengths are functions of the actual compositions of phases, expressed by:

$$b_{co,ce}^{Fe} = \sum c_{i,co,ce}^{Fe} b_i \tag{14}$$

$$b_{co,ce,h.ce}^{L21} = \sum c_{i,co,ce,h.ce}^{L21} b_i \tag{15}$$

where $c_{i,co,ce}^{Fe}$ and $c_{i,co,ce,h.ce}^{l21}$ are the atomic concentrations of the element, i, in the Fe and $L2_1$ phases, respectively, b_i is the scattering length of neutrons by the atom of the element, i, which can be obtained from the literature [54]. The transmission-electron-microscopy (TEM) energy-dispersive X-ray (EDX) analysis revealed a considerable amount of Fe dissolved in the $L2_1$-type precipitate, which alters the structure factor, and, thus, intensity. Table 11 shows the EDX compositions of the Fe and $L2_1$-type phases.

Assuming that the 15 atomic percent (at. %) and the rest of Fe in the $L2_1$-type precipitate occupies on the Ni and Ti sublattice sites, respectively, the structure factors and volume fractions have been calculated for four $(Ni_{35}Fe_{15})(Al_{25})(Ti_{25-x}Fe_x)$ (at. %) compounds with x = 0 ~ 7.5. The compositions, corresponding ratios of structure factors, and volume fraction of the $L2_1$ phase are summarized in Table 12.

The volume fraction (22.2 %) of the $L2_1$ phase determined from the SEM-image analysis is in better agreement with the value of 22.7 % calculated, based on an approximate composition of $(Ni_{35}Fe_{15})(Al_{25})(Ti_{20}Fe_5)$ (at. %) in Table 12, which supports that the $L2_1$-Ni_2TiAl phase is enriched in Fe. Assuming that the compositions of the Fe and $L2_1$ phases do not vary at higher temperatures, the volume fractions are calculated at 572 ˚C and 700 ˚C, which are given in Table 4. The calculated volume fraction at 572 ˚C remains fairly the same as that at room temperature, but increases to 23.2 % at 700 ˚C. In general, it is known that as the temperature increases, the volume fraction of precipitates decreases. Thus, the volume increase is unlikely to happen at 700 ˚C. This trend reflects that the compositions of the matrix and $L2_1$ phase could vary at 700 ˚C. The intensity ratio of $L2_1$ to Fe (I_{L21}/I_{Fe}) in Table 13 remains constant (0.178) at room temperature and 572 ˚C. However, the intensity ratio increases to 0.184 at 700 ˚C. With a decrease in the volume

fraction at high temperatures, it would be expected that the intensity ratio decreases accordingly. However, structure factors can also contribute to the intensity magnitude (Equation 3), which depends on the composition of the constitutive phases. First, more elements from the precipitate, such as Al, Ni, and Ti, could be dissolved into the matrix, which results in a reduction of the intensity of the Fe matrix. This trend results from the fact that Fe has higher solubility of Al, Ni, and Ti at high temperatures than at low temperatures [55], and these solute elements have all smaller scattering lengths than Fe [54]. Second, since the TEM and neutron analyses reveal that the $L2_1$-type phase contains a high amount of Fe, it can be inferred that a greater amount of Fe could be dissolved into the $L2_1$ precipitate at 700 ˚C, which results in an increase in the intensity of the $L2_1$ phase.

The difference in the CTEs between constitutive phases contributes to the temperature dependence of the lattice misfit 56. The linear CTE of the $L2_1$ phase is slightly higher than that of the Fe matrix [Figure 31(b)], and, thus, the slight increase of the misfit at 572 ˚C is observed (Table 10). However, the misfit at 700 ˚C is smaller than that at 572 ˚C (Table 10). Another feasible influence on the temperature dependence of the misfit is the compositional variation of the two phases. As the temperature increases, the compositional variation starts to occur, as mentioned above. This compositional variation leads to a reduction and increase of the lattice parameters of the $L2_1$ and Fe phases, respectively, due to the smaller atomic size of Fe than Al and Ti [57], and, thus, resulting in the decrease of the lattice misfit at 700 ˚C, as compared to 572 ˚C. As observed in the change of the intensity ratio (I_{L21}/I_{Fe}) (Table 13), this compositional variation appears to become significant at temperatures near 700 ˚C.

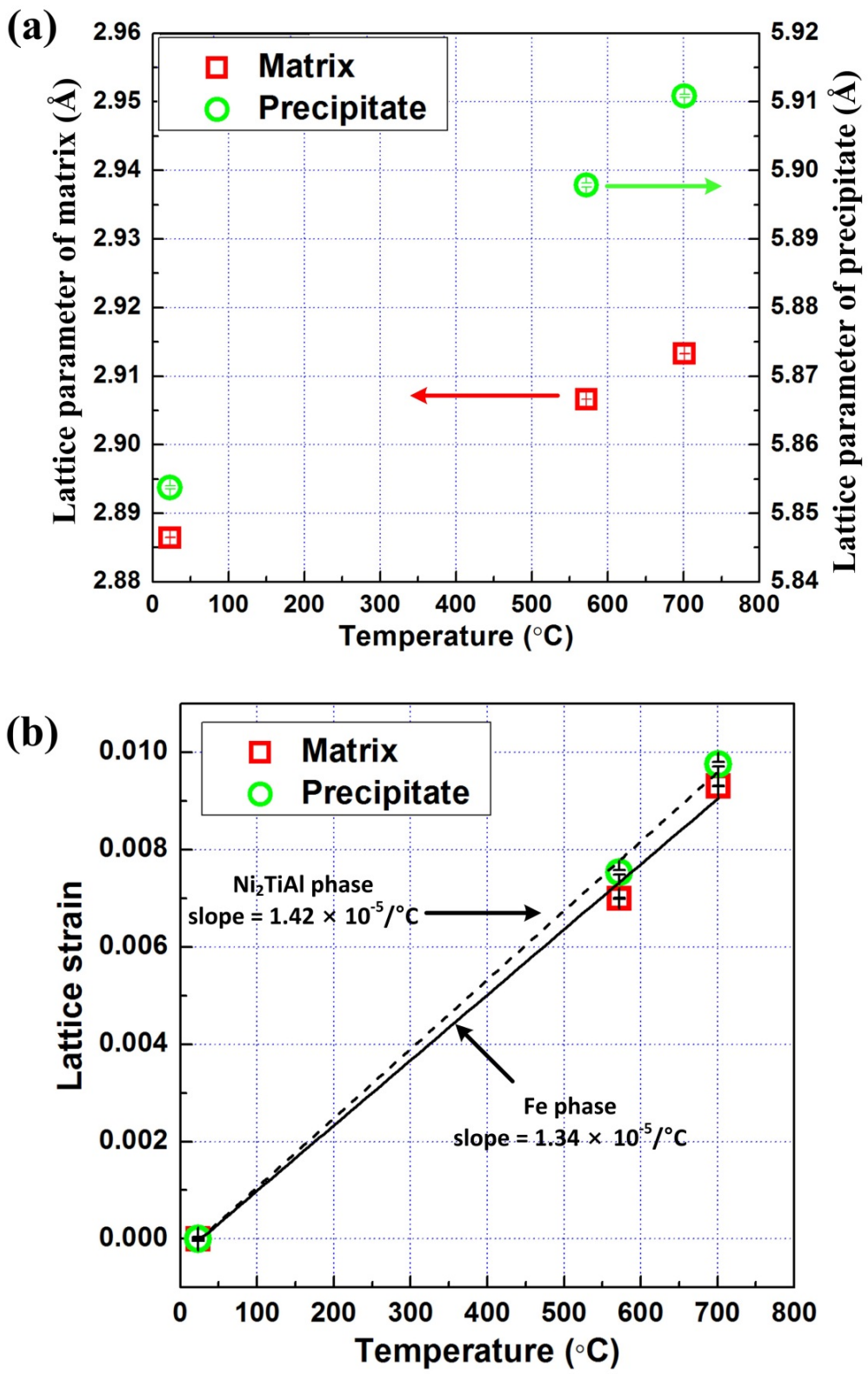

Figure 31. Plots of (a) lattice parameters and (b) thermal lattice strains of the Fe matrix and Ni_2TiAl precipitate as a function of temperature.

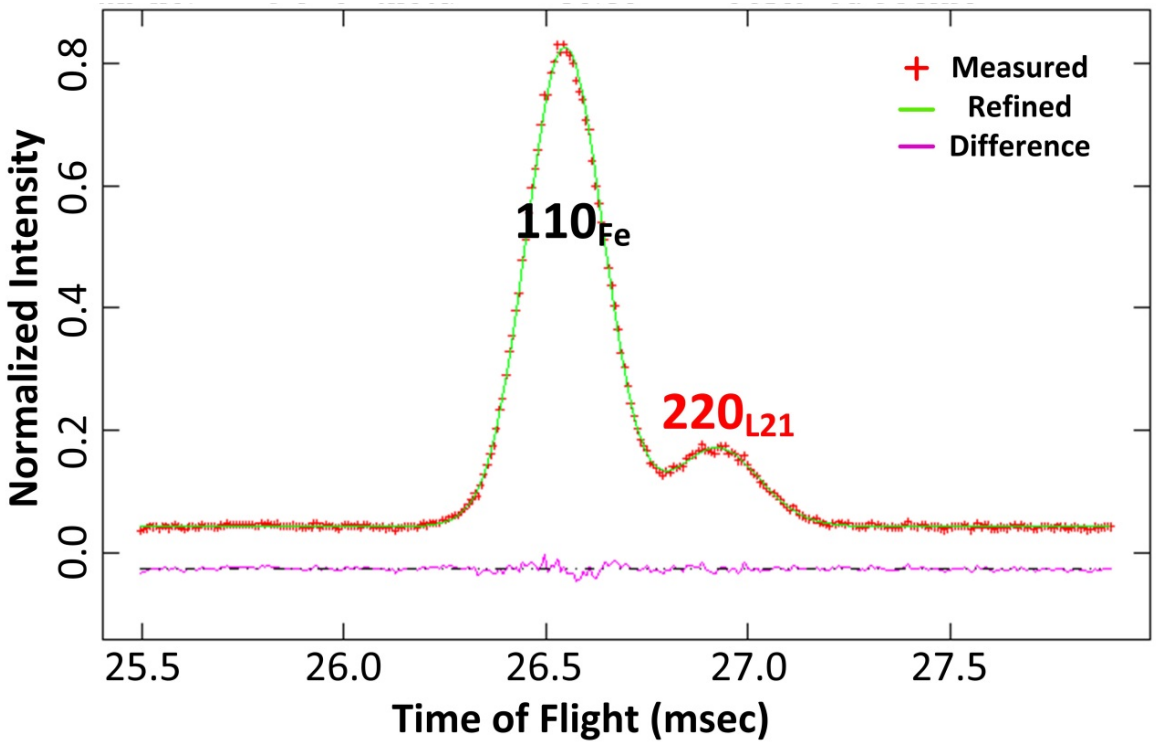

Figure 32. Single-peak-itting (SPF) result on a partially-overlapped $(110)_{Fe}/(220)_{L21}$ peaks at room temperature. The red cross represents the measured data. The green curve is the fitted profile, using GSAS. The pink curve presents the difference between the fitted profile and measured data.

Table 10. Average lattice parameters of the Fe and $L2_1$ phases and corresponding misfits as a function of temperature.

Temperature (˚C)	Rietveld refinement		
	Fe (Å)	$L2_1$ (Å)	Misfit (%)
23	2.8864	5.8537	1.391
572	2.9066	5.8978	1.445
700	2.9132	5.9108	1.436

Table 11. Chemical compositions (in atomic percent) of the bulk sample, derived from the chemical analysis, and the constitutive phases in the Ni_2TiAl-strengthened ferritic alloy, obtained from the transmission-electron microscopy energy-dispersive X-ray (TEM-EDX) analysis. The uncertainties for the EDX results are represented by the standard deviation from the measurement series.

Phase	Fe	Cr	Al	Ni	Ti	Mo	Zr
Bulk	61.6	10.1	12.8	8.9	4.5	1.9	0.1
Fe	74.9 ± 0.5	12.8 ± 0.2	7.0 ± 0.4	2.1 ± 0.2	1.0 ± 0.1	2.0 ± 0.2	0.2 ± 0.1
$L2_1$	22.9 ± 3.7	1.0 ± 0.7	25.0 ± 2.0	33.8 ± 1.9	16.5 ± 0.9	0.1 ± 0.1	0.5 ± 0.3

Table 12. Ratios of the squares of the structure factor (F) and intensity (I) between different $L2_1$ compounds with varying Ti and Fe contents, and the resulting volume fraction (V_f) of the $L2_1$ phase.

Composition (at. %)	$(F_{L21})^2/(F_{Fe})^2$	I_{L21}/I_{Fe}	V_f (%)
	$(220)_{L21}/(110)_{Fe}$		
$(Ni_{35}Fe_{15})(Al_{25})(Ti_{17.5}Fe_{7.5})$	0.739	0.178	19.45
$(Ni_{35}Fe_{15})(Al_{25})(Ti_{20}Fe_{5})$	0.608	0.178	22.68
$(Ni_{35}Fe_{15})(Al_{25})(Ti_{22.5}Fe_{2.5})$	0.490	0.178	26.67
$(Ni_{35}Fe_{15})(Al_{25})(Ti_{25})$	0.385	0.178	31.64

Table 13. Intensity ratios of $(220)_{L21}/(110)_{Fe}$ as a function of temperature with a composition of $(Ni_{35}Fe_{15})(Al_{25})(Ti_{20}Fe_5)$ of the $L2_1$ phase, and the resulting volume fraction (V_f) of the $L2_1$ phase.

Phase	Room temperature		572 ˚C		700 ˚C	
	Neutron intensities	I_{L21}/I_{Fe}	Neutron intensities	I_{L21}/I_{Fe}	Neutron intensities	I_{L21}/I_{Fe}
$(220)_{L21}/(110)_{Fe}$						
Fe	188.2	0.178	128.0	0.179	151.7	0.184
$L2_1$	33.6		22.9		28.3	
V_f	22.7	-	22.7	-	23.2	-

6.4 Conclusion

The Lattice constants and volume fractions for each phase within FBB8 + 2% Hf, FBB8 + 2% Zr, and FBB8 + 4% Ti alloys have been analyzed from the ND patterns. The above measurements are conducted not only at room temperature, but also at elevated temperatures. Therefore, from the lattice constants at different temperatures, the coefficient of thermal expansion can be calculated, which is also an essential factor for the evaluation of mechanical properties at high temperatures. In-situ ND data also require the information extracted here as a reference for further analysis.

7. Coarsening Kinetics of NiAl/Ni_2TiAl Precipitates in the α-iron Matrix

Coarsening of the precipitates within the alloy system strongly relates to the life expectancy of the alloy working at high temperature. Assuming that after aging process, the volume fraction of the precipitates had reached the maximum value, if the precipitation size increases, the number of the precipitates decreases. Less precipitates therefore cannot block dislocations from moving freely, and the plastic deformation easily happens. Therefore, an ideal precipitation strengthening alloy should possess low coarsening kinetics for the precipitates. In the following paragraph, an investigation on the coarsening of the FBB8 + 2% Hf alloy will be presented.

7.1 Coarsening of FBB8 + 2% Hf alloy

The FBB8 + 2% Hf alloy sample is fabricated by Sophisticated company, and aged at 700 ^{o}C, for the durations of 24 hours (hrs), 44 hrs, 68 hrs, 84 hrs, 108 hrs, 150 hrs, and 174 hrs, respectively. The aged alloy was then analyzed by scanning-electron microscope (SEM) in order to quantitatively understand the microstructure evolution of the model alloy at 700 ^{o}C.

The average particle sizes of both micron-sized and nano-sized precipitates are determined by SEM images and the ImageJ software. As mentioned in Chapter 5, the micron-sized precipitates should be Laves phase precipitates, and the nano-sized precipitates are B2-phase precipitates. For each value of average particle size, there are at least 500 particles counted. Table 14 shows the heat-treatment duration and the average size of precipitates.

Figure 33 shows the particle size growth trend for both types of precipitates. As shown in Figure, after 24 hours of aging, there are no significant precipitation growth with increasing the aging duration, although the fitting line for the micron-sized precipitate particle size shows a slight increase trend with increasing the aging duration. For the nano-sized precipitate, the particle size remains nearly unchanged. Thus, it might indicate that after 24 hours of aging, the microstructure of the FBB8 + 2% Hf alloy has become stable.

Assuming that the precipitates coarsen linearly over time after 24 hours of aging, from the regression lines shown in Figure 33, it takes roughly 362 hours for the micron-sized precipitates to double their size (the diameter increases to roughly 1.26x of the original diameter, and the volume increases to 2x), and 395 hours for nano-sized precipitates.

7.2 Conclusion

The coarsening investigation on both precipitates within FBB8 + 2% Hf has been conducted. From the regression of the precipitate sizes at different aging times, both precipitates (Laves and B2 phases) can last 350-400 hours before doubling the size. However, since the data points are not enough for a reliable regression, experiments with the longer aging duration might be required in order to obtain the reliable coarsening data. From current results, within the aging duration of 174 hours, Laves phase coarsens roughly 1 micrometers, and the B2 phase coarsens roughly 20 nanometers, which is a roughly 12% to 12.5% increase in the diameter, and a 42% increase in the volume. This result shows that the coarsening of the precipitates within the FBB8 + 2% Hf alloy is significant. Since for the application of these alloys, they are supposed to work for decades, coarsening of precipitates, which leads to the decrease of strength, is not allowed.

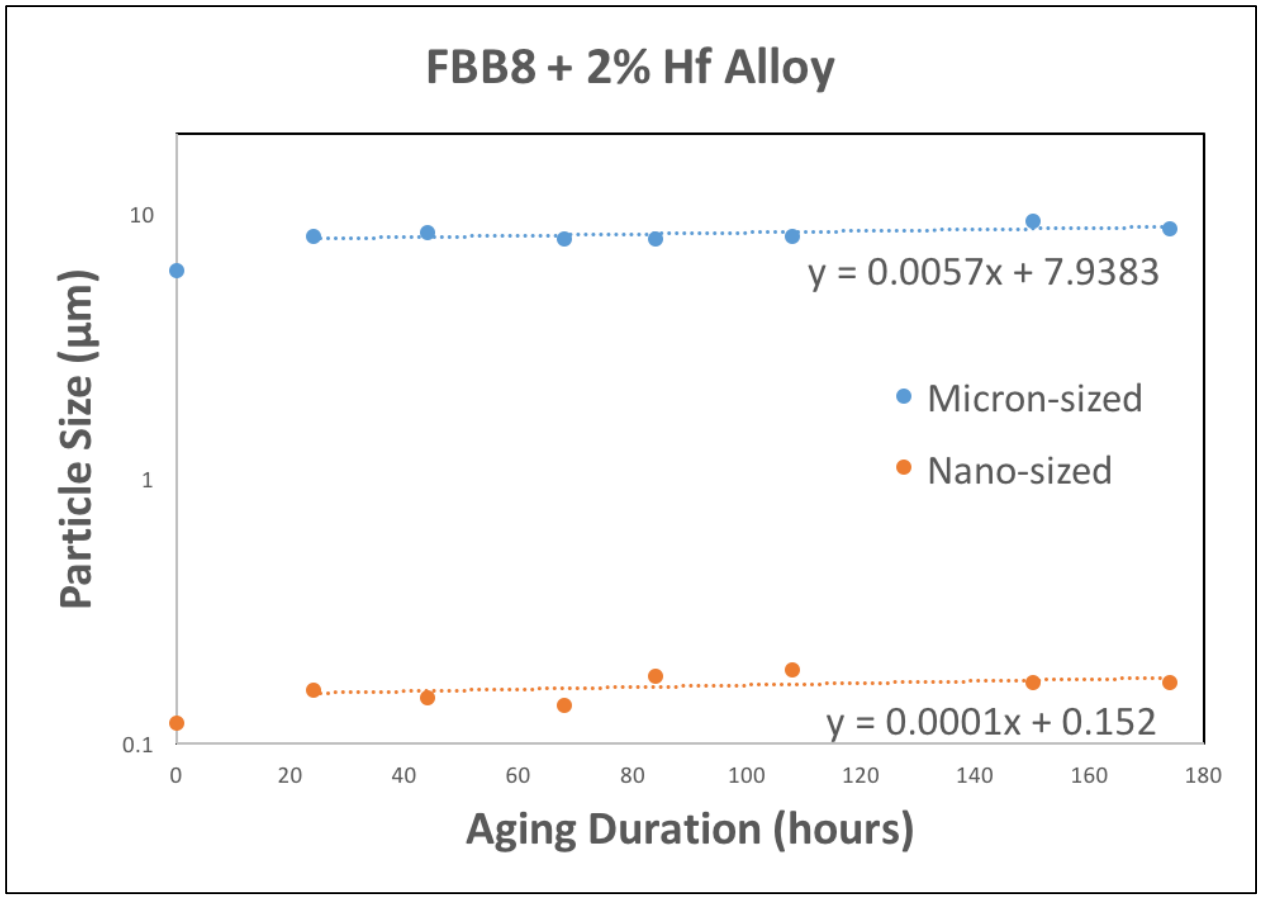

Figure 33. The trend of the precipitate-size evolution at the aging temperature of 700 °C. There are no significant changes in the precipitate size after 24 hours of aging.

Table 14. Aging duration (hrs) and the average size of the precipitates (µm) for the FBB8 + 2% Hf alloy

Duration	0 hrs	24 hrs	44 hrs	68 hrs	84 hrs	108 hrs	150 hrs	174 hrs
Micron-sized	6.13	8.20	8.55	8.04	8.09	8.24	9.40	8.76
Nano-sized	0.12	0.16	0.15	0.14	0.18	0.19	0.17	0.17

8. Systematical Creep Study on Model Alloys

Since this project majorly focuses on developing a novel creep-resistant material for the applications on the ultrasupercritical fossil-power plants, the creep resistance for the model alloys are the essential factor to be discovered. From the investigations shown in previous chapters, in order to achieve superior creep resistance in FBB8 alloy systems, hierarchical structure precipitates are necessary. The microstructural characterization on the FBB8 + 2% Hf and FBB8 + 2% Zr alloys shown in Chapter 5 presents a lack of the $L2_1$ phase formed. Therefore, the major strengtheners of these two alloys remain the same crystal structure as FBB8, which is the B2 phase. For the FBB8 + Ti alloys, if the Ti content is over 1.5%, there will be $L2_1$ phase formed parent with the B2 phase as a hierarchical structure, which improves the creep resistance. The following paragraphs are showing the creep test results to further prove the above statements, and also trying to optimize the creep resistance of the FBB8 + Ti alloys.

8.1 Experiment Procedure

Tension creep experiments were conducted at 700 ^{o}C on specimens with the geometry described in Chapter 4. The samples were loaded under constant load and then heated up to the target temperature, which is 700 ^{o}C in this case. Data points were collected every hour and recorded for the following analysis. The experiments last until the sample fractured.

Compression creep experiments were conducted at 700 °C on the polycrystalline specimens, with grain sizes ranging from 0.2 to 0.5 mm. The applied load was held constant until a well-defined minimum strain rate was observed and then the load was increased. This procedure was repeated up to the point where the cumulative creep strain reached 10%, a limit chosen to prevent sample barreling. At this point, the samples were air-cooled at a rate of ~ 50°C/min while under the terminal stress.

8.2 Creep Results for FBB8 + 2% Hf alloys

Two tension creep tests on the FBB8 + 2% Hf alloy at 700 ^{o}C had done. The alloy samples were aged, following the same aging process in Chapter 4. Each of tests was then conducted at stress levels of 150 MPa and 100 MPa, respectively. The creep test results are shown and compared with other materials in Figure 34. For the test at 150 MPa, the sample was failed in roughly 24 minutes, which is significantly faster than Ti-containing alloys. For the test at 100 MPa, the sample

was failed in in roughly 8 hours, and by selecting the section of the slowest strain in the curve, the creep rate is calculated, which is approximately $9 \times 10^{-8}\ s^{-1}$. Both samples went through necking and then failed, which indicated that the failure might not be caused by sample defects. Since the creep samples for these two tests failed in a relatively short of time, introducing the Hf into this alloy system, might cause the creep resistance decreases instead of increases. By comparing the FBB8 + 2% Hf alloy creep test results to other materials, it shows that the FBB8 + 2% Hf alloy has the similar creep resistance with FBB8, and the Laves phase caused by introducing Hf into the alloy system does not bring the enhancement on the mechanical properties.

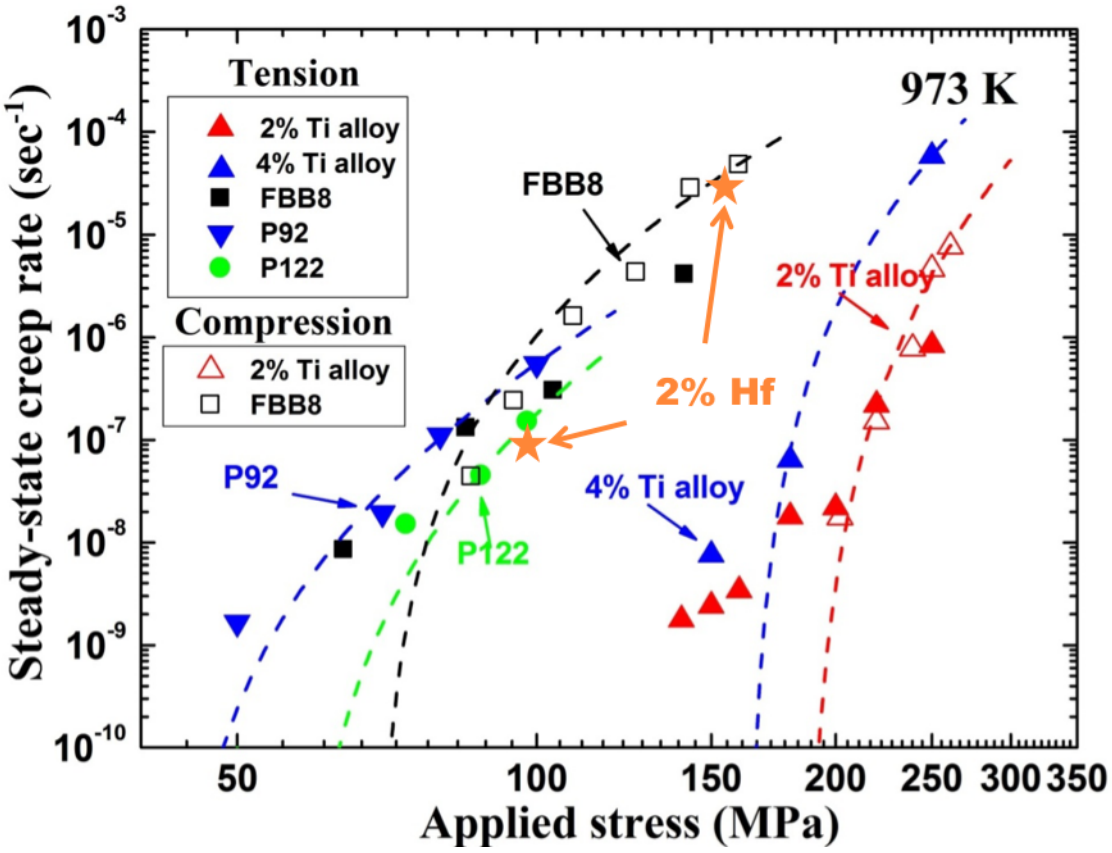

Figure 34. A comparison on steady state creep rate of the FBB8 + 2% Hf alloy and other alloy systems. The FBB8 + 2% Hf alloy has similar creep performance as FBB8, which shows that by introducing the Hf into the FBB8 alloy system does not bring obvious enhancement on mechanical properties.

8.3 Creep Results for FBB8 + 0.5% Hf-1.5% Ti alloys

Compression-creep results showing the steady-state creep strain rates as a function of applied stress at 700 °C for FBB8 + 0.5% Hf-1.5% Ti alloys are displayed in a double-logarithmic plot, Figure 35. The compression-creep experiments begin with a low stress to measure the threshold stress, σ_{th} , at which creep does not appear to occur or the creep rate is very slow after the first several tens of hours of the experiments [58]. This threshold stress normally appeared in the second-phase-strengthened alloy that has the higher strength than both the pure matrix itself and the solution-strengthened alloy.

A value of the threshold stress, σ_{th}, can be obtained, utilizing the modified Mukherjee-Bird-Dorn equation [59]:

$$\dot{\varepsilon} = A\left(\frac{\sigma_a - \sigma_{th}}{\mu}\right)^n \exp\left(\frac{-Q}{k_B T}\right) \tag{16}$$

where A is a constant, σ_a is the applied stress, μ is the shear modulus of the matrix, n is the steady-state stress exponent of the matrix, Q is the creep-activation energy for creep, k_B is Boltzmann constant, and T is the absolute temperature. Using the method described above, the threshold stress is calculated by a linear least-squares regression of $\dot{\varepsilon}^{1/n}$ vs. σ_a. A matrix stress exponent of $n = 4$ was employed, which yields a good linear fit in plots of $\dot{\varepsilon}^{1/n}$ vs. σ_a for all studied creep temperatures. The threshold stresses are derived by the y-axis intercept of the linear plot of regression analysis, represented in Table 15. In the regression analysis, the lower bound strain rate data points, marked by downward arrows, were not used in the evaluation of the threshold stresses. From the creep test, the creep resistance in the FBB8 + 1.5% Ti alloy is positioned between 0 and 2 wt.% Ti alloys. The threshold value is, however, not proportional to the fraction of the Ti concentration. Second, the addition of the 0.5 wt.% Hf into the FBB8 + 1.5% Ti decreases the creep resistance from 141.6 to 124.5 MPa for the threshold value.

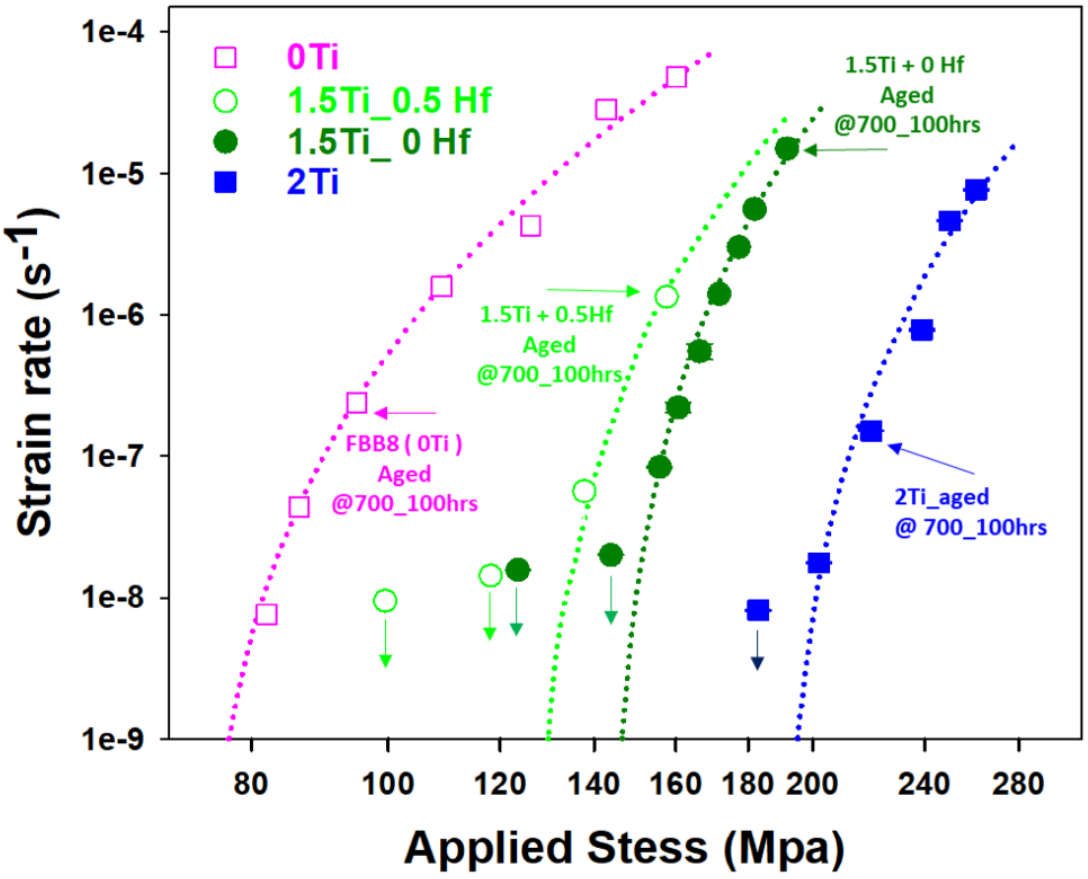

Figure 35. Double logarithmic plot of applied stress vs. steady-state strain rate of compression-creep tests performed at 700°C for FBB8 (pink), FBB8 + 1.5% Ti - 0.5% Hf (green), FBB8 + 1.5% Ti (dark green), and FBB8 + 2% Ti (blue). Data for FBB8 and FBB8 + 2% Ti alloys were obtained from Ref. [60]. Equation (16) was used to fit (dash lines) the experimental data (see the text). Data with the downward arrow indicates upper-bound values (the discernable creep rate not achieved).

Table 15. Comparison on creep threshold stresses for the FBB8 + Ti alloys.

Threshold stress of the FBB8, FBB8 + 0.5% Hf-1.5% Ti, FBB8 + 1.5% Ti, FBB8 + 2% Ti alloys			
Sample (wt%)	Aging condition	Creep temperature	Threshold stress (Mpa)
FBB8 (0%Ti)	Aged @ 700 ^{o}C for 100 hours (hrs)	700 ^{o}C	70.8
FBB8 + 1.5% Ti-0.5% Hf	Aged @ 700 ^{o}C for 100 hrs	700^{o}C	124.5
FBB8 + 1.5%Ti + 0% Hf	Aged @ 700 ^{o}C for 100 hrs	700 ^{o}C	141.6
FBB8 + 2%Ti	Aged @ 700 ^{o}C for 100 hrs	700^{o}C	183.7

8.4 Creep Results for FBB8 + Ti series alloys

Figure 7 displays the creep behavior for the alloys FBB8 + 1.5%Ti to 4.0%Ti at 700 ^{o}C. Double logarithmic plots of steady-state creep strain rate as a function of applied stress represent the compression creep behaviors performed at 700°C for FBB8-1.5%Ti (sky blue), -2.0%Ti (red), -2.5%Ti (orange), -3.0 (green), -3.5 (dark green), and FBB8-4%Ti (blue). The compression creep experiment begins at the low stress to measure the threshold stress, σ_{th}, below which creep is a very slow strain rate (below 10^{-9}) after the first several tens of hours of the experiments [58]. The low strain rates in the ranges 1 x 10^{-10} to 1 x 10^{-8} s^{-1} that cannot be accurately measured in the laboratory timeframe are marked with downward arrows. Creep data for FBB8-2 and 4wt% Ti samples in prior studies [41] are also added as empty red triangles and blue circles, respectively, along with results from this study for comparison in the same condition of experiment. A value of threshold stress, σ_{th}, is obtained utilizing Eq. (16) described in Chapter 8.3. The threshold stresses are derived by the y-axis intercept of the linear plot of its regression analysis, represented in Table 16. In the regression analysis, the data points with lower bound strain rate, marked by downward arrows, were not used to evaluate the threshold stresses. The dashed lines fits the creep experimental data using Eq. (16).

Several trends are shown in Figure 36 on the effect of Ti additions on the creep properties of the alloy. First, the creep resistance is increased by the addition of Ti in the range of 1.5% to

3.5% Ti, demonstrating the strong effect that the volume fraction of the $L2_1$-Ni_2TiAl phase in the hierarchical precipitate has on the creep strength. Second, there is no linear relationship between the creep resistance and the $L2_1$ volume fraction in the precipitate even though the volume fraction of $L2_1$ phase increases linearly with the Ti addition. The creep resistance significantly increases between the 1.5% Ti and 2.0% Ti, whereas the gap of increase is reduced in the range from 2.0 to 3.5 wt.% Ti additions. Third, although the presence of titanium has an overall positive effect on creep properties, there is a sharp drop of creep resistance when 4 wt.% Ti is added. This trend is related to the microstructural change of the precipitate between 3.5 and 4 wt% Ti in FBB8 alloy, as demonstrated in the TEM analysis. Finally, even with an evolving microstructure, FBB8 + 3.5% Ti consistently displays the best creep resistance of the six alloys tested here, with roughly a two order of magnitude decrease in the threshold value, over the FBB8 + 1.5% Ti alloy. This increase in the creep performance demonstrates that the precipitate's microstructure present in FBB8 + 3.5% Ti is the most effective at blocking the motion of dislocations in the alloys tested.

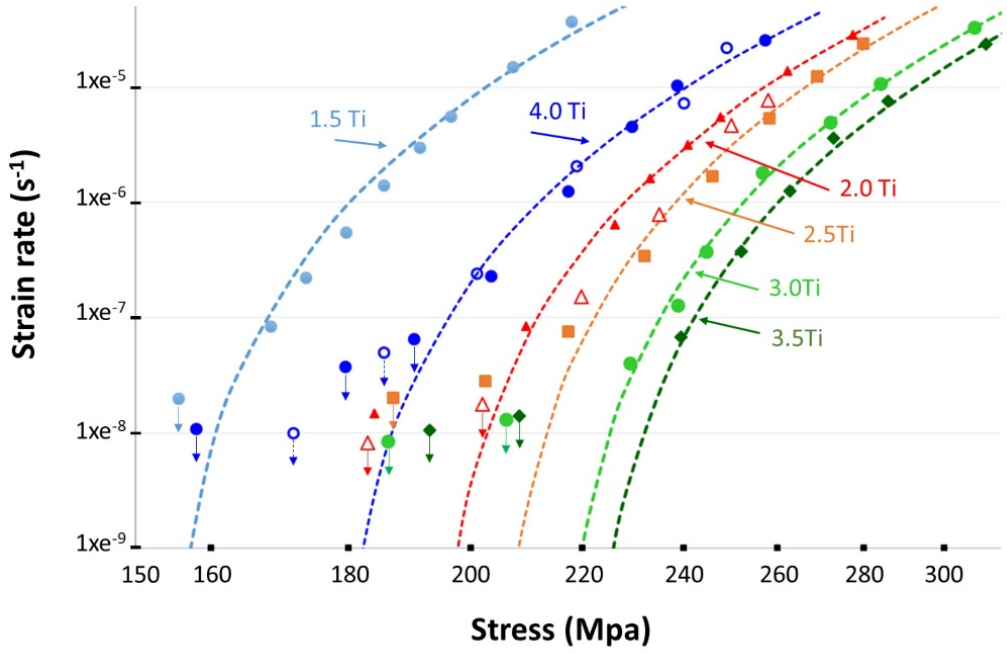

Figure 36. Double logarithmic plot of applied stress vs. steady-state strain rate of compression creep tests performed at 700 °C for FBB8 + 1.5% Ti (sky blue), FBB8 + 2.0%Ti (red), FBB8 + 2.5% Ti (orange), FBB8 + 3.0% Ti (green), FBB8 + 3.5% Ti (dark green) and FBB8 + 4% Ti (blue). Data for FBB8-2Ti and FBB8-4%Ti alloys (empty triangles and circles, respectively) were obtained from Ref. [41], which are added for the comparison with the current creep data. Equation (16) was used to fit (dash lines) the experimental data. Data with the downward arrow indicates a lower bound value that a discernable creep rate is not achieved.

Table 16. Creep threshold stresses for the FBB8-1.5Ti, 2.0Ti, 2.5Ti, 3.0Ti, 3.5Ti, and 4.0Ti ferritic alloys. Sample aged at 700^{o}C for 100 hrs and creep tested at 700^{o}C.

Samples	Threshold stress (MPa)
FBB8 + 1.5% Ti	156.4
FBB8 + 2.0% Ti	189.2
FBB8 + 2.5% Ti	201.9
FBB8 + 3.0% Ti	212.9
FBB8 + 3.5% Ti	218.8
FBB8 + 4.0% Ti	175.5

8.5 Conclusion

The creep tests on the FBB8 series alloys show that (1) the creep resistance of FBB8 + 2% Hf does not improve from adding Hf into FBB8, and the creep resistance remains similar to the original FBB8. From the investigations shown in previous chapters, it can now be concluded that without forming the $L2_1$ phase, the FBB8 + 2% Hf cannot further improve creep resistance, (2) within all the FBB8 + Ti alloys, FBB8 + 3.5% Ti has the greatest creep resistance (the threshold stress of 218.8 MPa at 700 ^{o}C). Combined with the microstructural characterization results, FBB8 + 3.5% Ti has a hierarchical structure precipitate with a $L2_1$/B2 ratio of 4, which means that when the $L2_1$ phase becomes dominant and combines with a slight amount of the B2 phase, the effect of dispersion strengthening goes optimized.

9. In-situ Creep Study on Model Alloys under Neutron Diffraction

The creep resistance of model alloys at high temperatures needs to be further improved, by investigating on the deformation mechanisms at the local phase and grain levels. Diffraction methods enable the accurate determination of the d-spacings in various phases and/or differently-oriented crystal grains, which leads to the ability to quantify internal stresses at the crystal level. ND provides the crucial structural information on mesoscopic scales (less than 1 μ m), specifically the accurate determination of lattice strains in differently-oriented grains and/or multiple phases. The large beam size and great penetration of neutrons into matters enable the illumination on a substantial quantity of grains, from which structural mechanisms in the bulk can be determined with good statistics. In contrast to the residual stress/strain state, as measured by ex-situ characterization techniques, in-situ measurements under loading at high temperatures probe the dynamic lattice-strain evolution during deformation. Since diffraction allows the precise determination of d-spacings, it can be used to measure elastic lattice strains. In the following paragraph, the in-situ ND tests on FBB8 + 2% Hf and FBB8 + 2% Zr alloys will be presented and discussed.

9.1 In-situ neutron diffraction on FBB8 + 2% Hf and FBB8 + 2% Zr alloys

The in-situ neutron experiment is conducted as a compressive creep test at 700 ^{o}C and different stress levels (80 and 100 MPa) at the SNS of ORNL. The samples of FBB8 + 2% Hf and FBB8 + 2% Zr alloys are fabricated as a cylinder, with the length and diameter ratio of 2:1. After the fabrication, the samples were aged described in Chapter 4. During the compressive creep tests, the incident neutron beam constantly hit the sample and diffracted, collected by two detectors, which are able to collect the axial and radial responses of the sample under stress, respectively. Figure 26 shows a schematic figure for the setup of the in-situ neutron experiment. During the experiment, the compression sample will be heated up and dwelled at 700 ^{o}C, and applied with constant loading, depending on the stress level.

Figure 37 shows the macroscopic strain vs. time plot for the in-situ experiments. The strain vs. time curves fluctuate because the MTS machine tries to maintain a constant load on the sample, and therefore keeps on micro-adjusting the applied stress. As a result, the samples experienced stressed-relax cycles, and the macroscopic strain fluctuates. In Figure 37, the positive values of strains refer to compressive strains, and the negative values refer to tensile strains. For tests with

80 MPa constant stress, the macroscopic strain vs. time curves start with significant amount of negative strain values, and gradually goes to positive strain values, which indicates that the tested samples first expanded and then compressed. The expansion part was due to thermal expansion, and the compression part was due to the compressive load on the tested sample. From the shape of the curves in Figure 37, none of these tests had entered the steady-state creep regime. Therefore, the strain vs. time curve cannot be analyzed simply by conventional creep equations, which are mostly formulated, based on the steady-state creep, with a constant strain rate.

Figure 38 presents the lattice strain for the tests. For each test, the data had divided into 10 data points, and then through the Rietveld refinement of the whole peak-fitting method performed by the GSAS, the lattice constant can be extracted from the fitting parameter, and further coverts into lattice strain value. In Figure 38, in both tests on FBB8 + 2% Zr, the lattice strains for both the precipitates and the matrix are sharing the same trend during the whole period of testing. The lattice strain should be a constant when the sample is under constant loading, since it represents the elastic strain. However, both FBB8 + 2% Hf tests (80 MPa and 100 MPa) show abnormal lattice strains for the B2 phase from the bank 1 (collecting compressive data). For the test of FBB8 + 2% Hf at 80 MPa, the lattice strain (elastic strain) of the B2 phase keeps on piling up. For the test of FBB8 + 2% Hf at 100 MPa, the lattice strain of the B2 phase drops down gradually. These abnormal reactions concerning both tests on FBB8 + 2% Hf shows that the B2 phase is releasing strains during the test at 100 MPa, and accumulating strain during the test at 80 MPa. The reason could be varied, one possibility could be due to the Laves phase actually forming small precipitates that dispersed within the matrix. In the FBB8 + 2% Hf alloy, although most of Laves phase particles segregate as large particles or as grain-boundary films, however there still exist quite an amount of Laves-phase particles that disperse in the matrix. This feature only happens within the FBB8 + 2% Hf alloy, but not in the FBB8 + 2% Zr alloy. Figure 8 (the FBB8 + 2% Hf alloy) and Figure 11 (the FBB8 + 2% Zr alloy) shows a clear view on the differences of the Laves phase within these alloys. In Figure 8, within the matrix, there are plenty of needle-shaped precipitates that disperse within the matrix. However, in Figure 11, there are no such needle shaped precipitates present. These needle-shaped, Laves phase precipitates could be secondary obstacles that prevent the dislocation from moving, therefore, taking some part of the load from the B2 phase precipitates. Anyway, further evidence is required in order to prove the above statement. From the lattice-strain

plots, the elastic strains of the samples are around 0.08% to 0.1%. Therefore, most of the macroscopic strains is due to plastic deformation.

In Figure 37, since the strain vs. time curves represent the primary stage creep, which the creep-strain rate hasn't reached the minimum yet. Several fitting equations, including the power-law equation, logarithmic equation, exponential equation, and hyperbolic-sine equation, based on different assumptions summarized in Table 17, and applied for the strain vs. time curves in order to obtain fitting parameters.

Table 18 shows the fitting parameters and coefficient of determination (R^2) of the fitting with the power-law equation. The power law has the advantage that no matter how the stress applied, it remains the same equation form, which could be great for stress analysis. In creep studies, the power-law equation describes the high-temperature plasticity. Tests over $0.4T_M$ (melting temperature) are able to fit with the power-law-creep equations [61]. The power-law creep describes a rate-dependent plastic deformation, usually with the stress exponent of $n = 3$ to 10. As shown in Table 3, all 4 curves statistically fit well with the power-law equation, with R^2 over 0.94. The stress exponent, n, has been assigned as 4, which has been discovered from the investigations on FBB8 [62].

The application of the logarithmic-creep equation fits for the low temperature region ($T < 0.3T_M$), which does not fit with the testing condition of this in-situ neutron test. However, for testing, we still do the fitting on the data sets. A logarithmic function has a similar shape with the primary creep curves, which starts with faster strain rates and gradually slows down to a constant. The original paper that features the logarithmic creep is a study of the creep of the indiarubber, glass, and soft metals, such as gold [63]. Since the in-situ experiment is a test at high temperatures and hard metals, the very assumption of a logarithmic-creep equation should not fit with the experimental data. However, in Table 19, a summary of the fitting parameters and R^2, all four stes of data fit well with the logarithmic equation, with R^2 higher than 0.93, only slightly worse than the power-law equation.

The exponential equation, also known as Garofalo/Dorn equation, is an equation that features the exponential term [64]. Compared to the power-law equation, the exponential equation fits creep at higher stresses, and the power-law equation fits at lower stresses. The exponential equation itself does not fit with the shape of the creep curve. However, the form of $y = [1 - \exp(-x)]$ fits. Table 20 summarized the fitting parameters and R^2. Among all the equations

that had tested, and the exponential equation fits the best, with R^2 higher than 0.95 for all data sets. Though the exponential equation fits the best with the experimental data sets, the data-point distribution does not really randomly distribute around the fitting curve. As shown in Figure 39(c), data points that are located lower than the strain of 0.08 are mostly higher than the fitting curve, which shows that this fitting curve cannot represent the prior part of the trend of the data-point distribution. Figure 39(a) also presents that compared to the exponential equation, the power-law equation does not have this issue.

The last equation to be fitted to the data points is the hyperbolic sine equation, which is a creep law that is supposed to cover the range of both high and low stresses [65]. However, in the fitting shown in Table 21, the hyperbolic sine law cannot fit with the data points at all. The hyperbolic-sine equation does have the shape similar to the data-point distribution. Nevertheless, no matter how the parameters had been tuned in a reasonable range, the fitting cannot reach an acceptable status.

Figure 39 exhibits the comparison between these four equations, as mentioned above, the power-law equation, logarithmic equation, and exponential equation can fit pretty well, with R^2 at least higher than 0.93. The hyperbolic-sine equation cannot fit at all. However, the power-law equation has better statistics than the exponential equation and logarithmic equation, because the data points can randomly distribute around the power-law-fitting curve.

Another creep equation that represents the complete creep strain history (primary + steady-state creep regimes) is employed in the analysis of these strain vs. time curves, as shown below [66]:

$$\varepsilon_{\text{creep}} = \frac{C\sigma^n t^{m+1}}{m+1}\exp\left(\frac{-Q}{RT}\right) \tag{17}$$

where C is a constant in $MPa^{-n}\ s^{-(m+1)}$, σ is the applied stress in MPa, n is stress exponent, t is time in second, m is a dimensionless constant, and Q is the activation energy of the creep in kJ/mol. The equation can be applied to fit the strain vs. time curve, and based on fitting, extracted the creep parameters. Based on the preliminary investigation on both FBB8 + 2 wt.% Hf and FBB8 + 2 wt.% Zr alloys, these two alloys have similar mechanical properties with FBB8. Table 22 shows the creep parameters that are extracted from the fitting. These parameters can be further applied to the creep behavior modeling in the future. For example, Eq. (16) requires parameters, *n* and *Q*, for the calculation of the steady-state creep rate, the parameters extracted here can be therefore applied.

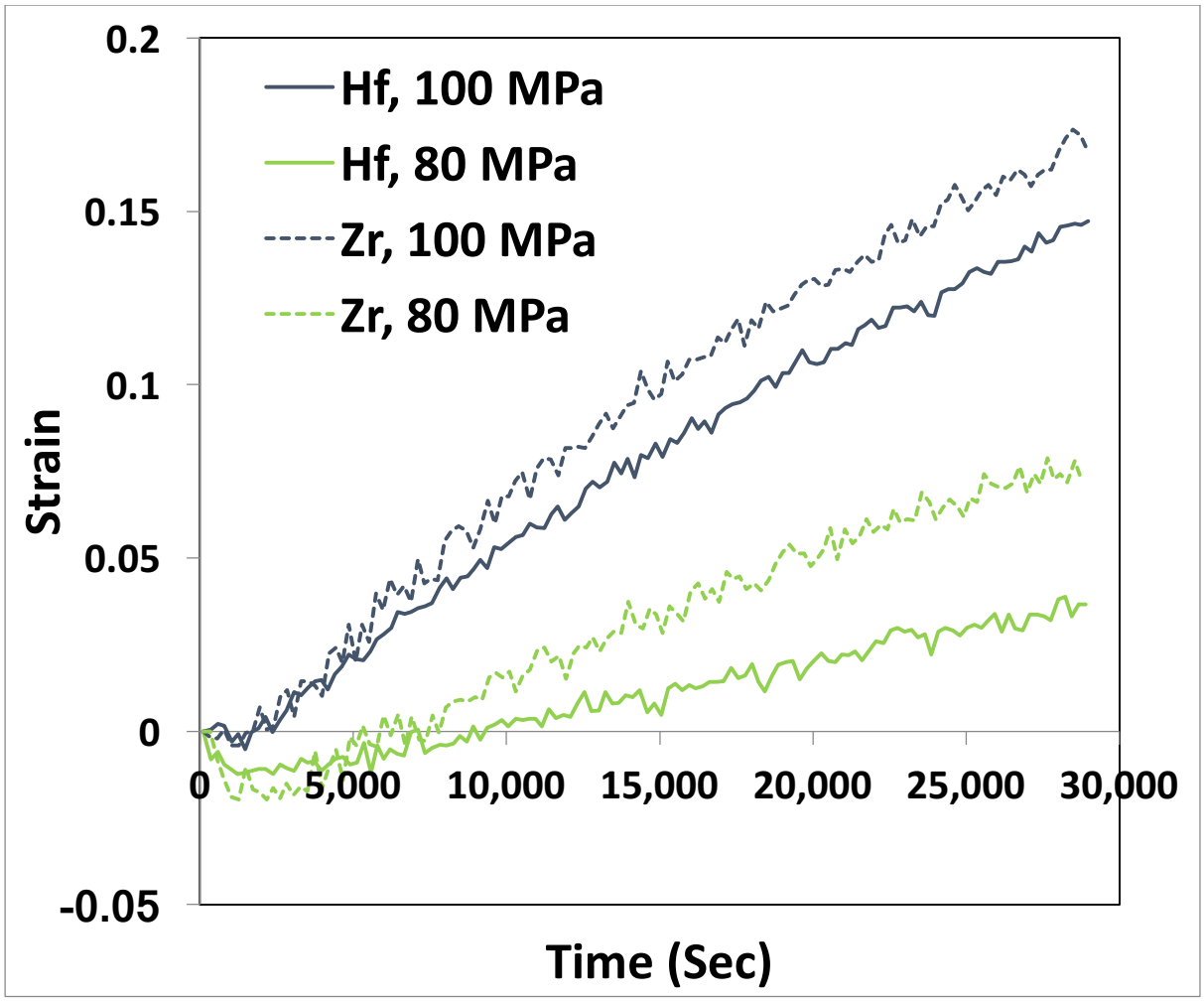

Figure 37. The macroscopic strain v.s. time plot for both FBB8 + 2 wt.% Hf and FBB8 + 2 wt.% Zr at 700 ^{o}C. Positive values of strains represent compressive strains, and negative values represent tensile strains.

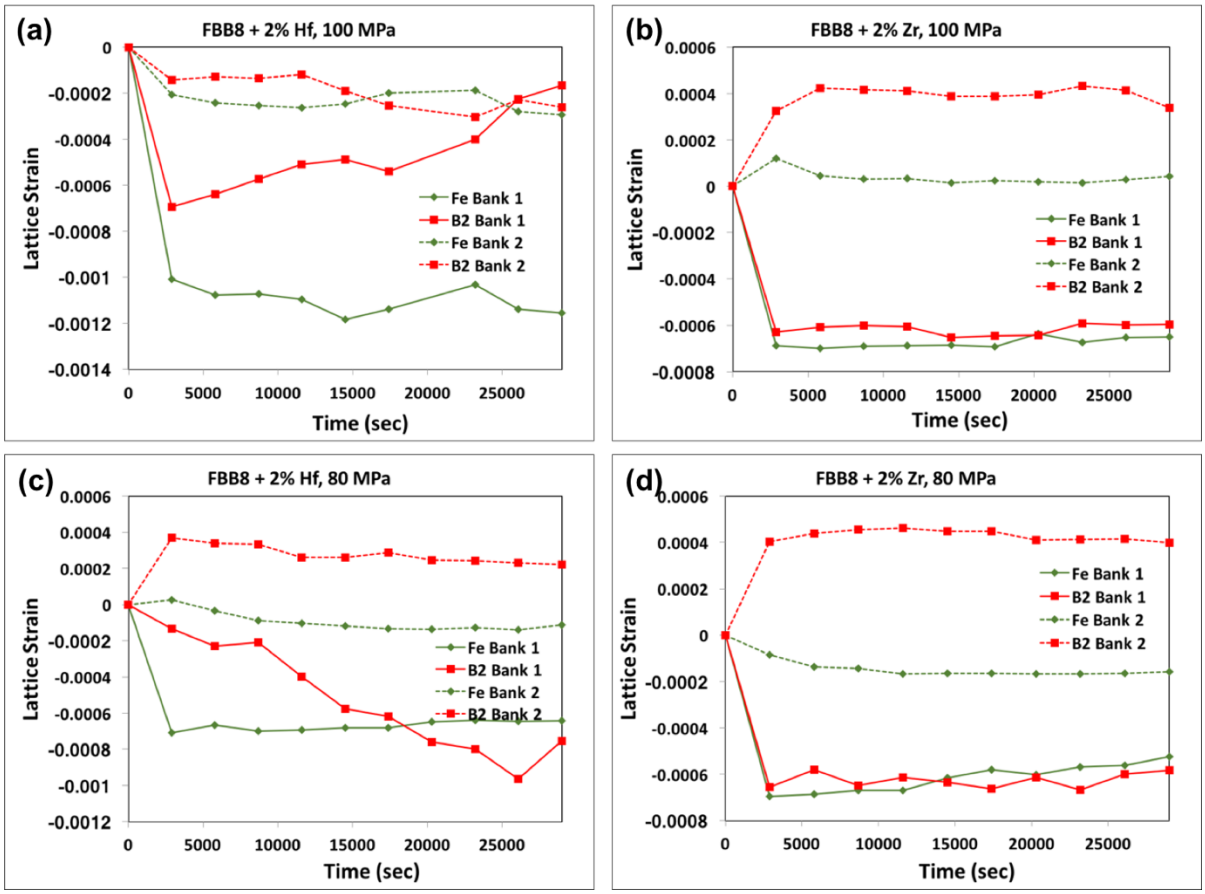

Figure 38. The lattice strain v.s. time plots for (a) FBB8 + 2 wt.% Hf at 100 MPa, (b) FBB8 + 2 wt.% Zr at 100 MPa, (c) FBB8 + 2 wt.% Hf at 80 MPa, and (d) FBB8 + 2 wt.% Zr at 80 MPa. The lattice strains at (b) and (d) are almost remained constant during the period of testing. However, for (a) and (c), lattice strains for the B2 phase act abnormally, the lattice strain in (a) of the B2 phase decreases and in (c) it keeps on increasing, which could be due to the dislocation-precipitation interaction.

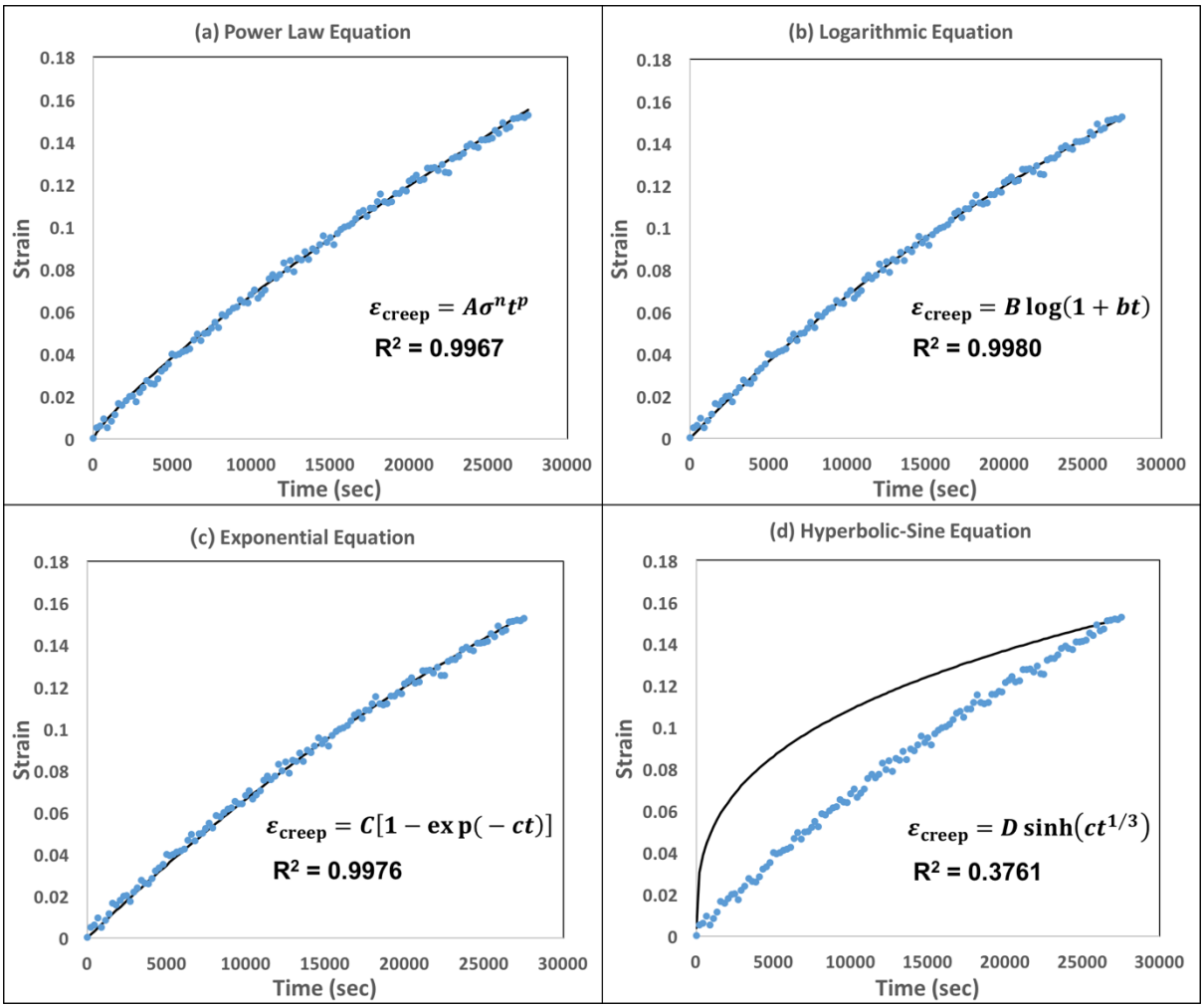

Figure 39. The fittings of strain vs. time curves for FBB8 + 2% Hf at 100 MPa, 700 ^{o}C as an example. (a) The fitting with the power-law equation, with great fitting and randomly-distributed data points around the fitting curve, implies a great statistic for the fitting. (b) The fitting with the logarithmic equation, the logarithmic equation also fits well as the power-law equation, but it should be applied to the lower-temperature condition ($T < 0.3T_M$). (c) The fitting with the exponential equation fits the best concerning the aspect of R^2. Nevertheless, most of the data points in the prior part of the fitting lies above the fitting curve, therefore not randomly distributed. (d) The fitting with the hyperbolic-sine (Sinh) equation. The equation and the data points does not fit at all.

Table 17. The primary-creep equations

Equation	Mathematical Form	Parameters	Reference
Power Law	$\boldsymbol{\varepsilon_{creep} = A\sigma^n t^p}$	$\boldsymbol{A}$: constant $\boldsymbol{n}$: stress exponent $\boldsymbol{p}$: dimensionless constant	Graham [67]
Logarithmic	$\boldsymbol{\varepsilon_{creep} = B\log(1 + bt)}$	$\boldsymbol{B}$, $\boldsymbol{b}$: constants for the particular pull	Phillips [63]
Exponential	$\boldsymbol{\varepsilon_{creep} = C[1 - \exp(-ct)]}$	$\boldsymbol{C}$, $\boldsymbol{c}$: constants	McVetty [68]
Hyperbloic-Sine Law	$\boldsymbol{\varepsilon_{creep} = D\sinh(ct^{1/3})}$	$\boldsymbol{D}$: constant	Conway [69]

Table 18. The creep parameters extracted from the fitting of the strain vs. time curve for the fitting of the power-law equation

Parameter	$\boldsymbol{A}$	$\boldsymbol{n}$	$\boldsymbol{p}$	$\mathbf{R^2}$
Hf, 100 MPa	3.55E-37	4	0.82	0.9976
Hf, 80 MPa	1.18E-37	4	0.82	0.9404
Zr, 100 MPa	3.90E-37	4	0.82	0.9851
Zr, 80 MPa	2.30E-37	4	0.82	0.9768

Table 19. The creep parameters extracted from the fitting of the strain vs. time curve for the fitting of the logarithmic equation

Parameter	$\boldsymbol{B}$	$\boldsymbol{b}$	$\mathbf{R^2}$
Hf, 100 MPa	0.52	0.000035	0.9980
Hf, 80 MPa	0.175	0.000035	0.9334
Zr, 100 MPa	0.58	0.000035	0.9895
Zr, 80 MPa	0.335	0.000035	0.9726

Table 20. The creep parameters extracted from the fitting of the strain vs. time curve for the fitting of the exponential equation

Parameter	C	c	R^2
Hf, 100 MPa	0.35	0.000021	0.9975
Hf, 80 MPa	0.115	0.000021	0.9534
Zr, 100 MPa	0.39	0.000021	0.9918
Zr, 80 MPa	0.225	0.000021	0.9684

Table 21. The creep parameters extracted from the fitting of the strain vs. time curve for the fitting of the hyperbolic-sine equation

Parameter	D	c	R^2
Hf, 100 MPa	240	0.000021	0.3761
Hf, 80 MPa	80	0.000021	0.1412
Zr, 100 MPa	270	0.000021	0.3048
Zr, 80 MPa	135	0.000021	0.4329

Table 22. The creep parameters extracted from the fitting of strain v.s. time curve

Parameter	C ($MPa^{-n}\ s^{-(m+1)}$)	n	m	Q (J/mol)
Hf, 100 MPa	0.0000015	4	- 0.196	571,000
Hf, 80 MPa	0.0000015	4	- 0.18	581,500
Zr, 100 MPa	0.0000017	4	- 0.196	571,000
Zr, 80 MPa	0.0000035	4	- 0.196	581,500

9.2 Conclusion

In-situ neutron diffraction tests on FBB8 + 2% Hf and FBB8 + 2% Zr had been done. The lattice-strain results show that the behaviors of the B2 phase under a constant load for FBB8 + 2% Hf and FBB8 + 2% Zr are different, which could be due to the different microstructures of the respective alloys. For the creep strain analysis, the shape of the strain v.s. time curve shows the creep tests were under primary stage creep. Therefore, several primary creep equations have been used in the fitting of the strain v.s. time curve. The power-law equation has the best statistic fitting among all the equations. Parameters, such as the stress exponent and creep activation energy, have been extracted, and can further apply to the steady-state creep models. The in-situ ND tests basically tell us (1) FBB8 + 2% Hf and FBB8 + 2% Zr alloys plastically deform in the same pattern, and both follows the power-law creep with similar activation energy. Hence their high-temperature plastic deformation mechanism is the same, and (2) elastic deformations for both alloys are different, due to slightly different microstructures. In FBB8 + 2% Hf alloy, there could be Laves-phase particles that share the load. However, in FBB8 + 2% Zr there are only B2 phase particles that take the load.

10. Dislocation-dynamics Simulations of Creep Resistance

Two-dimensional dislocation-dynamics (DD) simulations are performed to determine the increase in yield stress due to ordered β′ (B2)-NiAl nanoprecipitates within a ferritic matrix. Parametric studies investigate three precipitate volume fractions (10, 13, and 20 %) and various radii (from 1 to 75 nm), associated with the yield-stress mechanism based on precipitate bypassing and/or shearing by single and super-dislocations of an edge or screw character. Yield stresses from DD simulations for various precipitate radii with a volume fraction of 13% (corresponding to various stages of aging) are then compared to a variety of analytical models for strengthening by ordered precipitates.

10.1 Introduction

The NiAl nano-precipitates are coherently embedded in a β (body-centered-cubic, BCC)-iron matrix, resulting in a β/β′ microstructure, which is responsible for outstanding ambient and elevated temperature strengths [70]. The dislocation/precipitate interaction dictates the strength of these ferritic steels because the NiAl precipitates block the motion of dislocations, thereby increasing the yield stress at ambient temperature and decreasing the rate of plastic flow at elevated temperatures. Mechanisms include precipitate shearing where the order/disorder mechanism is active, and long-range elastic interactions resulting from the modulus and lattice parameter mismatch, which may lead to precipitate bypass via dislocation loops. Order/disorder strengthening occurs when a single dislocation or dislocation pairs, often referred to as a "super-dislocation", shear through a long-ranged ordered precipitate. Under a sufficient stress, the leading dislocation shears through the precipitate, creating an antiphase boundary (APB), and is followed by the trailing dislocation, which then shears through the same precipitate, restoring order to the system. Unlike the FCC metal, (BCC) α-Fe contains up to 48 slip systems along which dislocations can propagate. However, slip along the <111> direction in the {110}-type plane has been shown to be preferred at low temperatures, and this slip system is used in the present work. The two-dimentional (2-D) DD simulations require far fewer computational resources and shorter times to simulate a given material but are geometrically restricted to a single 2-D glide plane and hence are unable to incorporate dislocations that move into different slip planes via three-dimentional (3-D) dislocation phenomena, such as cross slip and climb. However, the movement of dislocations into a different slip plane is thermally activated and is, thus, expected to be negligible when simulating

dislocation propagation at low temperatures. In the present study, we utilize a 2-D DD line dislocation code created by Mohles and coworkers [71-73] to study the precipitate-strengthened (BCC)-iron structure by the parametric study for the NiAl precipitate size and volume fraction.

10.2 Simulation Models

10.2.1 Line-dislocation models

The DD model used here simulates one or two dislocations propagating through a field of precipitates embedded within a matrix, acting as obstacles to the motion of dislocations. Each dislocation is comprised of multiple nodes, with each node being subjected to up to four interaction forces originating from other dislocations, obstacles, the external applied stress, and the drag force. The nodes positions are adjusted iteratively until a net zero stress is reached, using the following force-balance equation:

$$\tau_{ext} + \tau_{obst} + \tau_{dis} + \tau_{drag} = 0 \tag{18}$$

where τ_{ext} is the external stress applied to the system, τ_{obst} is the stress associated with the dislocation interacting with the precipitates, τ_{disloc} is the stress induced by the dislocation interacting with itself and/or other dislocations, and τ_{drag} is the stress due to a viscous drag, which is proportional to the nodes local velocity normal to the dislocation line. At the beginning of the simulation, the dislocation is a straight line at the bottom edge of the obstacle field with a periodic boundary condition imposed (as if the glide plane wrapped around a cylinder, and the dislocation moved vertically parallel to the cylinder axis). This model can simulate either a single dislocation or a pair of interacting dislocations of the same sign and Burgers vector (more commonly known as a super-dislocation) propagating through the obstacle field. An external stress, τ_{ext}, is applied to the system to initiate dislocation motion and is initially set to a value of ~ 10 % below the stress at which large-scale dislocation slip occurs (i.e., the critical resolved shear stress, CRSS). This trend drives the dislocation(s) through the obstacle field until a static equilibrium is achieved at each node. The external stress is then increased by an increment, $\delta\tau$, a value usually ~ 2% of the estimated CRSS, which allows the dislocation(s) to continue to progress through the obstacle field until the next static equilibrium is reached. This process is repeated as the dislocation glides through the precipitate field while either shearing through the precipitates or bypassing them with

the concomitant formation of Orowan loops, with the dominant bypass mechanism being dictated by a precipitate average radius, <R>, and volume, ϕ, as described in more detail in a later section. As τ_{ext} increases, the lowest value necessary for the dislocation(s) to slip over long distances (i.e., to reach the upper edge of the precipitate field) is taken to be the strengthening increment due to precipitation, $\Delta\tau_p^{sim}$, for that particular obstacle field. For a given obstacle field, multiple runs were performed with a particular set of initial conditions (τ_{ext} , δτ) with the resulting $\Delta\tau_p^{sim}$ remaining constant within 1 - 3 MPa.

10.2.2 Analytical equations for order strengthening

Various closed-form equations [74, 75] have been developed to model strengthening effects of long-ranged ordered precipitates. Many of these equations are based on a force balance of the paired dislocation configuration with a leading dislocation (D1) shearing through precipitates and thus creating an APB, followed by a trailing dislocation (D2) restoring order in the precipitates. We use here the following equation for the strengthening increment, τ_p:

$$\tau_p = \frac{\gamma_{APB}}{2b}\left\{\frac{d_1}{L_1} - \frac{d_2}{L_2}\right\} \tag{19}$$

where d_i is the length of leading (I = 1) or trailing (I = 2) dislocation within the precipitate, and L_i is the mean center-to-center spacing of the leading or trailing dislocation. The ratio, $\frac{d_2}{L_2}$, is often set equal to $\alpha\phi$ where α is a constant ranging from 0 to 1 multiplied by the volume fraction, ϕ, where a value of α = 0 implies that the APB pulls the trailing dislocation out of all of the precipitates, and α = 1 implies that the trailing dislocation is completely straight. For the purpose of this study, α is taken as unity since the trailing dislocation experiences minimal to no repulsive stress while bypassing precipitates with either mechanism and, thus, maintains its roughly-straight geometry. The derivation for the term of the leading dislocation, $\frac{d_1}{L_1}$, varies, depending on the geometry and strength of the precipitate.

Several other equations exist, which predict the strengthening increment, τ_p, for alloys containing precipitates or dispersoids with a volume fraction, ϕ, and radii, <R>, which we use here to show the variations among analytical models as well as to compare with our DD simulations. The Friedel equation for the case where the particles are sheared is given by:

$$\tau_p^{Friedel} = \frac{2S}{b\langle R\rangle\sqrt{\pi\omega_q}}\sqrt{\phi}\left(\frac{\gamma_{APB}\omega_r\langle R\rangle}{S}\right)^{3/2} \tag{20}$$

where ω_r and ω_q are spherical correction constants, which take into account for 2-D planes cutting 3-D spherical particles and have values of $\omega_r = 0.82$ and $\omega_q = 0.75$, and where $S = \mu b^2/2$ denotes the line tension, with μ, the shear modulus.

The Orowan equation describes bypassing of particles by the looping mechanism:

$$\tau_p^{Orowan} = \frac{2S}{b\omega_L\langle R\rangle} \tag{21}$$

with $\omega_L = \sqrt{\pi\omega_q/\phi} - 2\omega_r$.

In the case of a square lattice, the maximum force, F_0 , of a particle and the minimum inter-particle distance, λ_{E-E}^{min}, are employed to determine a theoretical peak strengthening:

$$\tau_p^{Square\ Lattice} = \frac{F_0}{b\lambda_{E-E}^{min}} = \frac{2\omega_r}{\sqrt{\pi\omega_q/\phi}}\frac{\gamma_{APB}}{b} \tag{22}$$

with $F_0 = 2\gamma_{APB}\omega_r\langle R\rangle$.

For alloys in the under-aged condition where the shearing mechanism is dominant, the strengthening increment is:

$$\tau_p^{underaged} = \frac{\gamma_{APB}}{2b}\left\{\left(\frac{4\omega_r^3}{\pi\omega_q}\right)^{\frac{1}{2}}\left[\frac{\gamma_{APB}\langle R\rangle\phi}{S}\right]^{\frac{1}{2}} - \alpha\phi\right\} \tag{23}$$

and for alloys with high volume fractions of particles:

$$\tau_p^{HVf} = \frac{\gamma_{APB}}{2b}\{u - \alpha\phi\} \tag{24}$$

where $u = \frac{-B+\left(\frac{B^2}{3}+4B\right)^{1/2}}{2\left(1-\frac{B}{6}\right)}$, and $B = \frac{3\pi^2\gamma_{APB}\langle R\rangle\phi}{32S}$.

Finally, for shearing of particles by the closely-coupled dislocation, where two dislocations reside in the same particle, the following equation was derived:

$$\tau_p^{SP} = 0.69\left(\frac{\gamma_{APB} p\phi S}{b^2\langle R\rangle}\right)^{\frac{1}{2}} \tag{25}$$

where p is a fitting parameter equal to unity.

10.3 Results

10.3.1 Precipitate-size effect on strengthening in single and super dislocations

Figures 40(a) and (b) show three dislocation configurations for a single screw dislocation having glided partially through obstacle fields with various average particle radii, <R> = 10 and 62 nm, at a constant volume fraction, ϕ = 13%. The dislocation, at the start of the simulation, is a straight line. As the dislocation moves and encounters precipitates, it bows between them before shearing through them or bypassing them by the Orowan mechanism and leaving a dislocation loop. In some cases, a combination of both mechanisms operates for the same field of precipitates. The dislocation advances in some regions farther than in others because the local distribution of precipitates is more or less efficient at blocking the dislocation, resulting in a highly-sinuous dislocation line. There are two regimes that emerge from these simulations, as illustrated for screw dislocations in Figures 40(a) and (b). Regime 1 is observed when the dislocation interacts with a field of small precipitates, which are sheared by the dislocation [Figure 40(a), <R> = 10 nm]. Regime 2 occurs when the precipitates are relatively large so that the dislocation bypasses them all via the Orowan looping mechanism with each bypassed precipitate surrounded by a dislocation loops [Figure 40(b), <R> = 62 nm]. Closely-clustered groups of precipitates sometimes act as a single large obstacle around which the dislocation forms a single loop by the Orowan mechanism. Simulations using edge dislocations exhibit similar configurations and behavior as screw dislocations and are not presented here.

Super-dislocations, consisting of a pair of leading and trailing dislocations, were simulated with both edge and screw configurations. Again, two regimes are observed, as illustrated for a pair of screw dislocations. Super-dislocations bypass the obstacles through cooperative shearing with the repulsive forces from the trailing dislocation on the leading dislocation assisting in propelling the leading dislocation through the precipitate field. Due to this cooperative shearing process, a

lower external stress is required to bypass the precipitate field, as compared to the single-dislocation case and, thus super-dislocation simulations consistently predict a lower $\Delta\tau_p^{sim}$ than their single-dislocation counterparts for the same combination of precipitate radii and volume fractions. Once the leading dislocation shears through a precipitate, it creates an antiphase boundary in the precipitates left between the two dislocations, which allows the trailing dislocation to easily shear through the same precipitate as it restores order. As <R> increases (as long as the shearing is the dominant bypass method), a greater external stress is needed for the leading dislocation to shear through the precipitates. This increased τ_{ext} also acts on the trailing dislocation, forcing it in a closer proximity to the pinned leading dislocation, despite the repulsion force between the two types of dislocations. Regime 2 (Orowan bowing) becomes active when the dislocations interact with large precipitates. In Figure 40(c) (<R> = 62 nm), while τ_{ext} is still sufficiently large to force the dislocation pair into a close proximity, <R> has increased to the point where it is easier for the leading dislocation to loop around individual or clusters of precipitates rather than shear them in regions of relatively-low precipitate concentrations. In this case, the trailing dislocation encounters the remaining Orowan loops around the precipitates, which create a repulsive force. When the externally-applied load is sufficiently high, the Orowan loops are observed to collapse and annihilate, creating an APB by shearing the precipitates, and subsequently allowing the trailing dislocation to move through the same precipitates and restore order by shearing them. It is important to note that by modelling the super-dislocation propagating through fields of high ϕ and high <R> precipitates, strongly-coupled dislocation pairs have been shown to shear through a precipitate nearly simultaneously, as seen in Figure 40(c).

10.3.2 Effect of dislocation type (single and super-dislocations) on strengthening

Figure 41 displays the strengthening increment, $\Delta\tau_p^{sim}$, due to a constant volume fraction (ϕ = 13%) of NiAl precipitates, as a function of average radii (<R> = 5 - 75 nm) for the four cases of single and super-dislocations of both edge and screw types. Figure 41 shows that the edge and screw results are in close agreement with one another for both the single and super-dislocation cases, despite the fact that the dislocation paths through the fields are markedly different. However, both simulations for a single dislocation yield a much higher $\Delta\tau_p^{sim}$ than the corresponding super-dislocation simulations, for <R> up to ~ 50 nm beyond which the single and super-dislocation results are quite similar. The lower value of $\Delta\tau_p^{sim}$ for the super-dislocation case is due to the

cooperative shearing that occurs when the repulsive force of the trailing dislocation assists the leading dislocation in shearing the precipitates. This phenomenon is predominant at small average precipitate radii, where obstacles are mostly bypassed by the shearing mechanism, as opposed to being bypassed by Orowan looping, which dominates at larger radii, typically above ~ 20 nm.

10.3.3 Effect of volume fraction on strengthening

Simulations were carried out for super-dislocations of both edge and screw character, and plots of $\Delta\tau_p$ vs. <R> for <R> ranging from 1 to 75 nm and for three volume fractions (ϕ=10, 13, and 20 %) are shown in Figure 42. The strengthening for screw dislocations is consistently lower than for edge dislocations with a given <R> and the ratio of $\frac{\Delta\tau_p^{Edge}}{\Delta\tau_p^{Screw}}$ of 1.1 - 1.4 (ϕ = 10%), 1.1 - 1.3 (ϕ = 13%), and 1.2 - 1.5 (ϕ = 20%). We expect the disparity between screw and edge dislocations to be due to strong pair-coupling zones (SPCZs). These SPCZs are regions where the leading and trailing dislocations are forced into very close proximity to one another, increasing the repulsion force felt by the two dislocations so that the leading dislocation is helped in its bypass of the particles. The phenomenon has been shown to occur more readily in screw than edge dislocation pairs, thus reducing the CRSS. As seen in Figure 42, $\Delta\tau_p$ initially increases with increasing radii, followed by a short plateau at the peak, τ_p^{sim}, for <R> ~ 10 - 20 nm and a subsequent decrease in $\Delta\tau_p$ for a larger average radius. As reported by Bocchini *et al.* for Ni-based superalloys strengthened by γ′ ($L1_2$) precipitates with <R> between 1 - 110 nm and ϕ = 45%, the decrease in τ_p results from the formation of an increased number of strong pair-coupling zones as the resistance to the deformation of individual precipitates increases with size. The transition from a positive to a negative slope of $\Delta\tau_p$ for small radii versus larger radii is a result of a switch in the bypass method that dominates dislocation propagation and is explicitly observed to occur in the DD simulations. In addition, Figure 42 shows that in general, the $\Delta\tau_p$ increases with increasing the volume fraction for both super-edge and super-screw dislocations due to a decrease in the inter-precipitate distance, λ_{E-E}.

10.3.4 Overall precipitate strengthening at a constant volume fraction

Simulated results, for various radii at a constant volume fraction of 13%, are compared to the analytical equations given in Eqs. (20)-(25) and in Figure 43. It is apparent that Eqs. (20) and

(21), which correspond to the Friedel and Orowan closed-form solutions for the shearing and Orowan mechanisms, respectively, and most closely follow the results for the single-dislocation simulations for under-aged (a region of low <R> below the peak $\Delta\tau_p$) and over-aged (a region of high <R>) regions, respectively. In the under-aged region, there is only rough agreement between the analytical solutions of the simulated $\Delta\tau_p$ values. However, for both the single and super-dislocation cases, the closed-form solutions fail to accurately capture the trajectory of the simulated results. Similar discrepancies were observed in previous studies and were attributed to the influence of the periodic boundary condition used in the model, which is not accounted for in the analytical models that also use a regular lattice-like distribution of precipitates not representative of the true distribution of precipitates.

In the over-aged region, the closed-form solution associated with the Orowan bypass mechanism [Eq. (4)] accurately captures the trend of the simulated results with excellent agreement at precipitate radii greater than 30 nm. The higher level of agreement between analytical solutions and simulated results in the over-aged region, as opposed to the under-aged region, is expected as Mohles *et al* [71-73]. have shown that the effects of the periodic boundary condition has its greatest impact at smaller radii. As reported in Nembach [75], the constant value of $\Delta\tau_p^{Square\ Lattice}$ in Eq. (22) is derived from the maximum force of $F_0 = 2\gamma\omega_r r$ of the average obstacle and the minimum distance of L_{min}, between the particles if they were arranged in a square lattice. Since the inputs are independent of the line tension or energy and are based on the elastic interaction between dislocations, Eq. 5 serves as an upper limit for $\Delta\tau_p$ and is in good agreement with the highest simulated value.

In the case of super-dislocation pairs, both Eqs. (23) and (24) are plotted in Figure 43 to compare with the simulated results for small particle radii (<R> < 15 nm). While the analytical solution, which models alloys with high volume fractions (Eq. 7), best matches the simulated data, Eq. (25) is more appropriate due to the relatively-low volume fraction (< 50%) simulated in this study to model under-aged super-dislocation results. In any case, neither equation accurately matches the under-aged or peak-aged behavior of the simulated results, with Eq. (24) unable to capture the trend of the data, and Eq. 6 over-predicting the simulation results. The inability of the analytical solutions to accurately model the behavior of both types of super-dislocations in the peak-strengthening condition has been reported for other systems as well. This discrepancy is most likely due to numerous simplifying assumptions used when formulating the analytical solutions,

such as a static dislocation geometry as well as the effect of the periodic-boundary condition mentioned in the previous paragraph. In the over-aged region, Eq. 8, which models closely-coupled dislocations shearing the same particle, accurately describes the simulated results for super-dislocation pairs at large radii (<R> > 30 nm) even though the simulations show the evidence of Orowan looping as well as closely-coupled shearing.

10.4 Conclusion

The 2D dislocation dynamics (DD) simulations were performed to model the yield stress of a ferritic matrix with B2-NiAl precipitate volume fractions ranging from 10 to 20% and average radii, <R>, between 5 and 75 nm, representative of the ferritic superalloys. The simulations allow for a study of dislocation-precipitate interactions, which provide a prediction for the strengthening increment due to precipitation, τ_p^{sim}. The following observations were made:

- Three distinct regimes were identified for single dislocations gliding through a field of precipitates: (a) shearing of small precipitates, (b) combined shearing/looping of intermediate size precipitates, and (c) looping around large precipitates. The relative strengthening of these regimes follows (b) > (a) > (c).

- Three distinct regimes were identified for super-dislocations (pair of dislocations gliding together): (a) weakly-coupled with leading dislocation-shearing precipitates, (b) moderately-coupled with leading and trailing dislocations simultaneously shearing precipitates, and (c) strongly-coupled with the leading dislocation looping around precipitates and leading and trailing dislocations in a close proximity to one another. The relative strengthening of these regimes typically follows (b) > (a) > (c).

- Super-dislocations can more easily bypass obstacles than single dislocations, likely due to the strong repulsive inter-dislocation force, which occurs when two dislocations are forced in a close proximity to one another, which assists the leading dislocation through an obstacle field. Meanwhile, the trailing dislocation shears more easily the precipitates because it eliminates the anti-phase boundary created by the leading dislocation.
- Super-dislocations consistently predict lower strengthening contributions than single dislocations. However, there is a much smaller difference between the edge and screw

dislocation results, with a ratio of $\frac{\Delta\tau_p^{Edge}}{\Delta\tau_p^{Screw}}$ ranging from 1.1 - 1.5 over ϕ = 10, 13, and 20% for super-dislocations.

Closed-form analytical solutions for yield stresses capture the magnitude but not the evolution of the yield stress from DD-simulated results for the small <R> values in the underaged conditions; both the magnitude and evolution are captured for large <R> values, corresponding to the overaged condition, but they do not accurately depict the peak-aging τ_p^{sim} behavior.

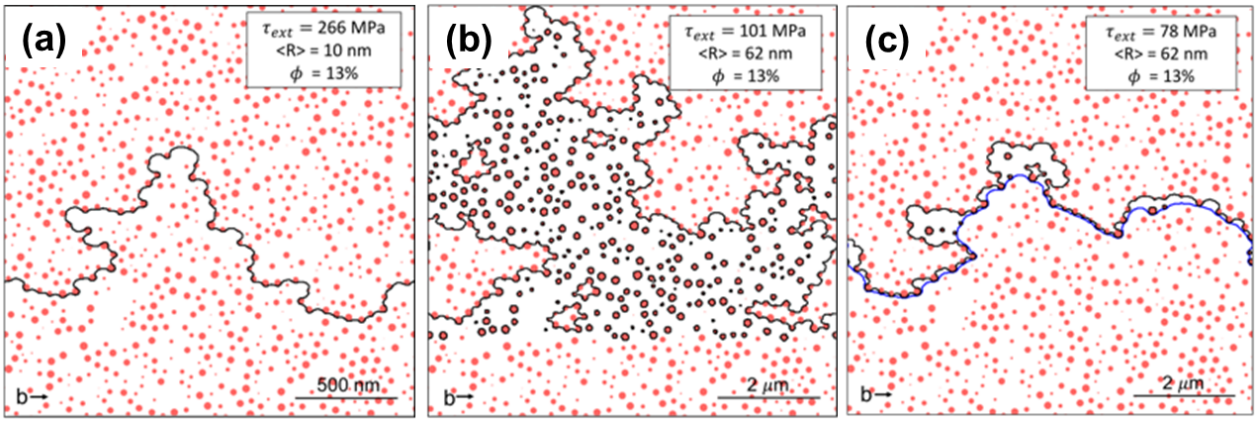

Figure 40. Two-dientional (2-D) dislocation-dynamics (DD)-simulation examples of (a) a single screw-type dislocation shearing small precipitates, (b) looping around large precipitates and bypassing combined shearing/looping intermediate-size precipitate, and (c) moderately-coupled screw-type dislocation pairs moving through fields of precipitates with an APB energy of 200 mJm^{-2}, typical of β´ (B2)-precipitates in Fe-based superalloys. The dislocation is moving in the direction perpendicular to the Burgers vector (b), indicating a screw-type dislocation. The maximum applied shear stress (τ_{ext}), average precipitate radius (<R>), and volume fraction (ϕ) are listed in the insets.

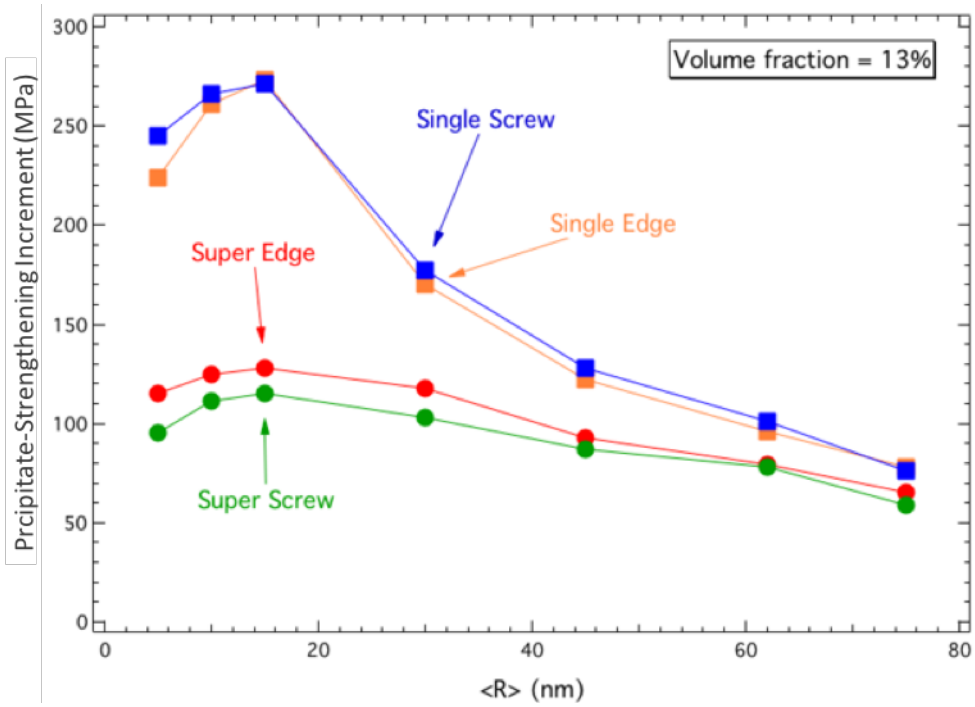

Figure 41. Plot of strengthening increment, $\boldsymbol{\tau_p}$, in Fe alloys with β′ (B2) precipitates with an APB energy of 200 mJ m^{-2} as a function of precipitate average radius for DD simulations of single and super-dislocations of both edge and screw-types with a volume fraction of ϕ = 13 %.

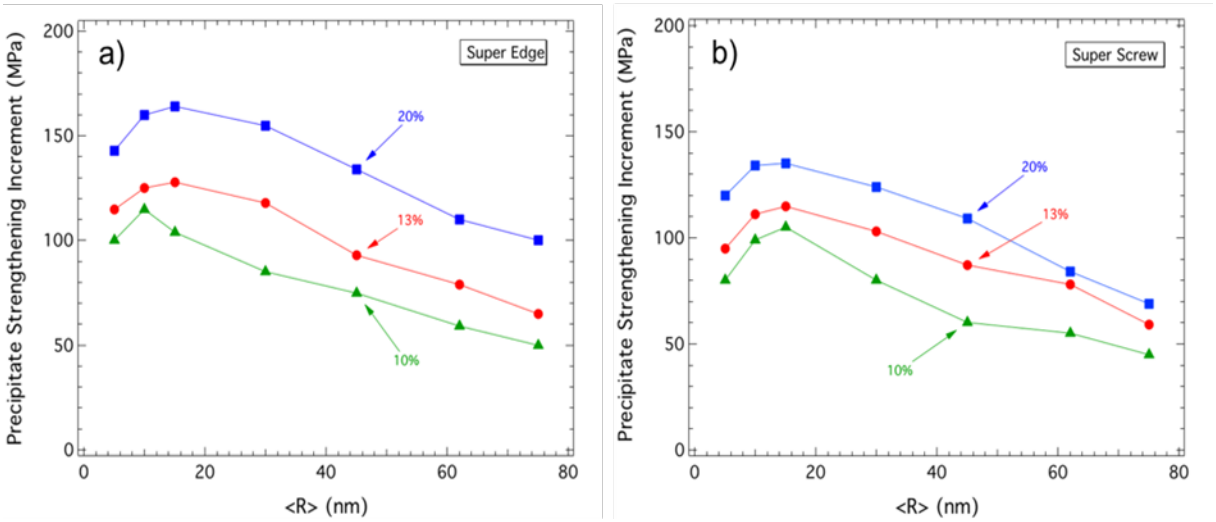

Figure 42. Plot of strengthening increment, $\boldsymbol{\tau_p}$, in Fe alloys with β′ (B2) precipitates with an APB energy of 200 mJm-2 as a function of precipitate average radius for 2D DD simulations of (a) super-edge and (b) super-screw dislocations for volume fractions of ϕ = 10, 13, and 20 %.

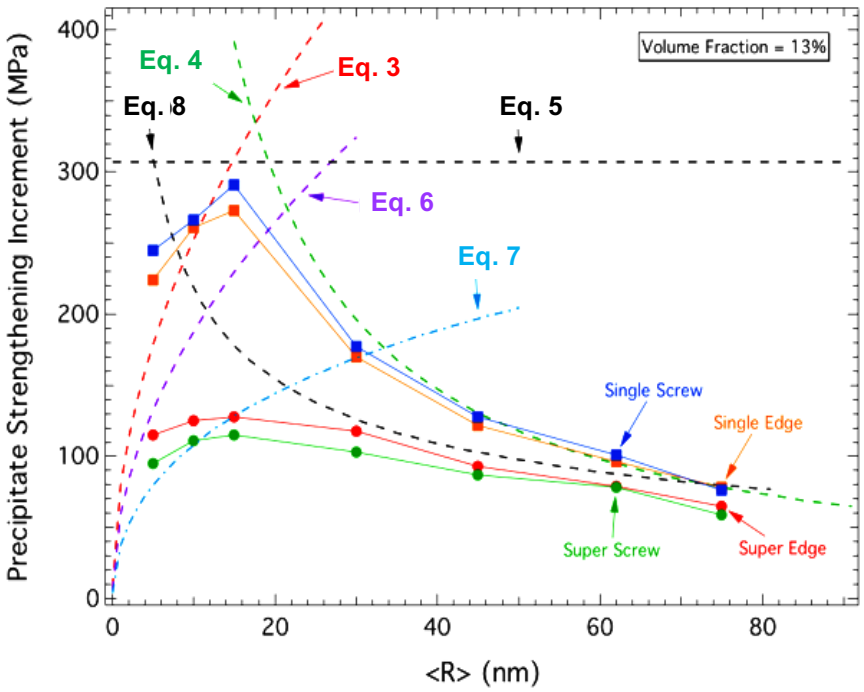

Figure 43. Plot of strengthening increment, $\boldsymbol{\tau_p}$, in Fe alloys with β′ (B2) precipitates with an APB energy of 200 mJ m^{-2} as a function of precipitate average radius with a volume fraction of $\phi = 13\%$ for DD simulations (solid lines with symbols) of super-edge and super-screw dislocations, compared to analytical models (dotted lines).

Executive Summary

The purpose of the present project is to develope ferritic superalloys with even higher creep resistance, based on the concept of the hierarchical-precipitate-strengthened ferritic alloy (HPSFA). Therefore, we've proposed to replace Ti with Hf and Zr, with their larger atomic size, to create higher lattice strain that is able to further enhance the effect of precipitation strengthening. However, in the present project, we've found out that unlike the FBB8 + 2% Ti alloy, the additions of Hf and Zr do not form the $L2_1$ phase within the alloy. Instead, these Hf and Zr elements form Laves phases and deposit along the grain boundaries or segregate as a large bulk within grains. These Laves phases, due to their size and distribution, cannot bring any obvious enhancement on the creep resistance to the original FBB8. In the first two years of this project, we've emphasized more on the research of the microstructures of FBB8 + 2% Hf and FBB8 + 2% Zr alloys, and had discovered the above phenomena. In the last year of the project, we've focused on the FBB8 + Ti series alloys, in order to optimize the creep resistance. The previous research found that with hierarchical structure precipitates, the creep resistance can be even higher than alloys with single phase precipitates. However, we did not know what the ideal ratio for the two phases within a hierarchical structure precipitate is, and what the ideal Ti content within the alloy is. Now we've found that the alloy with the optimized creep resistance is the FBB8 + 3.5% Ti, with the $L2_1$/B2 ratio of 4. Alloys with even higher Ti contents covert all the B2 phase into the $L2_1$ phase, lose the hierarchical structure feature, and creep resistances are reduced.

For the first-principle calculations, single crystal elastic constants (C_{ij}), congruent ordering energies, and coherent interfacial energies were calculated for BCC-Fe, B2-NiAl, and $L2_1$-Ni_2TiAl phases. The calculated C_{ij}s are compared with the available experimental data or other calculation results, and the orientation dependence of Young's modulus is also calculated, based on the calculated C_{ij}s. To establish reliability and accuracy of computational results, we have calculated C_{ij}s of relevant pure elements and compared them with experimental data at low temperatures, showing the agreement expected within the expected level of accuracy. For congruent ordering energies, relevant ordering energies are obtained from first principles using the Vienna ab-initio simulation package (VASP) and Alloy Theoretic Automated Tookit (ATAT) codes. Computed results are important in modeling the phase stability (using the Calculation of Phase Diagrams, CALPHAD technique) and understanding the microstructure dynamics, phase-transformation kinetics, and microstructure evolution in multi-component alloys, which is not obtained in

conventional experiments. For coherent interfacial energies, since there are three hetero-phase interfaces in a hierarchical microstructure involving the disordered matrix (α-Fe or A2) and ordered precipitates NiAl (B2), and Ni_2TiAl ($L2_1$), calculations are done with the sharp-interface approximation, with the consideration of {100}, {110}, and {111} interface habits. We find that the Fe/B2 interfacial energies are much greater than B2/$L2_1$.

For the dislocation-dynamics calculations, two-dimensional (2D) dislocation-dynamics (DD) simulations are performed, in order to determine the increase in the yield stress due to ordered B2-NiAl nanoprecipitates within a ferritic matrix. Parametric studies investigate three precipitate volume fractions (10, 13, and 20 %) and various radii (from 1 to 75 nm), associated with the yield-stress mechanism based on precipitate bypassing and/or shearing by single and super-dislocations of edge or screw character. Yield stresses from DD simulations for various precipitate radii with a volume fraction of 13% (corresponding to various stages of aging) are then compared to a variety of analytical models for strengthening by ordered precipitates. The calculation majorly focuses on understanding concerning the interaction of the dislocations and precipitates, and the results show that (1) super-dislocations can more easily bypass precipitates than single dislocations, (2) intermediate size precipitates have the best strengthening effect for single dislocations, (3) moderately-coupled with leading and trailing dislocations simultaneously shearing precipitates has the best strengthening effect for super-dislocations, and (4) there's no large differences between edge and screw dislocations.

References

[1] C.H. Liebscher, V. Radmilovic, U. Dahmen, M. Asta, G. Ghosh. On the Formation of Hierarchically Structured L21-Ni2TiAl type Precipitates in a Ferritic Alloy. *J. Mater Sci*, 48 (2013), 2067-2075.

[2] C.H. Liebscher, V.R. Radmolovic, U. Dahmen, N.Q. Vo, D.C. Dunand, M. Asta, G. Ghosh. A hierarchical microstructure due to chemical ordering in the bcc lattice: Early stages of formation in ferritic Fe-Al-Cr-Ni-Ti alloy. *Acta Mater.*, 92 (2015), 220-232.

[3] K. Zeng, R. Schmid-Fetzer, B. Huneau, P. Rogl, J. Bauer. The ternary system Al-Ni-Ti Part II: Thermodynamic assessment and experimental investigation of polythermal phase equilibria. *Intermetallics*, 7 (1999), 1347.

[4] G. Kresse, J. Hafner. Ab initio molecular-dynamics simulation of the liquid-metal–amorphous-semiconductor transition in germanium. *Phys Rev B*, 49 (1994), 14251.

[5] G. Kresse and J. Furthmüller, 54, 11169 (1996). Efficient iterative schemes for ab initio total-energy calculations using a plane-wave basis set. *Phys Rev B*, 54 (1996), 11169.

[6] G. Kresse, J. Furthmüller. Efficiency of ab-initio total energy calculations for metals and semiconductors using a plane-wave basis set. *Comp Mater Sci*, 6 (1996), 15.

[7] P.E. Blöchl. Projector augmented-wave method. *Phys Rev B*, 50 (1994), 17953.

[8] M. Marsman, G. Kresse. The relaxed core PAW method. *J Chem Phys*, 125 (2006), 104101.

[9] E. Wimmer, H. Krakauer, M. Weinert, A.J. Freeman. Full-potential self-consistent linearized-augmented-plane-wave method for calculating the electronic structure of molecules and surfaces: O2 molecule. *Phys Rev B*, 24 (1981), 864.

[10] J.P. Perdew. *Electronic structure of solids*. Akademie Verlag., Berlin, 1991.

[11] H.J. Monkhorst, J.D. Pack. Special points for Brillouin-zone integrations. *Phys Rev B*, 13 (1976), 5188.

[12] M. Methfessel, A.T. Paxton. High-precision sampling for Brillouin-zone integration in metals. *Phys Rev B*, 40 (1989), 3616.

[13] A. van de Walle, G. Ceder. Automating first-principles phase diagram calculations. *J. Phase Equil*, 23 (2002), 348.

[14] A. van de Walle, M. Asta, G. Ceder. The Alloy Theoretic Automated Toolkit: A User Guide. *Calphad*, 26 (2002), 539.

[15] A. van de Walle. Multicomponent multisublattice alloys, nonconfigurational entropy and other additions to the Alloy Theoretic Automated Toolkit. *Calphad*, 33 (2009), 266.

[16] A. Zunger, S.H. Wei, L. G. Ferreira, J.E. Bernard. Special quasirandom structures. *Phys. Rev. Lett.*, 65 (353), 1990.

[17] G. Ghosh, A. van de Walle, M. Asta. First-principles calculations of the structural and thermodynamic properties of bcc, fcc and hcp solid solutions in the Al–TM (TM = Ti, Zr and Hf) systems: A comparison of cluster expansion and supercell methods. *Acta Mater.*, 56 (2008), 3202.

[18] K. J. Lee, P. Nash. The Al-Ni-Ti system. *J. Phase Equilibria*, 12 (1991), 551.

[19] O. Kubaschewski, The Heats of Formation in the system Aluminium+Nickel+Titanium. *Trans. Faraday Soc.*, 54 (1958), 814.

[20] R. Hu, P. Nash, Q. Chen. Enthalpy of Formation in the Al-Ni-Ti System. *J. Phase Equilibria and Diffusion*, 30 (2009), 559.

[21] L. Kaufman, H. Nesor. Calculation of superalloy phase diagrams" Part II. *Metal. Trans.*, 5 (1974), 1623.

[22] P. Nash, W. W. Liang Metall. Trans A, 16A, 319 (1985). Phase equilibria in the Ni-Al-Ti system at 1173K. *Metall. Trans A*, 16A (1985), 319.

[23] P.B. Budberg. Aluminium-Nickel-Titanium. In G. Effenberg, S. Illyenko, ed., *Landolt-Börnstein Numerical Data and Functional Relationship in Science and Technology, New Series*. Springer-Verlag, Berlin/Heidelberg, 2005.

[24] J.C. Schuster, Z. Pan, S. Liu, F. Weitzner, Y. Du. On the constitution of the ternary system Al-Ni-Ti. *Intermetallics*, 15 (2007), 1257.

[25] W. Voigt. *Lehrbuch der Kristallphysik*. B.G. Teubner, Leipzig, 1928.

[26] A. Reuss. Berechnung der Fließgrenze von Mischkristallen auf Grund der Plastizita¨tsbedingung fu¨r Einkristalle. *Math Phys*, 9 (1929), 49-58.

[27] R. Hill. The elastic behaviour of a crystalline aggregate. *Proc. Phys Soc.*, 65A, 5 (1952), 349-354.

[28] D.H. Chung. Elastic moduli of single-crystal and poly- crystalline MgO. *Phil. Mag.*, 8 (1963), 833-841.

[29] M. Kumazawa. The elastic constant of polycrystalline rock and non-elastic behaviour inherent to them. *J. geophys. Res.*, 74 (1969), 5311-5320.

[30] M.M. Shukla, N.T. Padial. A calculation of the Debye characteristic tempera- ture of cubic crystals. *Revista Brasileira de Física*, 3 (1973), 39-45.

[31] Z. Hashin. The elastic moduli of heterogeneous materials. *J. Appl Mech*, 29 (1962), 143-150.

[32] Z. Hashin, S. Shtrikman. On some variational principles in anisotropic and nonhomogeneous elasticity. *J. Mech. Phys. Solids*, 10 (1962), 335-342.

[33] Z. Hashin, S. Shtrikman. A variational approach to the theory of the elastic behaviour of multiphase materials. *J. Mech. Phys. Solids*, 11 (1963), 127-140.

[34] J.A. Rayne, B.S. Chandrasekhar. Elastic Constants of Iron from 4.2 to 300°K. *Phys. Rev.*, 122 (1961), 1714.

[35] G. Simmons, H. Wang. *Single Crystal Elastic Constants and Calculated Aggregate Properties: A Handbook*. The MIT Press, MA, 1971.

[36] D.B. Miracle. Overview No. 104 The physical and mechanical properties of NiAl. *Acta Metallurgica et Materialia*, 41 (1993), 649-684.

[37] R.D. Noebe, R.R. Bowman, M.V. Nathal Ch 7, (1996). *Physical Metallurgy and Processing of Intermetallic Compounds*. Chapman & Hall, 1996.

[38] W. Ostwald. *Lehrbuch der Allgemeinen Chemie*. W. Engelmann, Leipzig, 1896.

[39] C. Woodward, A. van de Walle, M. Asta, D.R. Trinkle. *Acta Mater.* , 75 (2014), 60.

[40] G. Song, Z. Sun, L. Li, X. Xu, M. Rawlings, C.H. Liebscher, B. Clausen, J. Poplawsky, D.N. Leonard, S. Huang, Z. Teng, C.T. Liu, M.D. Asta, Y. Gao, D.C. Dunand, G. Ghosh, M. Chen, M.E. Fine, P.K. Liaw. Ferritic alloys with extreme creep resistance via coherent hierarchical precipitates. *Scientific Report*, 5 (2015), 16327.

[41] M.J.S. Rawlings, C.H. Liebscher, M. Asta, D.C. Dunand. Effect of titanium additions upon microstructure and properties of precipitation-strengthened Fe-Ni-Al-Cr ferritic alloys. *Acta Materialia*, 128 (2017), 103-112.

[42] J. Jung, G. Ghosh, D. Isheim, G.B. Olson. Precipitation of heusler phase (Ni2TiAl) from B2-TiNi in Ni-Ti-Al and Ni-Ti-Al-X (X=Hf, Zr) alloys. *Metall and Mat Trans A*, 34 (2003), 1221-1235.

[43] Davis, J. R. Nickel, Cobalt, and Their Alloys. *ASM International* (2000), 304.

[44] P.A. Burr, S.T. Murphy, S.C. Lumley, M.R. Wenman, R.W. Grimes. Hydrogen accommodation in Zr second phase particles: Implications for H pick-up and hydriding of Zircaloy-2 and Zircaloy-4. *Corrosion Science*, 69 (2013), 1-4.

[45] M.A.M. Bourke, D.C. Dunand, E. Ustundag. SMARTS – A Spectrometer for Strain Measurement in Engineering Materials. *Applied Physics A*, 74 (2002), 1707-1709.

[46] R. Von. Dreele. Quantitative texture analysis by Rietveld refinement. *J. Appl. Crystallogr.*, 30 (1997), 517-525.

[47] A.C. Larson, R.B. Von Dreele. *General Structure Analysis System (GSAS)*. Los Alamos National Laboratory, 1994.

[48] P.R. Strutt, R.S. Polvani, J.C. Ingram. Creep behavior of the heusler type structure alloy Ni2AlTi. *Metallurgical and Materials Transactions A*, 7A (1976), 23-31.

[49] H. Bei, E.P. George, D.W. Brown, G.M. Pharr, H. Choo, W.D. Porter, M.A.M. Bourke. Thermal-expansion behavior of a directionally solidified NiAl-Mo composite investigated by neutron diffraction and dilatometry. *J. Appl. Phys.*, 97 (2005), 123503.

[50] Z.K. Teng, G. Ghosh, M.K. Miller, S. Huang, B. Clausen, D.W. Brown, P.K. Liaw. Neutron-diffraction study and modeling of the lattice parameters of a NiAl-precipitate-strengthened Fe-based alloy. *Acta Mater.*, 60 (2012), 5362-5369.

[51] Property of solids. In D.R. Lide, W.M. Haynes, ed., *CRC handbook of chemistry and physics*. 2011.

[52] X. Yan, A. Grytsiv, P. Rogl, V. Pomjakushin, M. Palm. The Heusler phase Ti25(Fe50 − xNix)Al25 ($0 \leq x \leq 50$); Structure and Constitution. *J. Phs. Eqil. and Diff.*, 29 (2008), 500-508.

[53] H.J. Stone, T.M. Holden, R.C. Reed. Determination of the plane specific elastic constants of waspaloy using neutron diffraction. *Scr. Mater.*, 40 (1999), 353-358.

[54] V.F. Sears. Neutron scattering lengths and cross sections. *Neutron News*, 3 (1992), 26-37.

[55] O. Kubaschewski. *Iron-Binary Phase Diagrams*. Springer-Verlag, Berlin/Heidelberg, 1982.

[56] M.V. Nathal, R.A. MacKay, R.G. Garlick. Temperature Dependence of y-γ Lattice Mismatch in Nickel-Base Superalloys. *Materials Science and Engineering*, 75 (1985), 195-205.

[57] B.S. Mitchell. *An Introduction to Materials Engineering and Science for Chemical and Materials Engineers*. John Wiley, Hoboken, 2004.

[58] M.E. Kassner. *Fundamentals of creep in metals and alloys*. Elsevier, 2009.

[59] A.K. Mukherjee, J.E. Bird, J.E. Dorn. Experimental correlations for high-temperature creep. *ASM transactions quarterly*, 62 (1969), 155.

[60] G. Song, Z.Q. Sun, B. Clausen, P.K. Liaw. Microstructural characteristics of a Ni_2TiAl-precipitate-strengthened ferritic alloy. *Journal of alloys and compounds*, 693 (2017), 921-928.

[61] J. Weertman. Discussion of: "An experimental relation defining the stress dependence of minimun creep rate in metals". *Transactions of the American Institute of Mining, Metallurgical and Petroleum Engineers*, 227 (1963), 1475-1476.

[62] Z. Sun, C.H. Liebscher, S. Huang, Z. Teng, G. Song, G. Wang, M. Asta, M. Rawlings, M.E. Fine, P.K. Liaw. New design aspects of creep-resistant NiAl-strengthened ferritic alloys. *Scripta Materialia*, 68 (2013), 384-388.

[63] F. Phillips. The slow stretch in india rubber, glass and metal wire when subjected to a constant pull. *Philos Mag*, 19 (1903), 491-511.

[64] F. Garofalo. *Fundamentals of Creep and Creep-Rupture in Metals*. McMillan, New York, 1965.

[65] R.K. Penny, D.L. Marriott. *Design for Creep*. Springer, 1995.

[66] J. Dean, A. Bradbury, G. Aldrich-Smith, T.W. Clyne. A procedure for extracting primary and secondary creep parameters from nanoindentation data. *Mechanics of Materials*, 65 (2013), 124-134.

[67] A. Graham, K.F.A. Walles. Relations between long and short time properties of commercial alloys. *JISI*, 179 (1955), 105-120.

[68] P.G. McVetty. Factors affecting the choice of working stresses for high temperature service. *Trans ASME*, 55 (1933), 99-109.

[69] J. B. Conway, M. J. Mullikin. An evaluation of various first stage creep equations. In *Proceedings of AIME conference* (Detroit 1962).

[70] Z. Sun, G. Song, T.A. Sisneros, B. Clausen, C. Pu, L. Li, Y. Gao, P.K. Liaw. Load partitioning between the bcc-iron matrix and NiAl-type precipitates in a ferritic alloy on multiple length scales. *Scientific Reports*, 6 (2016), 23137.

[71] V. Mohles. Computer simulations of particle strengthening : the effects of dislocation dissociation on lattice mismatch strengthening. *Materials Science and Engineering: A*, 321 (2001), 206-210.

[72] V. Mohles. Computer simulations of the glide of dissociated dislocations in lattice mismatch strengthened materials. *Materials Science and Engineering: A*, 324 (2002), 190-195.

[73] V. Mohles, B. Fruhstorfer. Computer simulations of Orowan process controlled dislocation glide in particle arrangements of various randomness. *Acta Mater.*, 50 (2002), 2503-2516.

[74] G. Samsonov. *Handbook of the Physicochemical Properties of the Elements: Mechanical Properties of the Elements*. Springer US, 1968.

[75] E. Nembach. *Particle Strengthening of Metals and Alloys*. New York: Wiley, 1996.

[76] K.E. Yoon, R.D. Noebe, O.C. Hellman, D.N. Seidman. Dependence of interfacial excess on the threshold value of the isoconcentration surface (2004), 594-597.

[77] E. Arzt, J. Rosler. The Kinetics of Dislocation Climb over Hard Particles .2. Effects of an attractive particle dislocation interaction, *Acta Metallurgica* 36 (1988) 1053-1060.

[78] P.W. Voorhees, G.B. McFadden, W.C. Johnson. On the morphological development of 2nd-phase particles in elastically-stressed solids, *Acta Metall Mater* 40 (1992) 2979-2992.

[79] https://www.brown.edu/Departments/Engineering/Labs/avdw/atat/

[80] http://www.calphad.org

[81] C.J.B. Clews, E.N. Maslen, H.M. Rietveld, T.M. Sabine. X-Ray and Neutron Diffraction Examination of p-Diphenylbenzene, *Nature* 192 (1961) 154-155.

[82] https://www.ncnr.nist.gov/xtal/software/gsas.html

Publications, Presentations, and Awards

Publications

1. Z. K. Teng, M. K. Miller, G. Ghosh, C. T. Liu, S. Huang, K. F. Russel, M. E. Fine, and P. K. Liaw. Characterization of nanoscale NiAl-type precipitates in a ferritic steel by electron microscopy and atom probe tomography, *Scripta Materialia* 63 (2010) 61-64.
2. S. Huang, D. L. Worthington, M. Asta, V. Ozolins, G. Ghosh, and P. K. Liaw. Calculation of impurity diffusivities in α-Fe using first-principles methods, *Acta Materialia* 58 (2010) 1982-1993.
3. S. Huang, B. Clausen, D. Brown, Z. K. Teng, Y. F. Gao, and P. K. Liaw. In situ neutron-diffraction studies on the creep behavior of a ferritic superalloy, *Metallurgical and Materials Transactions A* 43 (2012) 1497-1508.
4. Z. K. Teng, F. Zhang, M. K. Miller, C. T. Liu, S. Huang, Y. T. Chou, R. H. Tien, Y. A. Chang, and P. K. Liaw. Thermodynamic modeling and experimental validation of the Fe-Al-Ni-Cr-Mo alloy system, *Materials Letters* 71 (2012) 36-40.
5. Z. K. Teng, G. Ghosh, M. K. Miller, S. Huang, B. Clausen, D. W. Brown, and P. K. Liaw. Neutron-diffraction study and modeling of the lattice parameters of a NiAl-precipitate-strengthened Fe-based alloy, *Acta Materialia* 60 (2012) 5362-5369.
6. Z. K. Teng, C. T. Liu, M. K. Miller, G. Ghosh, E. A. Kenik, S. Huang, and P. K. Liaw. Room temperature ductility of NiAl-strengthened ferritic steels: Effects of precipitate microstructure, *Materials Science and Engineering A* 531 (2012) 22-27.
7. H. Ding, S. Huang, G. Ghosh, P. K. Liaw, and M. Asta. A computational study of impurity diffusivities for 5d transition metal solutes in α-Fe, *Scripta Materialia* 67 (2012) 732-735.
8. S. Huang, G. Ghosh, X. Li, J. Ilavsky, Z. K. Teng, and P. K. Liaw. Effect of Al on the NiAl-Type B2 Precipitates in Ferritic Superalloys, *Metallurgical and Materials Transactions A* 43 (2012) 3423.
9. C. H. Liebscher, V. Radmilovic, U. Dahmen, M. Asta and G. Ghosh. On the formation of hierarchically structured L21-Ni2TiAl type precipitates in a ferritic alloy, *Journal of Materials Science* 48 (2013) 2067-2075.

10. Z. Sun, C. H. Liebscher, S. Huang, Z. Teng, G. Song, G. Wang, M. Asta, M. Rawlings, M. E. Fine, and P. K. Liaw. New design aspects of creep-resistant NiAl-strengthened ferritic alloys, *Scripta Materialia* 68 (2013) 384-388.
11. H. Ding, V. I. Razumovsky, and M. Asta. Self-diffusion anomaly in ferromagnetic metals: A density-functional-theory investigation of magnetically ordered and disordered Fe and Co, *Acta Materialia* 70 (2014) 130-136.
12. S. Huang, Y. Gao, K. An, L. Zheng, W. Wu, Z. Teng, and P.K. Liaw. Deformation mechanisms in a precipitation-strengthened ferritic superalloy revealed by in situ neutron diffraction studies at elevated temperatures, *Acta Materialia* 83 (2015) 137-148.
13. Z. Sun, G. Song, J. Ilavsky, and P.K. Liaw. Duplex precipitates and their effects on the room-temperature fracture behaviour of a NiAl-strengthened ferritic alloy, *Materials Research Letters* 3 (2015) 128-134.
14. C.H. Liebscher, V.R. Radmilović, U. Dahmen, N.Q. Vo, D.C. Dunand, M. Asta, and G. Ghosh. A hierarchical microstructure due to chemical ordering in the bcc lattice: Early stages of formation in a ferritic Fe-Al-Cr-Ni-Ti alloy, *Acta Materialia* 92 (2015) 220-232.
15. G. Song, Z. Sun, L. Li, X. Xu, M. Rawlings, C.H. Liebscher, B. Clausen, J. Poplawsky, D.N. Leonard, S. Huang, Z. Teng, C.T. Liu, M.D. Asta, Y. Gao, D.C. Dunand, G. Ghosh, M. Chen, M.E. Fine, and P.K. Liaw. Ferritic alloys with extreme creep resistance via coherent hierarchical precipitates, *Scientific Reports* 5 (2015) 16327.
16. Z. Sun , G. Song , J. Ilavsky , G. Ghosh, and P.K. Liaw. Nano-sized precipitate stability and its controlling factors in a NiAl-strengthened ferritic alloy, *Scientific Report* 5 (2015) 16081.
17. Z. Sun, G. Song, T. Sisneros, B. Clausen, C. Pu, L. Li, Y. Gao, and P.K. Liaw. Load partitioning between the bcc-iron matrix and NiAl-type precipitates in a ferritic alloy on multiple length scales, *Scientific Reports* 6 (2016) 23137.
18. G. Song, Z. Sun, J. D. Poplawsky, Y. Gao, P.K. Liaw. Microstructural evolution of single Ni2TiAl or hierarchical NiAl/Ni2TiAl precipitates in Fe-Ni-Al-Cr-Ti ferritic alloys during thermal treatment for elevated-temperature applications, *Acta Materialia* 127 (2017) 1-16.

19. G. Song, Z. Sun, J. D. Poplawsky, X. Xu, M. Chen, P. K. Liaw. Primary and secondary precipitates in a hierarchical-precipitate-strengthened ferritic alloy, *Journal of Alloys and Compounds* 706 (2017) 584-588.

20. G. Song, Z. Sun, B. Clausen, P. K. Liaw. Microstructural characteristics of a Ni 2 TiAl-precipitate-strengthened ferritic alloy, *Journal of Alloys and Compounds* 693 (2017) 921-928.

21. M.J.S. Rawlings, C.H. Liebscher, M. Asta, D.C. Dunand. Effect of titanium additions upon microstructure and properties of precipitation-strengthened Fe-Ni-Al-Cr ferritic alloys, *Acta Materialia* 128 (2017) 103-112.

22. S.I. Baik, M.J.S. Rawlings, D.C. Dunand. Atom probe tomography study of Fe-Ni-Al-Cr-Ti ferritic steels with hierarchically-structured precipitates, *Acta Materialia* (In press)

23. S. I. Baik, M. J. S. Rawlings, D. C. Dunand. Effect of hafnium micro-addition on precipitate microstructure and creep properties of a Fe-Ni-Al-Cr-Ti ferritic superalloy, *Acta Materialia* (Submitted)

24. S. Y. Wang, J. Poplawsky, C. Lee, P. Chen, C. Zhang, P. K. Liaw. Partitioning of hafnium and zirconium in Fe-Ni-Al-Cr ferritic alloy systems. (In preparation)

25. S. Y. Wang, A. Ke, C. Lee, P. Chen, P. K. Liaw. In-situ neutron diffraction on FBB8 + 2% Hf and FBB8 + 2% Zr alloys. (In preparation)

26. S. Y. Wang, Y. Gao, C. Lee, P. Chen, P. K. Liaw. Modeling on advanced creep resistant Fe-Ni-Al-Cr ferritic alloys. (In preparation)

Invited Presentations

1. P. K. Liaw, C. T. Liu, M. E. Fine, G. Ghosh, M. D. Asta, M. K. Miller, S. Y. Huang, Z. K. Teng, and G. Wang, International Conference on Advanced High-Temperature and High-Strength Structural Materials (HTHSSM), Hong Kong, China, 10/04-10/08, 2009

2. P. K. Liaw, Z. Teng, S. Huang, C. T. Liu, M. E. Fine, G. Ghosh, M. D. Asta, and G. Wang, The Annual University Coal Research/Historically Black Colleges and Universities and Other Minority Institutions Conference, Pittsburgh, Pennsylvania, 06/07 – 06/08, 2011

3. P. K. Liaw, M. D. Asta, D. C. Dunand, M. E. Fine, G. Ghosh, and C. T. Liu, National Energy Technology Laboratory, Pittsburgh, Pennsylvania, 04/18, 2012
4. Z. Sun, G. Song, M. D. Asta, D. C. Dunand, M. E. Fine, G. Ghosh, and P. K. Liaw, The Annual University Coal Research/Historically Black Colleges and Universities and Other Minority Institutions Conference, Pittsburgh, Pennsylvania, 06/18-06/20, 2013
5. P. K. Liaw, QuesTek Innovations LLC, Evanston, Illinois, 06/01, 2017
6. S.Y. Wang, G. Song, S. I. Baik, G. Ghosh, D. C. Dunand and P. K. Liaw, 2018 TMS Meeting, Phoenix, Arizona, 3/11 – 3/15, 2018

Presentations

1. Z. K. Teng, F. Zhang, M. K. Miller, C. T. Liu, A. Y. Chuang, S. Y. Huang, R. H. Tien, Y. T. Chou, and P. K. Liaw. 2011 TMS Meeting, San Diego, 02/27 – 03/04.
2. S. Y. Huang, B. Clausen, D. Brown, Z. Teng, G. Ghosh, M. Fine, and P. K. Liaw, 2011 TMS Meeting, San Diego, 02/27 – 03/04.
3. S. Huang, Y. F. Gao, K. An, W. Wu, L. Zheng, M. Rawlings, D. Dunand, and P. K. Liaw, 2012 TMS Meeting, Orlando, Florida , 03/11 – 03/15.
4. C. H. Liebscher, V. Radmilovic, U. Dahmen, M. Asta, and G. Gosh, Microscopy & Microanalysis 2012 Meeting, Phoenix, Arizona, 07/29 - 08/02
5. C. H. Liebscher, V. Radmilovic, U. Dahmen, M. Asta, and G. Gosh, Materials Science and Technology 2012 Meeting, Pittsburgh, Pennsylvania, 08/07 - 08/11
6. H. Ding, S. Huang, G. Ghosh, P. K. Liaw, and M. Asta, Materials Science and Technology 2012 Meeting, Pittsburgh, Pennsylvania, 08/07 - 08/11
7. Z. Sun, G. Song, Z. Teng, G. Ghosh, and P. K. Liaw , 2012 MRS Fall Meeting & Exhibit, Boston, 11/25 – 11/30
8. P. K. Liaw, M. Asta, D, Dunand, M. Fine, G. Ghosh, C. Liu, H. Ding, S. Huang, M. Rawlings, Z. Sun, G. Song, Z. Teng, G. Wang, and C. Liebscher, 2013 TMS Meeting, San Antonio, Texas, 03/03 – 03/07
9. Z. Sun, S. Huang, Z. Teng, G. Song, G. Wang, and P. K. Liaw, 2013 TMS Meeting, San Antonio, Texas, 03/03 – 03/09

10. G. Song, Z. Sun, G. Wang, H. Ding, C. Liebscher, M. D. Asta, G. Ghosh, D. C. Dunand, M. Rawling, N. Q Vo, and P. K. Liaw, 2015 TMS Meeting, Orlando, Florida, 3/15 – 3/19
11. Z. Sun, G. Song, J. Ilavsky, and P. K. Liaw, 2015 Materials Science & Technology Conference (MS&T), Columbus, Ohio, 10/4 – 10/8
12. G. Song, Z. Sun, L. Li, X. Xu, M. Rawlings, C. Liebscher, B. Clausen, J. Poplawsky, D. Leonard, S. Huang, Z. Teng, C. Liu, M. Asta, Y. Gao, D. Dunand, G. Ghosh, M. Chen, M. Fine, and P. K. Liaw, 2015 Materials Science & Technology Conference (MS&T), Columbus, Ohio, 10/4 – 10/8
13. G. Song, Z. Sun, D. Dunand, M. Rawlings, G. Ghosh, and P. K. Liaw, 2016 TMS Meeting, Nashville, Tennessee, 02/14 – 02/18
14. G. Song, Y. Gao, Z. Sun, J. Poplawsky, and P. K. Liaw , 2016 TMS Meeting, Nashville, Tennessee, 02/14 – 02/18
15. Z. Sun, G. Song, J. Ilavsky, G. Ghosh, and P. K. Liaw, 2016 TMS Meeting, Nashville, Tennessee, 02/14 – 02/18
16. Shao-Yu Wang, David Dunand, Gautam Ghosh, Gian Song, Sungil Baik, P. K. Liaw, 2017 MRS Meeting, Boston, Massachusetts, 11/26 – 12/01

Awards

1. Zhiqian Sun, TMS Best poster in Structural Materials Devision, 2014 TMS Annual Meeting & Exhibition, Feb.16-20, 2014, San Diego, California.
2. Zhiqian Sun, TMS Best Paper Contest – Graduate Division – First Place, TMS 2016 Annual Meeting & Exhibition, Feb. 14-18, 2016, Nashville, Tennessee
3. Gian Song, TMS Best Paper Contest – Graduate Division – Second Place, TMS 2016 Annual Meeting & Exhibition, Feb. 14-18, 2016, Nashville, Tennessee
4. Gian Song, TMS Best Paper Contest – Graduate Division – First Place, TMS 2017 Annual Meeting & Exhibition, Feb. 26-Mar. 2, 2017, San Diego, California

5. Peter K. Liaw, selected to be the TMS FELLOW, Class of 2018.